



Dissertation - Doctoral Thesis

Axisymmetric Combined Thermocapillary-Buoyant Flow in Sessile and Hanging Droplets

ausgeführt zum Zwecke der Erlangung des akademischen Grades
des Doktors der technischen Wissenschaften unter der Leitung

von

Univ. Prof. Dr. Hendrik C. Kuhlmann

Institutsnummer E322

Institut für Strömungsmechanik und Wärmeübertragung

von

M.Sc. Saeed Masoudi

Matrikelnummer 1228779

1120 Wien, Teichackergerasse 5/1

Wien, September 2016

Abstract

The combined thermocapillary-buoyant flow in sessile and hanging droplets is investigated numerically. The droplet sits on or hangs from a flat plate whose temperature is kept constant. The flow is driven by buoyancy and thermocapillary forces which arise due to a linear variation of the ambient temperature normal to the wall. Neglecting evaporation and in the limit of large mean surface tension the liquid–gas interface is spherical and non-deformable which allows to formulate the problem in body-fitted orthogonal toroidal coordinates such that the interface is a coordinate line.

Steady-state axisymmetric solutions to the incompressible Boussinesq equations are obtained using a vorticity–stream function formulation discretized by second-order central finite differences on a non-uniform grid. The resulting nonlinear difference equations are solved iteratively employing a Newton–Raphson method. The results in terms of stream function and temperature are presented varying influential parameters such as the contact angle, Reynolds number, heat transfer rate between the liquid and the ambient, fluid material, and level of gravity. Three different cases are comprehensively examined: thermocapillary-driven flow, buoyancy-driven flow, and mixed thermocapillary-buoyant flow.

A temporal two-dimensional linear stability analysis is carried out for the pure buoyant flow as well as for the thermocapillary-driven flow in droplets attached to a flat substrate. The onset of thermal instabilities is found in the buoyancy-driven flow when the temperature is uniformly distributed in vertical direction. Moreover, the existence of axisymmetric instabilities is examined for thermocapillary flow in liquid droplets varying different parameters.

Acknowledgements

First and foremost, I would like to sincerely thank my adviser, Prof. Hendrik C. Kuhlmann, for his continuous encouragement, understanding, and guidance during my doctoral studies at TU Wien. He gave me not only scientific, but also moral support in all the time of research and writing of this thesis. I would also like to thank all of the institute members for making the working environment a friendly and stress-free place.

Besides, I am especially grateful to the second referee Prof. Günter Brenn (TU Graz) who immediately accepted to examine the present doctoral thesis. I appreciate his insightful comments on a very short notice. Moreover, I am thankful to the rest of my thesis committee, Prof. Reinhard Willinger (TU Wien) who accepted to chair the defence session, and Prof. Tatiana Gambaryan-Roisman (TU Darmstadt) for reviewing my thesis.

A special thanks goes to my colleague and friend, Francesco Romanò, who is always willing to help the others. I deeply acknowledge his helpful suggestions regarding the numerical methods.

Finally, and most importantly, my deepest gratitude goes to my wife Sonia, who has been with me and encouraged me through all stages of research, writing, and editing of this thesis. Her understanding, support, and unwavering love were undeniably vital to the accomplishment of this dissertation.

Contents

1	Introduction	1
1.1	Motivation	1
1.2	Literature review	2
1.2.1	Rayleigh-Bénard convection	3
1.2.2	Evaporation	4
1.2.3	Marangoni effect	5
1.3	Scope of the thesis	7
2	Problem Formulation	9
2.1	Governing equations	10
2.1.1	Thermocapillary scaling	11
2.1.2	Boundary conditions	12
2.1.3	Viscous scaling	13
2.1.4	Boundary conditions	14
2.2	Linear stability analysis	14
3	Numerical Implementation	17
3.1	Toroidal coordinates	18
3.2	Steady axisymmetric flow	20
3.2.1	Vorticity-stream function formulation	20
3.2.2	Thermocapillary scaling	22
3.2.3	Viscous scaling	25
3.3	Numerical solution of the steady flow	26
3.3.1	Grid generation	26
3.3.2	Finite difference discretization	30
3.3.3	Newton's method	31
3.4	Steady solver code verification	32
3.5	Linear stability equations	35

4	Basic State Results	39
4.1	Heated substrate	39
4.1.1	Thermocapillary-driven flow	40
4.1.2	Buoyancy-driven flow	50
4.1.3	Thermocapillary-buoyant flow	56
4.2	Cooled substrate	61
4.2.1	Thermocapillary-driven flow	61
4.2.2	Buoyancy-driven flow	68
4.2.3	Thermocapillary-buoyant flow	74
5	Axisymmetric Linear Stability Analysis	85
5.1	Pure buoyant flow	85
5.2	Thermocapillary flow	91
5.3	Combined thermocapillary-buoyant flow	96
6	Summary and Conclusions	103
	Bibliography	107

Chapter 1

Introduction

In a liquid droplet attached to a flat substrate, which has a different temperature than the surrounding atmosphere, two main forces drive the fluid flow within the droplet. The temperature gradient along the free surface results in surface tension variation and consequently, the thermocapillary stresses drive the flow (Scriven and Sternling, 1960). In addition, buoyant forces act in the bulk as a result of a heterogeneous thermal expansion of the fluid (Lord Rayleigh, 1916).

1.1 Motivation

In-depth studies have been carried out on the thermocapillary-buoyant flow in liquid droplets owing to the important influence it has on many industrial processes. For instance, in surface coating and patterning processes by means of binary solutions, in order to achieve a uniform distribution of the particles over the surface, it is crucial not only to take into account the particle-surface interactions (Shmuylovich et al., 2002), but also the influence of Marangoni flow during the evaporation of the binary solution. Kim et al. (2016) show that, during the evaporation of the solution, a continuous mixing procedure due to a sequence of Marangoni flows leads to obtaining a homogeneous deposit. The solute- and surfactant-driven Marangoni effects are thoroughly discussed by Jamgotchian et al. (2001) and Marin et al. (2016). In microfluidic devices with open channels where the liquid has a free surface, one recent actuation technique is to employ the thermocapillary pumping to drive droplets or liquid streams (Sammarco and Burns, 2000; Chen et al., 2005). Experimental and analytical results are discussed by Odukoya and Naterer (2013) for the microheaters which drive the thermocapillary motion in microfluidic devices, considering different substrate materials. Dynamical

particle accumulation structures (PAS) are observed in droplets due to the thermocapillary convection (Ueno, 2011). Similar structures have been detected and extensively studied in liquid bridges (Schwabe et al., 1996; Ueno et al., 2008; Kuhlmann et al., 2014) as well as in annular pools (Lappa, 2013). The current study can be extended to find the PAS in liquid droplets. Another example of a technical application of the Marangoni effect is to produce smart surfaces which their surface properties can be triggered to switch between superhydrophobicity and superhydrophilicity (Guo et al., 2005). These surfaces are becoming widely demanding in space, aviation, and even automotive industries. For instance, these coatings can prevent fog condensation over surfaces with different chemical properties (Onda et al., 1996), or can be useful to produce self-cleaning surfaces in small-scale electronic circuits (Fürstner et al., 2005). Migrating droplets through Marangoni convection is another function conducted by Chen and Stebe (1997), Nguyen and Chen (2010) and Schmitt and Stark (2016). They investigated the influence of both the thermocapillarity and the surfactant-induced Marangoni stresses on the migration of a self-propelled droplet. Darhuber and Troian (2005) discussed the more general case of migration of the droplets by surface stresses. The last applications to be mentioned here are the control of deposition patterns by ejecting droplets through ink-jet printers (Park and Moon, 2006), and migrating bubbles and drops under reduced gravity (Subramanian and Balasubramanian, 2005; Wu and Hu, 2011). There are numerous other applications applied to Marangoni effect.

Considering all the discussed applications above, it is important to explicitly study the effects of thermocapillarity in liquid droplets by decoupling the problem into more manageable subproblems. Then it is possible to include more additional effects such as buoyancy, evaporation, and surface deformation. In this work, the thermocapillary-driven as well as the buoyancy-driven flows in liquid droplets are studied. Then the combined thermocapillary-buoyant flow is taken into account to analyze the interactions between buoyancy and thermocapillarity in sessile and hanging droplets.

1.2 Literature review

The fluid flow in a droplet attached to a flat rigid substrate has been studied from many aspects in the last two centuries. Many experimental as well as numerical studies were undertaken with the focus on natural convection, evaporation, and thermocapillary convection in sessile or hanging droplets. In this section, a brief review of previous studies in this field is given.

1.2.1 Rayleigh-Bénard convection

The most famous studies on the convection in a liquid layer subject to a vertical temperature stratification are done by Bénard (1900) and Lord Rayleigh (1916). The convection cells with periodic pattern which develop due to buoyancy-driven instabilities are known as Rayleigh-Bénard convection cells. The study of this type of convection leads to the development of hydrodynamic stability theory (Chandrasekhar, 1961; Drazin and Reid, 1981). In the past century, a huge amount of studies has been conducted to discuss this phenomenon in different geometries and under various conditions (Block, 1956; Busse, 1978; Bergé et al., 1980; Benguria and Depassier, 1987; Colinet and Legros, 1994). A stability analysis of a horizontal layer of liquid heated from below has been carried out by Clever and Busse (1974) in order to find the onset of convection varying the Prandtl and Rayleigh numbers. They found that the instabilities appear when the temperature difference across the liquid layer exceeds a critical value ($\Delta T > \Delta T_c$) which leads to the formation of periodic convection rolls with a certain wave number k . They showed that in the $\Delta T - k$ plane exists a region in which the steady convection rolls are stable. This region is known as the "Busse balloon". The transition from the steady to the time-dependent convection in two- and three-dimensions has been investigated by Curry et al. (1984) in rectangular and Morris et al. (1993) in cylindrical geometries. In the former work, the transition to the chaotic Rayleigh-Bénard convection in a liquid layer bounded by free-slip walls was studied numerically. They found that increasing the Rayleigh number through the chaotic regime leads to an increasing degree of small-scale structures. In the latter study, it was stated that a reason for the chaotic convection even for small Rayleigh numbers might be the large aspect ratio of the cylindrical cell even though the theory predicts that the steady rolls have to be stable. The onset of instability has been analytically found to be $Ra_c = 657.51$ for two impermeable parallel horizontal boundaries which are maintained at different constant temperatures by Lord Rayleigh (1916). Furthermore, the critical Rayleigh number for a plane layer of the fluid with free boundary at the top and rigid boundary at the bottom was obtained to be $Ra_c = 1100.65$ (Chandrasekhar, 1961).

In liquid droplets attached to a solid flat plate, buoyant forces are usually weaker than thermocapillary stresses; therefore, the convection inside the droplet is generated by surface-tension gradients rather than buoyancy (Zhang and Yang, 1982; Hegseth et al., 1996). As a consequence, the influence of buoyancy-driven flow in liquid droplets has not been extensively examined although in some cases buoyancy becomes dominant (Savino et al., 2002). In this work, the effect of buoyancy on the fluid flow in liquid droplets is investigated in the absence and presence of thermocapillarity by varying

key parameters such as Biot, Prandtl, and Rayleigh numbers.

1.2.2 Evaporation

In the early twentieth century, Irving Langmuir developed an equation to describe the liquid evaporation (Langmuir, 1932) using only the temperature and pressure parameters. Later in 1940s Birks and Bradley (1949) and Bradley and Shellard (1949) studied, more specifically, the evaporation of liquid droplets by taking into account the vapor pressure as well as temperature gradient in the droplet and in the ambient. Fuchs (1959) introduced d^2 law of evaporation for spherical droplets, stating that during the evaporation, the square of the droplet diameter decreases linearly with time. The evaporation of droplets on surfaces was theoretically studied by Picknett and Bexon (1977). They introduced three modes of evaporation: constant contact angle, constant radius, and the mixed mode for a large range of droplet shapes. They also realized that, except for very shallow droplets, the evaporation process begins with the constant radius up to a certain contact angle and then switches to the constant angle mode. They validated their predictions by comparing the results with experimental measurements as well as other theoretical works. The effect of the droplet size on the contact angle employing solid surfaces with different materials was examined by Good and Koo (1979). They experimentally observed that the contact angle variation depends not only on the material of the substrate, but also the droplet size.

Yekta-Fard and Ponter (1988) evaluated the impact of liquid vapor in the ambient on the contact angle for a wide range of liquid materials, droplet sizes, and substrate roughnesses. They also observed that for water droplets residing on different substrates in a vapor saturated environment, the contact angle increases by decreasing the drop size. Hegseth et al. (1996) investigated a significant interior flow in evaporating droplets and provided a formula for the droplet lifetime. They detected unsteady cellular structures which always appeared close to the droplet surface, meaning that the surface tension gradients drive the flow. A numerical model for describing the hydrodynamics inside an evaporating droplet was developed by Mollaret et al. (2004). They also studied the effect of the humidity on the evaporation process, on the presumption that the droplet has a spherical cap shape. The model was confirmed by comparing the results with that of their own experiments and also with the previous experimental results.

McHale et al. (2005) studied the evaporation of water droplets on superhydrophobic surfaces experimentally. They found that superhydrophobic textured surfaces consisting of circular micro-pillars lead to form droplets with contact angles even larger than

160°. The evaporation mode for droplets of such large contact angles was found to be constant radius initially up to a certain contact angle followed by a stepwise contact line jump from one pillar to the other. Dunn et al. (2008) provided a mathematical model for the evaporation of a shallow axisymmetric sessile droplet assuming the constant radius evaporation mode. They showed that the total evaporation rate depends on the thermal conductivity of both the liquid droplet and the flat substrate as well as the ambient pressure. A numerical method for simulating the evaporation of a non-spherical axisymmetric sessile droplet was developed by Barash et al. (2009). For the simulations, they took into account the shape deformation of the droplet induced by gravity. Moreover, they considered the influence of the thermal conduction in the droplet as well as nonstationary effects of the vapor diffusion in the ambient air. Yet, they noticed that approximating the shape of droplet by a spherical-cap agrees well with the flow characteristics obtained from the simulation of the real droplet shape.

Evaporation of droplets attached to a flat substrate results in the evolution of different flow patterns (Sefiane et al., 2008; Carle et al., 2012). Finding the origin of these flow patterns made the stability analysis of the liquid droplets interesting. Karapetsas et al. (2012) showed that the thermocapillary instabilities (Davis, 1987; Schwabe et al., 1992) are responsible for the appearance of the hydrothermal waves, leading to the development of the patterns. Resulting from their numerical simulations, they discovered the formation of stationary multiple rolls as well as traveling hydrothermal waves within the droplet.

Although evaporation has a significant influence on the flow behavior within droplets, it has been neglected in the current study due to the following reasons. Assuming a non-volatile droplet leads to mass conservation and consequently the liquid-gas interface can be assumed to have a non-deformable shape (in the limit of large mean surface tension) which significantly simplifies the problem. Furthermore, neglecting evaporation, the influence of the other phenomena such as thermocapillarity and buoyancy can be independently studied.

1.2.3 Marangoni effect

The gradient of temperature along the free surface of a liquid results in surface tension stresses which drive the Marangoni convection (Marangoni, 1871; Scriven and Sternling, 1960). The Marangoni effect has been observed and studied in many fluid mechanics problems (Pesach and Marmur, 1987; Fuhrich et al., 2001; Arafune et al., 2003). However, in case of droplets and bubbles, Bond and Newton (1928) were probably the first

who investigated the effect of thermocapillarity. They showed, both theoretically and experimentally, that because of the Marangoni effects the terminal velocity of spherical droplets or bubbles surrounded by a medium of higher viscosity is larger than that of a solid sphere with the same size and mass. Much later, Citakoglu and Rose (1969) investigated the influence of surface curvature as well as the non-equilibrium at the liquid-vapor interface in small droplets on the rate of heat transfer during evaporation and condensation processes. They experimentally observed that the thermocapillary convection has a strong influence on the heat transfer in a droplet. Davis and Homay (1980) observed the formation and detachment of droplets from a fluid layer with a free surface due to thermocapillary stresses along the free surface. Shih and Megaridis (1996) studied numerically the effect of thermocapillary forces on the lifetime of evaporating droplets, and concluded that the thermocapillary flow along the free surface amplifies the internal circulation in the droplet and subsequently decreases the evaporation time.

Savino et al. (2002) studied buoyancy and thermocapillary effects on the evaporation of hanging drops and evaluated the flow in octane and water. In the case of octane droplets they observed that the effect of thermocapillary stresses is essential and buoyancy does not affect the fluid flow. On the other hand, they examined a water droplet in which the thermocapillary effect can be disregarded, and compared the flow characteristics with the former case. However, they considered a fixed and non-deformable liquid-air interface by considering a quasi-steady process. Carle et al. (2012) detected hydrothermal waves in drops of ethanol under microgravity conditions during a parabolic flight as well as under normal gravity condition. They observed that the resulting hydrothermal waves have similar characteristics (apart from the g-jitter effect). Consequently, they confirmed that the thermocapillary instabilities result in the observed hydrothermal waves.

The evaporation of non-axisymmetric droplets was examined by Sáenz et al. (2015). Their experimental and numerical study showed the existence of three-dimensional azimuthal flow in the bulk of the droplet. They also detected two counter-rotating vortices emerging in the transient stage right after placing the droplet over a heated substrate. The strength of these vortices is found to be directly related to the initial temperature difference between the droplet and the substrate. Furthermore, they discussed the influence of thermocapillary convection and thermal conduction on the temperature distribution within the droplet. More recently, Al-Sharafi et al. (2016) investigated the effects of buoyant and thermocapillary forces on the fluid flow within a droplet sitting on a superhydrophobic surface. Droplets with contact angles of up to 150° have been considered. In the limit of large contact angles, they detected a pair of

counter-rotating circulation cells in the upper part of the droplet. They claimed that the combination of buoyancy and thermocapillarity results in the formation of these vortices. A state-of-the-art application of thermocapillarity is introduced by Black (2016) for the lab-on-a-chip applications. He introduced a number of methods to capture and levitate a nano-scale inner droplet within a larger compound drop by means of thermocapillary convection.

A mechanism known as coffee-ring effect was first presented by Deegan et al. (1997). They observed patterns over the substrate left from the edge of an evaporating droplet containing colloidal particles. Following their work, many other researchers tried to employ this phenomenon in many industrial applications. For instance, Nguyen and Stebe (2002) proposed that by altering the boundary conditions along the liquid-gas interface in a droplet, it is possible to control the structure of patterns formed from an evaporating droplet. The reversal of the coffee-ring phenomenon by thermocapillary-driven flow was introduced by Hu and Larson (2006), both experimentally and theoretically, showing that the particles deposit at the center of the droplet. Considering the thermal conductivity of the substrate, Ristenpart et al. (2007) arrived at the conclusion that the direction of the Marangoni flow in a sessile droplet is based on the relative thermal conductivities of the substrate and the liquid; a phenomenon which may notably change the resulting particle-deposition patterns. Through a mathematical model, Dunn et al. (2009) addressed the significant impact of substrate conductivity on droplet evaporation. Another recent application of the coffee-ring effect is related to molecular semiconductors which are used in electronic devices. Wang et al. (2016) demonstrated that, employing thermocapillary-driven flow, it is possible to grow bilayer semiconductors in a rapid cost-efficient way.

1.3 Scope of the thesis

As it is discussed in the previous section, many of the earlier studies have addressed the flow and the temperature fields, evaporation rate, chemical and mechanical properties of the substrate, and the interactions between different forces which are driving the flow in droplets, qualitatively. The numerical study of the fluid flow within a droplet is, however, challenging as the liquid-gas interface is nonstationary and has a curvature. In order to meet the challenge, a non-volatile droplet with a spherical-cap-shape interface is considered assuming that the mean surface tension is asymptotically large. The aim of this work is a detailed numerical study of the internal convective flow of a droplet considering thermocapillary, buoyant, and combined thermocapillary-buoyant forces.

Chapter 1 Introduction

In this study, thermocapillary and buoyant flows in sessile and hanging droplets are considered, taking into account a variety of Prandtl numbers, droplet sizes and shapes, gravity levels, temperature gradients, and heat transfer rates through the liquid-gas interface. Moreover, a two-dimensional axisymmetric linear stability analysis is presented to investigate the mechanism of thermal instability in pure buoyant flow as well as to examine the existence of axisymmetric instabilities in thermocapillary flows in liquid droplets. None of these topics have been systematically studied before.

All the physical, theoretical, and numerical aspects of this research together with the obtained results are presented in the following order. Chapter 2 provides the problem formulation including the governing equations in different scalings as well as the linear stability equations. The relevant boundary conditions for each set of equations are also derived. In chapter 3 the numerical implementations are presented in detail. The properties of the body-fitted coordinate system employed in this study is introduced, the numerical methods which are used to solve the problem are provided, and the computational code is verified prior to solving the main problem by means of a two-dimensional exact solution of the Navier-Stokes equations. The steady-state results are provided in chapter 4 for both sessile and hanging droplets attached to a heated or cooled flat substrate. Chapter 5 presents the axisymmetric two-dimensional linear stability analysis of the buoyancy-driven, the thermocapillary-driven, and the combined thermocapillary-buoyant-driven flows. Finally, the summary and conclusions are given in chapter 6.

Chapter 2

Problem Formulation

The fluid flow confined to a droplet in contact with a solid flat plate is considered. The fluid is an incompressible Newtonian liquid of density ρ , surface tension σ , kinematic viscosity ν and thermal diffusivity κ . The temperature of the flat plate T_0 is kept constant and the droplet is either sitting on or hanging from the flat plate. The temperature of the passive ambient varies linearly from T_0 at the level of the plate to $T_a(z) = T_0 + bz$ at a perpendicular distance z from the plate, where b can be positive or negative. In practice, this constant temperature gradient can be reproduced between two parallel isothermal flat plates with different temperatures. Far from the edges of the parallel plates, the conduction heat transfer dominates and consequently, the temperature isolines are parallel to the flat plates, varying linearly in the fully developed thermal region (Eckert and Carlson, 1961; Guo et al., 1998).

This temperature gradient drives the heat transfer between the liquid droplet and the ambient gas which leads to a surface tension variation $\sigma(T)$ along the free surface. In the linear approximation

$$\sigma = \sigma_0 - \gamma_s(T - T_0), \quad (2.1)$$

where σ_0 is the surface tension at the reference (flat plate) temperature and $\gamma_s = -\partial\sigma/\partial T|_{T_0}$ is the surface-tension coefficient.

A spherical-cap-shaped droplet of radius R is considered assuming that the static Bond number

$$\text{Bo} = \frac{\rho g L^2}{\sigma_0} \quad (2.2)$$

as well as the Capillary number

$$\text{Ca} = \frac{\gamma_s |\Delta T|}{\sigma_0} \quad (2.3)$$

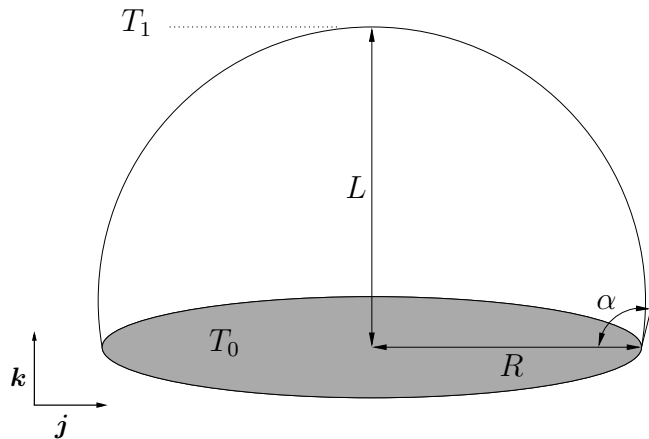


Figure 2.1: Droplet with base radius R in contact with a flat plate at temperature T_0 . The temperature in the passive gas at the level of the droplet's apex is T_1 . The contact angle α is indicated. \mathbf{j} and \mathbf{k} are unit vectors in Cartesian coordinates.

tend to zero in the limit of large mean surface tension, where L is the maximum height of the droplet. These assumptions ensure that the static and dynamic deformations of the liquid-gas interface are negligible (see Rienstra, 1990). Furthermore, we assume a non-volatile liquid which guarantees a time-independent droplet shape. Figure 2.1 shows the configuration for a sessile droplet with a contact angle $\alpha = 100^\circ$.

For the setup described only two forces drive the fluid flow: buoyancy and thermocapillarity. The effects of these driving forces are studied separately as well as jointly. The thermal stratification in vertical direction initiates a buoyant flow within the droplet's bulk for a strong enough gravity level. On the other hand, the surface-tension variation leads to the thermocapillary effect which generates the fluid motion along the droplet's free surface.

2.1 Governing equations

The sets of equations governing the thermocapillary-buoyant flow have been derived previously in detail for similar fluid dynamical problems by, e.g., Bergman and Ramadhyani (1986); Davis (1987); Ben Hadid and Roux (1992) and Priede and Gerbeth (1997). Therefore, the derivation of the governing equations consisting of continuity, Navier–Stokes, and energy equations is not repeated here. However, some important remarks which specifically address the current problem are presented in this chapter.

Two different scalings of the governing equations have been employed in this work, the thermocapillary scaling (Ostrach, 1977; Haj-Hariri et al., 1997), which is applied for the cases of the pure thermocapillary flow as well as for the combined thermocapillary-buoyant flow, and the viscous scaling (Busse, 1986) for the case of pure buoyancy-driven flow.

2.1.1 Thermocapillary scaling

The flow is governed by the Navier–Stokes, continuity, and energy equations in the Boussinesq approximation

$$\partial_t \mathbf{U}_0 + (\mathbf{U}_0 \cdot \nabla) \mathbf{U}_0 = -\frac{1}{\rho} \nabla P_0 + \nu \nabla^2 \mathbf{U}_0 + g T_0 \mathbf{k}, \quad (2.4a)$$

$$\nabla \cdot \mathbf{U}_0 = 0, \quad (2.4b)$$

$$\partial_t T_0 + \mathbf{U}_0 \cdot \nabla T_0 = \kappa \nabla^2 T_0, \quad (2.4c)$$

where \mathbf{k} is the unit vector normal to the flat plate in Cartesian coordinates. In (2.4) the subscript 0 denotes basic flows. The Boussinesq approximation assumes that the density variation is negligible in all terms of the governing equations except in the gravity term in (2.7a), which is responsible for the buoyancy-driven flow (Zeytounian, 2003).

The temperature is scaled by $\Delta T = |T_1 - T_0|$, where $T_1 = bL$ is the passive ambient temperature at a distance L above (or below) the plate. Moreover, we define the mean temperature $T_m = (T_0 + T_1)/2$ which is employed to non-dimensionalize the temperature. The reduced temperature

$$\theta_0 = \frac{(T - T_m)}{\Delta T} + \frac{1}{2} \quad (2.5)$$

is defined such that in the case of a hot plate in a cold atmosphere $\theta_0(z = 0) = 1$ and $\theta_0(z = l) = 0$ (where $l = L/R$) in the passive gas, and in the case of a cold plate and

Variable	r	t	U_0, V_0, W_0	Ψ_0	P_0	θ_0
Scale	R	R/U^*	$U^* = (\nu/R)\text{Re}$	νRe	ρU^{*2}	ΔT

Table 2.1: Thermocapillary scaling of the variables with Re according to (2.6).

hot ambient $\theta_0(z = l) = 1$ and $\theta_0(z = 0) = 0$.

Important dimensionless parameters in (2.7) are Reynolds, Prandtl, and Grashof numbers

$$\text{Re} = \frac{U^* R}{\nu} = \frac{\gamma_s \Delta T R}{\rho \nu^2}, \quad \text{Pr} = \frac{\nu}{\kappa}, \quad \text{Gr} = \frac{g \beta \Delta T R^3}{\nu^2}, \quad (2.6)$$

using the thermocapillary scaling which is given in table 2.1, where $\beta = -\rho^{-1} \partial \rho / \partial T|_p$ is the linear thermal expansion coefficient of the liquid. In this scaling U^* is the characteristic thermocapillary velocity, as stated in Nienhüser and Kuhlmann (2002). Now we can write the non-dimensional set of the governing equations as

$$\text{Re} (\partial_t + \mathbf{U}_0 \cdot \nabla) \mathbf{U}_0 = -\nabla P_0 + \nabla^2 \mathbf{U}_0 + \frac{\text{Gr}}{\text{Re}} \theta_0 \mathbf{k}, \quad (2.7a)$$

$$\nabla \cdot \mathbf{U}_0 = 0, \quad (2.7b)$$

$$\text{Ma} (\partial_t + \mathbf{U}_0 \cdot \nabla) \theta_0 = \nabla^2 \theta_0. \quad (2.7c)$$

The product RePr , which is here termed the Marangoni number, Ma , is otherwise the Peclet number ($\text{Pe} = U^* R / \kappa = \text{RePr}$).

2.1.2 Boundary conditions

To solve the governing equations specified above, a set of boundary conditions has to be defined on all boundaries of the domain.

The no-slip boundary condition for the velocity

$$\mathbf{U}_0 = 0, \quad (2.8)$$

as well as a Dirichlet boundary condition for the temperature

$$\theta_0 = \begin{cases} 1, & \text{if } b < 0 \text{ (hot plate),} \\ 0, & \text{if } b > 0 \text{ (cold plate),} \end{cases} \quad (2.9)$$

are imposed on the flat plate.

The non-volatile-liquid assumption imposes the global conservation of mass for a stationary droplet shape, which means that the velocity normal to the liquid-gas interface is zero, i.e.

$$\mathbf{n} \cdot \mathbf{U}_0 = 0, \quad (2.10)$$

where \mathbf{n} is the unit vector normal to the free surface. Moreover, the balance between tangential viscous stresses and thermocapillary forces along the free surface yields

$$\mathbf{t}_1 \cdot (\mathbf{S} \cdot \mathbf{n}) = -\mathbf{t}_1 \cdot \nabla \theta_0, \quad (2.11a)$$

$$\mathbf{t}_2 \cdot (\mathbf{S} \cdot \mathbf{n}) = -\mathbf{t}_2 \cdot \nabla \theta_0, \quad (2.11b)$$

where $\mathbf{S} = \nabla \mathbf{U}_0 + (\nabla \mathbf{U}_0)^T$ is the viscous stress tensor in the liquid phase and \mathbf{t}_1 and \mathbf{t}_2 are the two orthogonal unit vectors tangent to the free surface. It should be mentioned that the viscous stresses in the gas phase are neglected.

To model the heat transfer between the liquid and the ambient gas Newton's law is employed

$$\mathbf{n} \cdot \nabla \theta_0 = -\text{Bi}(\theta_0 - \theta_a), \quad \theta_a(z) = \begin{cases} 1 - z/l, & \text{if } b < 0 \text{ (hot plate),} \\ z/l, & \text{if } b > 0 \text{ (cold plate),} \end{cases} \quad (2.12)$$

where $\text{Bi} = hR/k$ the Biot number, in which h is the heat transfer coefficient and k denotes the thermal conductivity of the gas. $\text{Bi} = 0$ implies that the liquid-gas interface is adiabatic, whereas the $\text{Bi} \rightarrow \infty$ imposes the fixed temperature $\theta_a(z)$ along the free surface.

2.1.3 Viscous scaling

For pure buoyancy-driven flow, the viscous scaling is employed instead of the thermocapillary scaling discussed above. The scaling of the governing equations (2.7) is converted to viscous scaling by redefining the characteristic velocity as

$$U^* = \frac{\nu}{R}, \quad (2.13)$$

and setting $\text{Re} = 1$. The variables are then scaled as shown in table 2.2. The governing equations read

$$(\partial_t + \mathbf{U}_0 \cdot \nabla) \mathbf{U}_0 = -\nabla P_0 + \nabla^2 \mathbf{U}_0 + \text{Gr} \theta_0 \mathbf{k}, \quad (2.14a)$$

$$\nabla \cdot \mathbf{U}_0 = 0, \quad (2.14b)$$

$$\text{Pr} (\partial_t + \mathbf{U}_0 \cdot \nabla) \theta_0 = \nabla^2 \theta_0. \quad (2.14c)$$

Variable	r	t	U_0, V_0, W_0	Ψ_0	P_0	θ_0
Scale	R	R^2/ν	ν/R	ν	$\rho\nu^2/R^2$	ΔT

Table 2.2: Viscous scaling of the variables.

In this case, the thermocapillary stresses are neglected. However, we assume that the surface tension keeps the steady spherical-cap-shape of a non-volatile droplet subject to any level of gravity which is used in this study.

2.1.4 Boundary conditions

As discussed in the previous subsection, for the viscous scaling, the boundary condition on liquid-gas interface has to be modified. Neglecting the thermocapillary stresses, a free-slip condition is considered along the free surface which reads

$$\partial_n(\mathbf{U}_0 \cdot \mathbf{t}_1) = 0. \quad (2.15)$$

The temperature boundary condition along the free surface as well as the velocity and temperature boundary conditions at the substrate remain the same as in (2.12), (2.8), and (2.9), respectively.

2.2 Linear stability analysis

In this work, the two-dimensional axisymmetric stability is analyzed for the thermocapillary driven flow, the pure buoyant flow, as well as the combined buoyant-thermocapillary convection in liquid droplets.

In order to determine the linear stability of the flow, a total flow is introduced which consists of the basic flow and infinitesimal perturbations $|(\tilde{\mathbf{u}}, \tilde{p}, \tilde{\theta})| \ll 1$ (Drazin and Reid, 1981)

$$\mathbf{u}(\mathbf{x}, t) = \mathbf{U}_0 + \tilde{\mathbf{u}}, \quad p(\mathbf{x}, t) = P_0 + \tilde{p}, \quad \theta(\mathbf{x}, t) = \theta_0 + \tilde{\theta}, \quad (2.16)$$

where $\mathbf{x} = (x_1, x_2, x_3)$ is the vector of the three coordinates. Considering the same boundary conditions as in the basic state, the governing equations (thermocapillary

scaling) can be written for the total flow

$$\text{Re}(\partial_t + \mathbf{u} \cdot \nabla) \mathbf{u} = -\nabla p + \nabla^2 \mathbf{u} + \frac{\text{Gr}}{\text{Re}} \theta \mathbf{k}, \quad (2.17a)$$

$$\nabla \cdot \mathbf{u} = 0, \quad (2.17b)$$

$$\text{Ma}(\partial_t + \mathbf{u} \cdot \nabla) \theta = \nabla^2 \theta. \quad (2.17c)$$

Substituting (2.16) into (2.17) and subtracting the basic flow yields

$$\text{Re}(\partial_t \tilde{\mathbf{u}} + \tilde{\mathbf{u}} \cdot \nabla \mathbf{U}_0 + \mathbf{U}_0 \cdot \nabla \tilde{\mathbf{u}} + \tilde{\mathbf{u}} \cdot \nabla \tilde{\mathbf{u}}) = -\nabla \tilde{p} + \nabla^2 \tilde{\mathbf{u}} + \frac{\text{Gr}}{\text{Re}} \tilde{\theta} \mathbf{k}, \quad (2.18a)$$

$$\nabla \cdot \tilde{\mathbf{u}} = 0, \quad (2.18b)$$

$$\text{Ma}(\partial_t \tilde{\theta} + \tilde{\mathbf{u}} \cdot \nabla \theta_0 + \mathbf{U}_0 \cdot \nabla \tilde{\theta} + \tilde{\mathbf{u}} \cdot \nabla \tilde{\theta}) = \nabla^2 \tilde{\theta}. \quad (2.18c)$$

Furthermore, the quadratic terms $\tilde{\mathbf{u}} \cdot \nabla \tilde{\mathbf{u}}$ and $\tilde{\mathbf{u}} \cdot \nabla \tilde{\theta}$ can be neglected due to the assumption of infinitesimal perturbations. Therefore, the governing equations for infinitesimal perturbations read

$$\text{Re}(\partial_t \tilde{\mathbf{u}} + \tilde{\mathbf{u}} \cdot \nabla \mathbf{U}_0 + \mathbf{U}_0 \cdot \nabla \tilde{\mathbf{u}}) = -\nabla \tilde{p} + \nabla^2 \tilde{\mathbf{u}} + \frac{\text{Gr}}{\text{Re}} \tilde{\theta} \mathbf{k}, \quad (2.19a)$$

$$\nabla \cdot \tilde{\mathbf{u}} = 0, \quad (2.19b)$$

$$\text{Ma}(\partial_t \tilde{\theta} + \tilde{\mathbf{u}} \cdot \nabla \theta_0 + \mathbf{U}_0 \cdot \nabla \tilde{\theta}) = \nabla^2 \tilde{\theta}. \quad (2.19c)$$

Considering the assumptions which are discussed for the basic flow, the boundary conditions corresponding to (2.19) are

$$\tilde{\theta} = 0, \quad \tilde{\mathbf{u}} = 0, \quad (\text{on the flat plate}), \quad (2.20)$$

and

$$\left. \begin{aligned} \mathbf{n} \cdot \tilde{\mathbf{u}} &= 0 \\ \mathbf{n} \cdot \nabla \tilde{\theta} &= -\text{Bi} \tilde{\theta} \\ \mathbf{t}_1 \cdot (\mathbf{S} \cdot \mathbf{n}) &= -\mathbf{t}_1 \cdot \nabla \tilde{\theta} \\ \mathbf{t}_2 \cdot (\mathbf{S} \cdot \mathbf{n}) &= -\mathbf{t}_2 \cdot \nabla \tilde{\theta} \end{aligned} \right\} (\text{on the free surface}). \quad (2.21)$$

Similarly, for the case of viscous scaling, the governing equations for the infinitesimal

perturbations are

$$(\partial_t \tilde{\mathbf{u}} + \tilde{\mathbf{u}} \cdot \nabla \mathbf{U}_0 + \mathbf{U}_0 \cdot \nabla \tilde{\mathbf{u}}) = -\nabla \tilde{p} + \nabla^2 \tilde{\mathbf{u}} + \text{Gr} \tilde{\theta} \mathbf{k}, \quad (2.22a)$$

$$\nabla \cdot \tilde{\mathbf{u}} = 0, \quad (2.22b)$$

$$\text{Pr} \left(\partial_t \tilde{\theta} + \tilde{\mathbf{u}} \cdot \nabla \theta_0 + \mathbf{U}_0 \cdot \nabla \tilde{\theta} \right) = \nabla^2 \tilde{\theta}, \quad (2.22c)$$

with the same boundary conditions as in (2.20) and (2.21), except for the perturbation velocity tangent to the liquid-gas interface

$$\partial_n(\tilde{\mathbf{u}} \cdot \mathbf{t}_1) = 0. \quad (2.23)$$

The general solution of (2.19) as well as (2.22) can be introduced as a superposition of normal modes, considering the periodic extension of the domain in azimuthal (x_3) direction

$$\begin{pmatrix} \tilde{\mathbf{u}} \\ \tilde{p} \\ \tilde{\theta} \end{pmatrix} (x_1, x_2, x_3, t) = \begin{pmatrix} \hat{\mathbf{u}} \\ \hat{p} \\ \hat{\theta} \end{pmatrix} (x_1, x_2) e^{-\gamma t + i m x_3} + c.c. \quad (2.24)$$

where $\hat{\mathbf{u}}$, \hat{p} and $\hat{\theta}$ are the shape functions of the perturbations, $m \in \mathbb{N}$ is a natural wave number in azimuthal direction, and γ is the temporal complex decay rate

$$\gamma = \mu + i\omega \in \mathbb{C} \quad (2.25)$$

of (2.24), includes the decay rate $\mu \in \mathbb{R}$ and the oscillation frequency $\omega \in \mathbb{R}$. In order to have normalized shape functions of the perturbations we set the maximum infinity norm to 1 within the computational domain.

The substitution of the normal mode ansatz (2.24) into the perturbation equations (2.19) requires first to choose an appropriate coordinate system such that the governing equations can be discretized, which will be discussed in the next chapter.

Chapter 3

Numerical Implementation

In order to treat the governing equations numerically, it is preferred to select a body-fitted coordinate system such that no coordinate mapping will be needed. At the first glance, considering liquid droplets with a spherical-cap shape, the spherical coordinate system is a practical option. However, considering droplets of different contact angles, the coordinate lines fit perfectly only to the free surface of droplets and no coordinate line fits to the solid wall (except in case of $\alpha = \pi/2$). Therefore, the spherical coordinate system is not an optimal coordinate system for the current study.

Among the available curvilinear coordinate systems, toroidal coordinates seem to be a suitable candidate for this problem. As it is shown in figure 3.1, the $\xi = \text{constant}$ lines fit to the free surface of spherical-cap-shaped droplets with different contact angles. Moreover, the $\xi = \xi_{\text{max}} = \pi$ line fits to the flat substrate. However, a singularity which appears in toroidal coordinates when $\eta \rightarrow \infty$ has to be treated numerically. On the other hand, the differential vector operators are quite complicated and the numerical discretization is hard to implement. Nevertheless, this coordinate system has been used in some specific problems such as solving the force-free magnetic-field boundary-value problem (Buck, 1965) or simulation of the flow in the throat of convergent-divergent nozzles (Kliegel and Levine, 1969). Although some researchers have employed toroidal coordinates, no comprehensive reference is available for this coordinate system. Therefore, we first need to discuss the coordinate system itself and then derive the differential operators.

3.1 Toroidal coordinates

Toroidal coordinates are obtained by rotating planar bipolar coordinates about the y -axis (Arfken, 1985). Two foci of the coordinate system which are located at $(\pm a, 0)$ coincide with the three-phase contact line of the droplet, where $a = 1$ introduces the dimensionless form of the drop's base radius regardless of the contact angle. The transformation equations from toroidal to Cartesian coordinates as well as the scale factors are

$$x = \frac{a \sinh \eta \cos \phi}{\cosh \eta - \cos \xi}, \quad y = \frac{a \sinh \eta \sin \phi}{\cosh \eta - \cos \xi}, \quad z = \frac{a \sin \xi}{\cosh \eta - \cos \xi}, \quad (3.1a)$$

$$h_\eta = \frac{a}{\cosh \eta - \cos \xi}, \quad h_\xi = \frac{a}{\cosh \eta - \cos \xi}, \quad h_\phi = \frac{a \sinh \eta}{\cosh \eta - \cos \xi}, \quad (3.1b)$$

and the unit vectors $(\mathbf{e}_\eta, \mathbf{e}_\xi, \mathbf{e}_\phi)$ read

$$\mathbf{e}_\eta = \frac{\cos \phi (1 - \cosh \eta \cos \xi)}{q} \mathbf{i} + \frac{\sin \phi (1 - \cosh \eta \cos \xi)}{q} \mathbf{j} - \frac{\sinh \eta \sin \xi}{q} \mathbf{k}, \quad (3.2a)$$

$$\mathbf{e}_\xi = -\frac{\sinh \eta \sin \xi \cos \phi}{q} \mathbf{i} - \frac{\sinh \eta \sin \xi \sin \phi}{q} \mathbf{j} + \frac{\cosh \eta \cos \xi - 1}{q} \mathbf{k}, \quad (3.2b)$$

$$\mathbf{e}_\phi = -\sin \phi \mathbf{i} + \cos \phi \mathbf{j}, \quad (3.2c)$$

where

$$q = \cosh \eta - \cos \xi. \quad (3.3)$$

The coordinates satisfy $\eta \in [0, \infty)$, $\xi \in [0, 2\pi]$, and $\phi \in [0, 2\pi]$. The inverse transformation from Cartesian to toroidal coordinates reads

$$\eta = \ln \frac{d_1}{d_2}, \quad \xi = \cos^{-1} \left(\frac{d_1^2 + d_2^2 - 4a^2}{2d_1 d_2} \right), \quad \phi = \tan^{-1} \frac{y}{x}, \quad (3.4)$$

where $d_{1,2} = \sqrt{x^2 + y^2 + z^2 + a^2 \pm 2a\sqrt{x^2 + y^2}}$.

In three dimensions a ξ -constant surface

$$2az \cot \xi = x^2 + y^2 + z^2 - a^2, \quad 0 \leq \xi \leq 2\pi, \quad (3.5)$$

with the center-point positioned at $(0, 0, a \cot \xi)$ and radius $a |\cot \xi|$ fits to the free surface of a spherical-cap-shaped sessile or hanging droplet of contact angle α . The

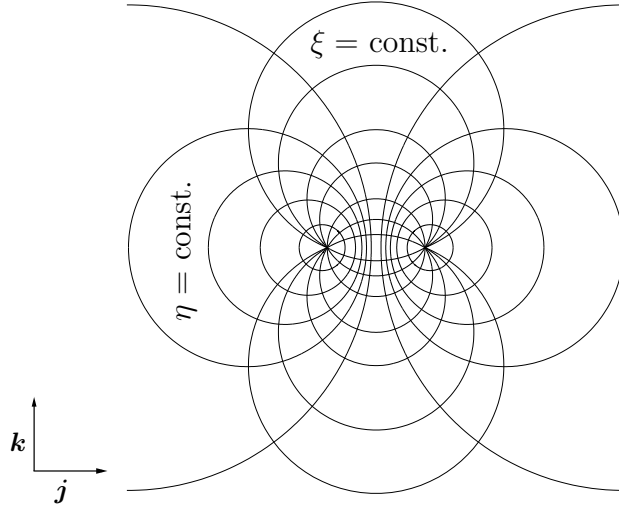


Figure 3.1: Toroidal coordinates. \mathbf{j} and \mathbf{k} are unit vectors in Cartesian coordinates.

contact angle can be expressed as a function of ξ which fits to the liquid-gas interface. It reads

$$\alpha(\xi_{\min}) = \pi - \xi_{\min}, \quad (3.6)$$

where $0 < \xi_{\min} < \pi$ fits to the free surface of all possible drop shapes, from a droplet of a very large contact angle over a superhydrophobic surface to an extremely shallow one. On the other hand, $\xi_{\max} = \pi$ fits to the flat plate. However, to provide a better imagination of the problem setup, a two-dimensional sample grid in toroidal coordinates is illustrated in figure 3.2 for $\alpha = \pi/2$ and $\phi = 0$.

The differential vector operators gradient, divergence, curl, and Laplacian, respectively, are written as

$$\nabla\psi = \frac{q}{a} \left(\mathbf{e}_\eta \frac{\partial\psi}{\partial\eta} + \mathbf{e}_\xi \frac{\partial\psi}{\partial\xi} + \mathbf{e}_\phi \frac{1}{\sinh\eta} \frac{\partial\psi}{\partial\phi} \right), \quad (3.7a)$$

$$\nabla \cdot \mathbf{U} = \frac{q}{a} \left[\frac{\partial U_\eta}{\partial\eta} + \frac{\partial U_\xi}{\partial\xi} + \frac{1}{\sinh\eta} \frac{\partial U_\phi}{\partial\phi} - 2U_\xi H_3 + U_\eta H_1 \right], \quad (3.7b)$$

$$\nabla \times \mathbf{U} = \frac{q^3}{a^3 \sinh\eta} \begin{vmatrix} \mathbf{e}_\eta(a/q) & \mathbf{e}_\xi(a/q) & \mathbf{e}_\phi(a/q) \sinh\eta \\ \partial_\eta & \partial_\xi & \partial_\phi \\ (a/q)U_\eta & (a/q)U_\xi & (a/q) \sinh\eta U_\phi \end{vmatrix}, \quad (3.7c)$$

$$\nabla^2\psi = \frac{q^2}{a^2} \left[\partial_{\eta\eta}\psi + \partial_{\xi\xi}\psi + \frac{1}{\sinh^2\eta} \partial_{\phi\phi}\psi - H_2 \partial_\eta\psi - H_3 \partial_\xi\psi \right], \quad (3.7d)$$

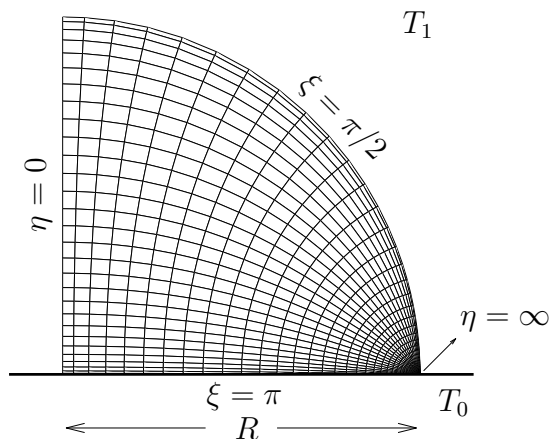


Figure 3.2: A sample non-uniform grid corresponding to toroidal coordinates (η, ξ) .

where

$$H_1 = \left(\frac{\cosh \eta}{\sinh \eta} - \frac{2 \sinh \eta}{q} \right), \quad H_2 = \left(\frac{\cosh \eta \cos \xi - 1}{q \sinh \eta} \right), \quad H_3 = \frac{\sin \xi}{q}, \quad (3.8)$$

and $\mathbf{U} = (U_\eta, U_\xi, U_\phi)^T$ is the (velocity) vector in toroidal coordinates. These differential operators are employed to formulate the Navier–Stokes, continuity, and energy equations in toroidal coordinates.

3.2 Steady axisymmetric flow

In the limit of relatively small Reynolds numbers the flow in a drop can be assumed to be steady and axisymmetric with respect to the centerline $\eta = 0$ using toroidal coordinates (η, ξ, ϕ) . Therefore, we can eliminate the following terms from the governing equations

$$\partial_t = \partial_\phi = U_\phi = 0. \quad (3.9)$$

3.2.1 Vorticity-stream function formulation

Rewriting the governing equations in vorticity-stream function formulation simplifies the solution procedure, since the pressure will drop out from the equations. In order

to define the Stokes stream function and vorticity in toroidal coordinates, we have to start from the vector potential

$$\mathbf{U}_0 = \nabla \times \mathbf{B}, \quad (3.10)$$

in which the stream function Ψ_0 builds the only non-zero component of the vector potential (Batchelor, 1967)

$$\mathbf{B} = \left(0, 0, \frac{q}{a \sinh \eta} \Psi_0(\eta, \xi) \right). \quad (3.11)$$

For the toroidal coordinate system, the vector potential for the velocity depends on η and ξ . Therefore, taking the curl of \mathbf{B} the stream function in two-dimensional flow is introduced as

$$U_\eta = \frac{q^2}{a^2 \sinh \eta} \frac{\partial \Psi_0}{\partial \xi}, \quad (3.12a)$$

$$U_\xi = -\frac{q^2}{a^2 \sinh \eta} \frac{\partial \Psi_0}{\partial \eta}, \quad (3.12b)$$

which automatically satisfies the continuity equation (2.7b). In order to show that the presented isolines are streamlines, the total differential of the Stokes stream function Ψ_0 has to be zero (Thomson, 1960). In toroidal coordinates

$$\frac{d\mathbf{l}}{ds} = \frac{a}{q} \frac{d\eta}{ds} \mathbf{e}_\eta + \frac{a}{q} \frac{d\xi}{ds} \mathbf{e}_\xi = \lambda \mathbf{U}_0, \quad (3.13)$$

where \mathbf{l} is the line element, s is the curvilinear line along the streamline, and λ is a constant. In other words, we find

$$d\eta = \lambda U_\eta \frac{a}{q} ds, \quad d\xi = \lambda U_\xi \frac{a}{q} ds. \quad (3.14)$$

Having the total differential of the stream function, it follows that

$$d\Psi_0 = \frac{\partial \Psi_0}{\partial \eta} d\eta + \frac{\partial \Psi_0}{\partial \xi} d\xi = -\frac{\sinh \eta}{q^2} U_\xi d\eta + \frac{\sinh \eta}{q^2} U_\eta d\xi = 0, \quad (3.15)$$

which confirms that Ψ_0 is the Stokes stream function. As it is mentioned before, using the current scaling we have $a = 1$.

The vorticity is derived from

$$\Omega_0 = \nabla \times \mathbf{U}_0 = q(\partial_\eta U_\xi - \partial_\xi U_\eta) - \sinh \eta U_\xi + \sin \xi U_\eta, \quad (3.16)$$

which can be written in terms of the stream function

$$\Omega_0 = -\frac{q^3}{\sinh \eta} [\partial_{\eta\eta} + \partial_{\xi\xi} + H_2\partial_\eta + H_3\partial_\xi] \Psi_0. \quad (3.17)$$

Since two different scalings of the governing equations have been employed in this work, the components of governing equations in toroidal coordinates for each scaling are presented separately.

3.2.2 Thermocapillary scaling

The relation connecting the vorticity and stream function is given in (3.17), which satisfies the continuity. Taking the curl of the momentum equation (2.7a) gives

$$\text{Re} [\nabla \times (\mathbf{U}_0 \cdot \nabla) \mathbf{U}_0] = \underbrace{-\nabla \times (\nabla P_0)}_{=0} + \nabla \times \nabla^2 \mathbf{U}_0 + \frac{\text{Gr}}{\text{Re}} (\nabla \times \theta_0 \mathbf{k}). \quad (3.18)$$

The term on the left side can be expanded to

$$\nabla \times (\mathbf{U}_0 \cdot \nabla) \mathbf{U}_0 = (\mathbf{U}_0 \cdot \nabla) \mathbf{\Omega}_0 - \underbrace{(\mathbf{\Omega}_0 \cdot \nabla) \mathbf{U}_0}_{=0 \text{ (for 2D flow)}} + \overbrace{\mathbf{\Omega}_0 (\nabla \cdot \mathbf{U}_0)}^{=0 \text{ (incomp. flow)}} + \underbrace{\mathbf{U}_0 (\nabla \cdot \mathbf{\Omega}_0)}_{\nabla \cdot \text{curl}=0}. \quad (3.19)$$

The only non-zero term $(\mathbf{U}_0 \cdot \nabla) \mathbf{\Omega}_0$ results in

$$(\mathbf{U}_0 \cdot \nabla) \mathbf{\Omega}_0 = q (U_\eta \partial_\eta \Omega_0 + U_\xi \partial_\eta \Omega_0) \mathbf{e}_\phi. \quad (3.20)$$

In the same manner, the second term on the right side of (3.18) becomes

$$\nabla \times (\nabla^2 \mathbf{U}_0) = \nabla^2 \mathbf{\Omega}_0 = \nabla^2 \Omega_0 \mathbf{e}_\phi, \quad (3.21)$$

and finally, considering the transformation from Cartesian to toroidal coordinates, the last term in (3.18) becomes

$$\begin{aligned} \nabla \times \theta_0 \mathbf{k} &= \nabla \times \left(\theta_0 \begin{bmatrix} -\sinh \eta \sin \xi / q \\ (\cosh \eta \cos \xi - 1) / q \\ 0 \end{bmatrix} \right) \\ &= \left[(\cosh \eta \cos \xi - 1) \partial_\eta + (\sinh \eta \sin \xi) \partial_\xi \right] \theta_0 \mathbf{e}_\phi. \end{aligned} \quad (3.22)$$

Moreover, from the energy equation (2.7c) we have

$$\text{Ma} (U_\eta \partial_\eta \theta_0 + U_\xi \partial_\xi \theta_0) = q [\partial_{\eta\eta} + \partial_{\xi\xi} - H_2 \partial_\eta - H_3 \partial_\xi] \theta_0. \quad (3.23)$$

Collecting all terms discussed above and expressing the velocity by the stream function considering (3.12), the vorticity-stream function formulation of the governing equations reads

$$\frac{q^3}{\sinh \eta} [\partial_{\eta\eta} + \partial_{\xi\xi} + H_2 \partial_\eta + H_3 \partial_\xi] \Psi_0 = -\Omega_0, \quad (3.24a)$$

$$\begin{aligned} q^2 [\partial_{\eta\eta} + \partial_{\xi\xi} - H_2 \partial_\eta - H_3 \partial_\xi] \Omega_0 &= \text{Re} \frac{q^3}{\sinh \eta} (\partial_\xi \Psi_0 \partial_\eta - \partial_\eta \Psi_0 \partial_\xi) \Omega_0 \\ &- \frac{\text{Gr}}{\text{Re}} \left[(\cosh \eta \cos \xi - 1) \partial_\eta + (\sinh \eta \sin \xi) \partial_\xi \right] \theta_0, \end{aligned} \quad (3.24b)$$

$$[\partial_{\eta\eta} + \partial_{\xi\xi} - H_2 \partial_\eta - H_3 \partial_\xi] \theta_0 = \text{Ma} \frac{q}{\sinh \eta} (\partial_\xi \Psi_0 \partial_\eta - \partial_\eta \Psi_0 \partial_\xi) \theta_0. \quad (3.24c)$$

For the vorticity-stream function formulation of the governing equations, the boundary conditions have to be defined. We start with the free surface boundary conditions as the thermocapillary driving force is determined along the liquid-gas interface. The heat transfer condition in toroidal coordinates is

$$\mathbf{e}_\xi \cdot \nabla \theta_0 = \text{Bi}(\theta_0 - \theta_a). \quad (3.25)$$

in which \mathbf{n} from (2.12) is substituted by $-\mathbf{e}_\xi$. Furthermore, the surface stress condition become

$$\mathbf{e}_\eta \cdot (\mathbf{S} \cdot \mathbf{e}_\xi) = \mathbf{e}_\eta \cdot \nabla \theta_0, \quad (3.26a)$$

$$\mathbf{e}_\phi \cdot (\mathbf{S} \cdot \mathbf{e}_\xi) = \mathbf{e}_\phi \cdot \nabla \theta_0 = 0, \quad \text{due to } \partial_\phi = 0, \quad (3.26b)$$

where $\mathbf{t}_1 = \mathbf{e}_\eta$ and $\mathbf{t}_2 = \mathbf{e}_\phi$. In two-dimensional form the viscous stress tensor is derived in toroidal coordinates as

$$\mathbf{S} = q \begin{bmatrix} 2 \left(\partial_\eta u_\eta - u_\xi \frac{\sin \xi}{q} \right) & \partial_\eta u_\xi + \partial_\xi u_\eta + u_\eta \frac{\sin \xi}{q} + u_\xi \frac{\sinh \eta}{q} & 0 \\ \partial_\eta u_\xi + \partial_\xi u_\eta + u_\eta \frac{\sin \xi}{q} + u_\xi \frac{\sinh \eta}{q} & 2 \left(\partial_\xi u_\xi - u_\eta \frac{\sinh \eta}{q} \right) & 0 \\ 0 & 0 & 0 \end{bmatrix}. \quad (3.27)$$

Therefore, from (3.26a) we have

$$\partial_\eta \theta_0 = q \left(\partial_\eta u_\xi + \partial_\xi u_\eta + u_\eta \frac{\sin \xi}{q} + u_\xi \frac{\sinh \eta}{q} \right). \quad (3.28)$$

Substituting the velocities by the stream function as in (3.12) gives

$$\partial_\eta \theta_0 = \frac{q^3}{\sinh \eta} \left[-\partial_{\eta\eta} + \partial_{\xi\xi} - \left(\frac{3 \sinh \eta}{q} - \frac{\cosh \eta}{\sinh \eta} \right) \partial_\eta + \frac{3 \sin \xi}{q} \partial_\xi \right] \Psi_0. \quad (3.29)$$

Defining $\Psi_0 = 0$ at all the boundaries, the terms $\partial_{\eta\eta}$ and ∂_η vanish along the free surface. On the other hand, using the vorticity and stream function relation (3.24), it is possible to rewrite (3.29) in the compact form of

$$\begin{aligned} \partial_\eta \theta_0 &= \frac{q^3}{\sinh \eta} \left[\partial_{\xi\xi} \Psi_0 + \frac{3 \sin \xi}{q} \partial_\xi \Psi_0 \right] \\ &= -\Omega_0 + \frac{q^3}{\sinh \eta} \left(\frac{2 \sin \xi}{q} \partial_\xi \Psi_0 \right). \end{aligned} \quad (3.30)$$

As a result, collecting (3.25) and (3.30) as well as considering the zero value of the stream function along all the boundaries, on the spherical free surface we impose

$$\left. \begin{aligned} \Psi_0 &= 0, \\ \partial_\xi \theta_0 &= \text{Bi}(\theta_0 - \theta_a), \\ \partial_\eta \theta_0 &= -\Omega_0 + \frac{2q^2 \sin \xi}{\sinh \eta} \partial_\xi \Psi_0 \end{aligned} \right\} \quad \text{on } \xi = \pi/2 \text{ (free surface),} \quad (3.31a)$$

and for the other boundaries of the domain we have

$$\partial_\eta \theta_0 = 0, \quad \Psi_0 = \Omega_0 = 0, \quad \text{on } \eta = 0, \text{ (vertical axis),} \quad (3.31b)$$

$$\theta_0 = \theta_w, \quad \Psi_0 = \partial_\xi \Psi_0 = 0, \quad \text{on } \xi = \pi, \text{ (flat plate).} \quad (3.31c)$$

where θ_w is the dimensionless temperature of the flat plate. It is either $\theta_w = 1$ for a heated or $\theta_w = 0$ for a cooled flat plate.

Moreover, for the boundary conditions at the contact line (3.40) as well as at the flat plate (3.31c) two conditions are imposed on Ψ_0 . Numerically it is not possible to satisfy both conditions for one variable; therefore, the Neumann boundary condition is required to be converted to a boundary condition on the vorticity Ω_0 (Lundgren and Koumoutsakos, 1999). For the flat plate the Neumann boundary condition on stream

function is substituted by

$$\Omega_0^{i,\text{end}} = -2 \frac{q^3}{\sinh \eta \Delta \xi_j} \Psi_0^{i,\text{end}-1}, \quad (3.32)$$

following the work of E and Liu (1996) and considering the differential vector operators in toroidal coordinates. In (3.32), superscripts (i, j) show the (η, ξ) coordinates of a node on the computational grid and $\Delta \xi_j = \xi_j - \xi_{j-1}$. Similar boundary condition on Ω_0 is obtained at the contact line.

3.2.3 Viscous scaling

The components of the governing equations in viscous scaling are obtained in a similar way as it is described in the previous subsection. The vorticity-stream function formulation of the governing equations in this case reads

$$\frac{q^3}{\sinh \eta} [\partial_{\eta\eta} + \partial_{\xi\xi} + H_2 \partial_\eta + H_3 \partial_\xi] \Psi_0 = -\Omega_0, \quad (3.33a)$$

$$\begin{aligned} q^2 [\partial_{\eta\eta} + \partial_{\xi\xi} - H_2 \partial_\eta - H_3 \partial_\xi] \Omega_0 &= \frac{q^3}{\sinh \eta} (\partial_\xi \Psi_0 \partial_\eta - \partial_\eta \Psi_0 \partial_\xi) \Omega_0 \\ &- \text{Gr} \left[(\cosh \eta \cos \xi - 1) \partial_\eta + (\sinh \eta \sin \xi) \partial_\xi \right] \theta_0, \end{aligned} \quad (3.33b)$$

$$[\partial_{\eta\eta} + \partial_{\xi\xi} - H_2 \partial_\eta - H_3 \partial_\xi] \theta_0 = \text{Pr} \frac{q}{\sinh \eta} (\partial_\xi \Psi_0 \partial_\eta - \partial_\eta \Psi_0 \partial_\xi) \theta_0. \quad (3.33c)$$

The boundary conditions are similar to the thermocapillary scaling case apart from the free surface boundary conditions for which the thermocapillary stresses are neglected and a free-slip boundary condition is introduced. The free-slip condition for the tangential velocity along the free surface gives

$$\partial_\xi U_\eta = 0. \quad (3.34)$$

Rewriting this condition in terms of the stream function using (3.12), we have

$$\partial_\xi \left(\frac{q^2}{a^2 \sinh \eta} \frac{\partial \Psi_0}{\partial \xi} \right) = 0 \Rightarrow \left(\partial_{\xi\xi} + \frac{2 \sin \xi}{q} \partial_\xi \right) \Psi_0 = 0. \quad (3.35)$$

Again, since the boundary condition $\Psi_0 = 0$ is applied on the stream function along all the domain boundaries, the free slip boundary condition has to be converted to a

vorticity boundary condition. From the vorticity and stream function relation (3.17) and considering that $\Psi_0 = 0$, the vorticity along the free surface is

$$\Omega_0 = -\frac{q^3}{\sinh \eta} [\partial_{\xi\xi} + H_3 \partial_\xi] \Psi_0. \quad (3.36)$$

Combining (3.35) and (3.36) results in the free slip boundary condition along the free surface as

$$\Omega_0 - \frac{q^2 \sin \xi}{\sinh \eta} \partial_\xi \Psi_0 = 0. \quad (3.37)$$

3.3 Numerical solution of the steady flow

To solve the governing equations numerically, the set of equations is discretized by finite differences on a non-uniform grid. In this section, the grid generation in toroidal coordinates, the discretization details, and the numerical method to solve the equations are presented.

3.3.1 Grid generation

In order to provide the adequate resolution in regions where large gradients appear (mostly along the boundaries), it is necessary to generate a non-uniform grid with a proper stretching. To distribute the grid points in η and ξ directions, the nature of toroidal coordinates has to be considered. The scale factors and transformation equations are characterized by hyperbolic functions. Therefore, these functions have been employed to define the stretching functions

$$\eta = c_1 [\tanh^{-1}(x_1)]^{c_2}, \quad x_1 \in [0, 0.5], \quad (3.38a)$$

$$\xi = \xi_{\text{mid}} + \tanh(x_2), \quad x_2 \in [\tanh^{-1}(-\xi_{\text{sym}}), \tanh^{-1}(\xi_{\text{sym}})], \quad (3.38b)$$

where $c_1 \in [12.25, 16]$ and $c_2 \in [1.05, 1.5]$ are the regulating coefficients which control the distribution of the nodes in η -direction, $\xi_{\text{mid}} = (\xi_{\text{max}} + \xi_{\text{min}})/2$ is the algebraic mean of the ξ coordinate and $\xi_{\text{sym}} = (\xi_{\text{max}} - \xi_{\text{min}})/2$ defines a symmetrical grid stretching starting from ξ_{mid} in both directions, toward ξ_{max} and ξ_{min} .

The distribution of N_η and N_ξ points is homogeneous in x_1 and x_2 , respectively. However, the stretching function in ξ direction (3.38b) is not suitable for all contact angles,

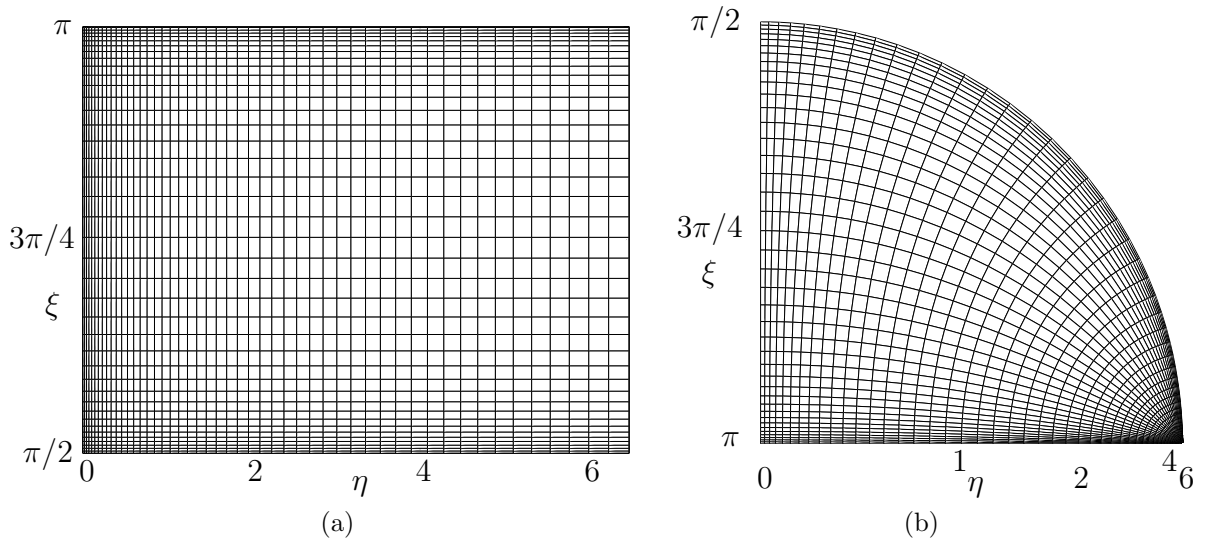


Figure 3.3: Computational grid in (η, ξ) -plane (a) and (x, y) -plane (b). Every fifth grid line is plotted in both directions for clarity. In (b), the values of η and ξ are shown along the x and y coordinates, respectively.

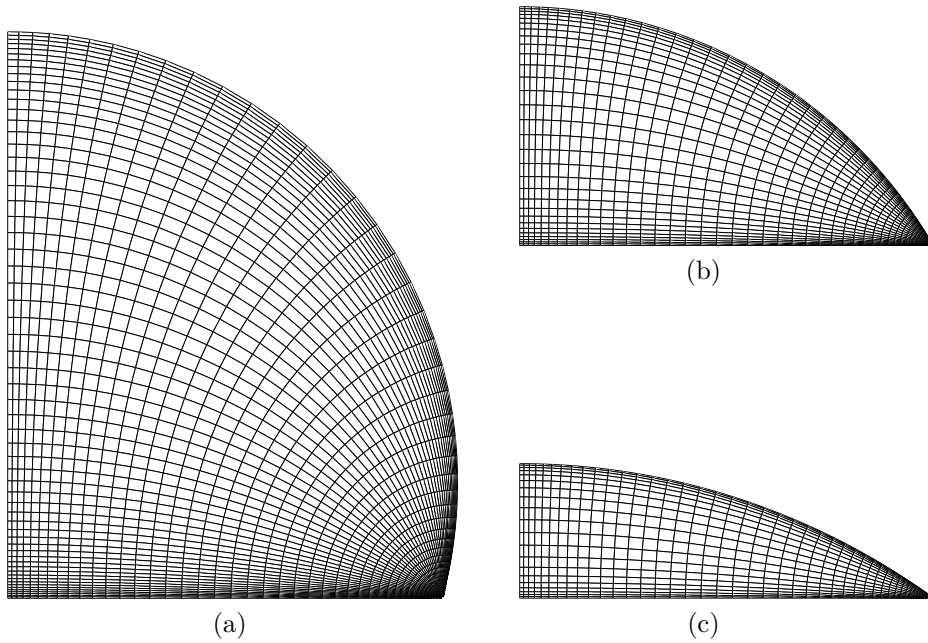


Figure 3.4: Computational grid in (x, y) -plane for different contact angles. (a) $\alpha = 105^\circ$, (b) $\alpha = 60^\circ$, and (c) $\alpha = 36^\circ$. Every fifth grid line is plotted in both directions for clarity.

since the applied inverse hyperbolic tangent function returns a real number only in the interval of $[-1, 1]$. For instance, for a droplet with the contact angle of $\alpha = 135^\circ$ the x_2 interval exceeds the limit of $[-1, 1]$ and becomes complex ($\tanh^{-1}(\xi_{\text{sym}}) = 1.25 + i(\pi/2)$). Furthermore, in case of shallow droplets, this function provides a weak stretching close to the boundaries and the grid points are almost uniformly distributed. The reason is that the inverse hyperbolic tangent function behaves almost linearly close to zero. In order to treat these problems and provide a similar stretching for droplets of different contact angles, equation (3.38b) is substituted by the following function

$$\xi = \xi_{\text{mid}} + \chi \tanh(x_2) \quad , \quad x_2 \in \left[\tanh^{-1} \left(-\frac{\xi_{\text{sym}}}{\chi} \right), \tanh^{-1} \left(\frac{\xi_{\text{sym}}}{\chi} \right) \right], \quad (3.39)$$

where χ is the normalized stretching factor and defined as $\chi = \xi_{\text{sym}}/0.95$. In other words, the normalized x_2 interval is set to $[\tanh^{-1}(-0.95), \tanh^{-1}(0.95)]$ independent of the contact angle. Consequently, choosing an appropriate number of nodes in ξ direction results in a similar stretching of the nodes for all contact angles.

Employing the stretching functions (3.38a) and (3.39), a suitable non-uniform grid can be obtained for any droplet contact angle. A sample grid for a droplet with the contact angle of $\alpha = 90^\circ$ is plotted in figure 3.3, showing the grid points in both (η, ξ) - and (x, y) -planes. To make the grid stretching visible, every fifth grid line is plotted in both η and ξ directions. Close to the contact line, an accumulation of the grid points is observed. This high resolution is, to some extent, required in this part of the domain, where a boundary layer may develop for high Reynolds numbers. However, an excessive accumulation of the nodes is not desired and has to be controlled. This issue is discussed later in this subsection.

More computational grids are presented in figure 3.4 for different contact angles ($\alpha = 105^\circ, 60^\circ$, and 36°). Comparing the stretching along the free surface as well as the flat substrate for different droplet shapes presented in figures 3.3 and 3.4 confirms that the applied stretching function (3.39) in ξ direction is properly defined.

At the droplet's contact line where $\eta \rightarrow \infty$ exists a singularity in toroidal coordinates. To numerically treat this singularity the full interval of the domain in η direction is reduced from $\eta \in [0, \infty)$ to $\eta \in [0, \eta_{\text{max}}]$ with a sufficiently large value of η such that the numerical results are not affected. It is clear that along the imposed cut an extra boundary condition has to be defined, which reads

$$\theta_0 = \theta_w, \quad \Psi_0 = \partial_\eta \Psi_0 = 0, \quad \text{on} \quad \eta = \eta_{\text{max}}, \quad (\text{contact line}), \quad (3.40)$$

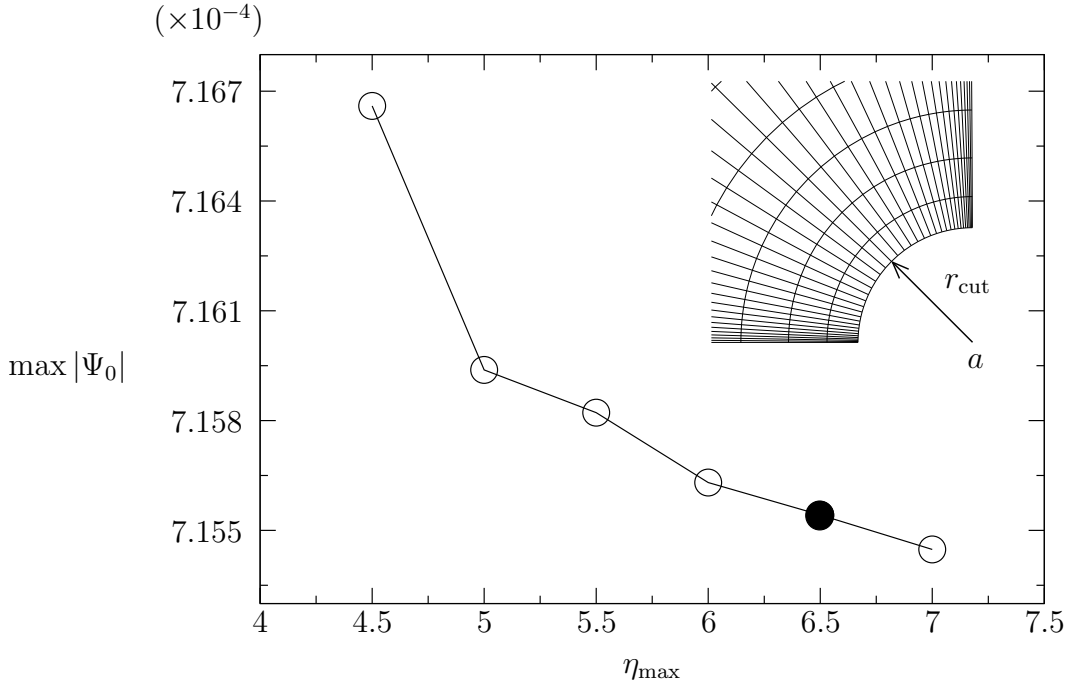


Figure 3.5: $\max_{\eta, \xi} |\Psi_0|$ as a function of η_{\max} . The parameters are $\text{Re} = 100$, $\text{Pr} = 4$, $\text{Gr} = 0$, $\text{Bi} = 0.1$, and $\alpha = \pi/2$. The highlighted point indicates the selected cut-off value of $\eta_{\max} = 6.5$. The cut is shown in the computational domain, where a is the focus of the coordinate system and r_{cut} is defined in (3.41).

Moreover, the nature of the toroidal coordinates exhibits an accumulation of grid points when $\eta \rightarrow \infty$. Therefore, the selected value of η_{\max} should assure that not only the solutions are not affected by the imposed cut, but also the unwanted grid refinement close to the contact line is avoided.

To select an optimum value for η_{\max} , some numerical solutions are selected to be shown here although the solution method is not presented yet. Figure 3.5 shows the extremum of the stream function within the domain as a function of η_{\max} . It is clear that, for $\eta_{\max} > 6$, the trend of $\max |\Psi_0|$ levels off. On the other hand, comparing the grid spacing for different values of η_{\max} leads to find an optimum value of $\eta_{\max} = 6.5$, which results to a cut of the computational domain (see figure 3.5) with a relatively small radius of

$$r_{\text{cut}} = 1 - \frac{\sinh \eta_{\max}}{1 + \cosh \eta_{\max}} = 3.00 \times 10^{-3}. \quad (3.41)$$

The selected value for η_{\max} has been considered in defining the intervals x_1 , c_1 , and c_2 in the grid stretching formulation (3.38a) in η direction.

3.3.2 Finite difference discretization

The governing equations are discretized by a second-order central difference scheme on a non-uniform grid which is specified in detail in the previous subsection. The centered difference first derivative approximation at a grid-point i of a function y in η -direction reads

$$\left. \frac{\partial y}{\partial \eta} \right|_i = \frac{\Delta_i^2(y_{i+1} - y_i) + \Delta_{i+1}^2(y_i - y_{i-1})}{\Delta_i \Delta_{i+1} (\Delta_i + \Delta_{i+1})} + \mathcal{O}(\Delta_i \Delta_{i+1}), \quad (3.42a)$$

where $\Delta_i = \eta_i - \eta_{i-1}$. Similarly, the centered difference second derivative approximation at a grid point i is defined as

$$\left. \frac{\partial^2 y}{\partial \eta^2} \right|_i = 2 \frac{\Delta_i(y_{i+1} - y_i) - \Delta_{i+1}(y_i - y_{i-1})}{\Delta_i \Delta_{i+1} (\Delta_i + \Delta_{i+1})} + \mathcal{O}(\Delta_i - \Delta_{i+1}), \quad (3.42b)$$

Furthermore, the forward and backward difference representations are

$$\begin{aligned} \left. \frac{\partial y}{\partial \eta} \right|_i^f &= - \frac{\Delta_{i+1}^2(y_{i+2} - y_i) - (\Delta_{i+1} + \Delta_{i+2})^2(y_{i+1} - y_i)}{\Delta_{i+2} \Delta_{i+1} (\Delta_{i+2} + \Delta_{i+1})} \\ &\quad + \mathcal{O}(\Delta_{i+2} \Delta_{i+1} (\Delta_{i+2} + \Delta_{i+1})), \end{aligned} \quad (3.43a)$$

$$\begin{aligned} \left. \frac{\partial y}{\partial \eta} \right|_i^b &= \frac{\Delta_i^2(y_{i-2} - y_i) - (\Delta_i + \Delta_{i-1})^2(y_{i-1} - y_i)}{\Delta_{i-1} \Delta_i (\Delta_{i-1} + \Delta_i)} \\ &\quad + \mathcal{O}(\Delta_{i-1} \Delta_i (\Delta_{i-1} + \Delta_i)), \end{aligned} \quad (3.43b)$$

which are employed to discretize the boundary condition equations.

For an equidistant grid, the presented scheme is second-order accurate. However, for a non-uniform grid it is first-order, but the local solution error can be controlled by limiting the grid growth factor $f = \Delta_{i+1}/\Delta_i$ in the range $[0.8, 1.2]$ (Fletcher, 1991). In most of the grids employed in this work, the growth factor varies in the interval of $[0.9, 1.1]$. A corresponding finite difference scheme is applied on ξ -direction.

Figure 3.6 sketches a nine-point stencil of the computational grid in the (η, ξ) -plane. The indexing which is employed here is a one-index notation, n , which is defined as

$$n = i + (j - 1)N_\eta, \quad (3.44)$$

where $i = 1, 2, \dots, N_\eta$ and $j = 1, 2, \dots, N_\xi$.

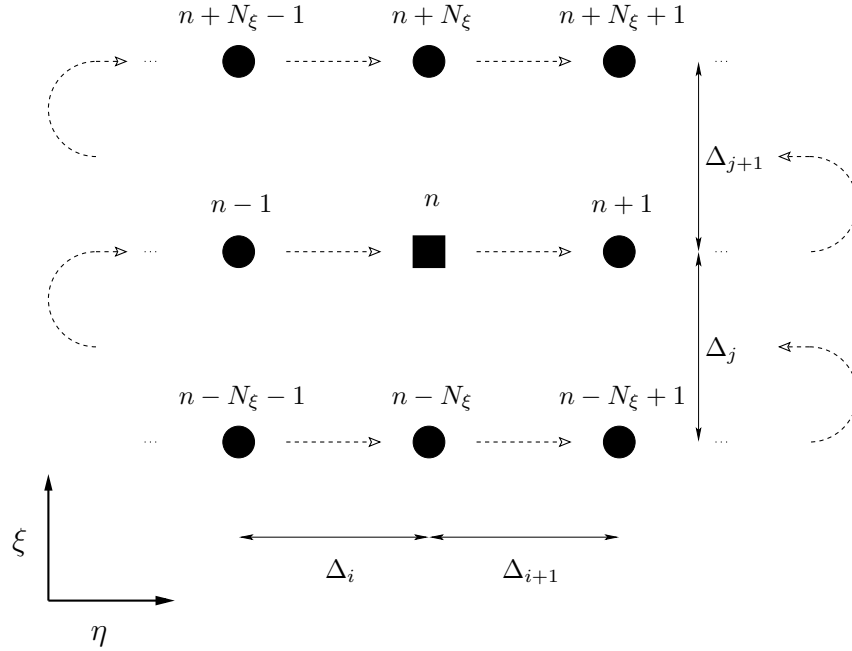


Figure 3.6: Grid indexing in η - ξ coordinates. N_η and N_ξ are the number of nodes in η and ξ directions, respectively. n is the index notation which varies between 1 and $N_\eta N_\xi$ and the dashed lines show the direction of the notation increment.

3.3.3 Newton's method

The sets of non-linear governing equations (3.24) as well as (3.33) are discretized using finite difference schemes which are given in (3.42) and (3.43). The discretized equations are then solved employing Newton's method with damping which is implemented in a Matlab code. When no damping is considered, this scheme ideally converges quadratically to the final solution (Kelley, 1995). Newton's method is an iterative solver which is defined by

$$\mathbf{J}(\mathbf{x}^n) \cdot \boldsymbol{\delta} = -\mathbf{f}(\mathbf{x}^n), \quad (3.45a)$$

$$\mathbf{x}^{n+1} = \mathbf{x}^n + \epsilon \boldsymbol{\delta}, \quad (3.45b)$$

where $\mathbf{x}^n = (\Psi_0, \Omega_0, \theta_0)^T$ is the actual solution (or the initial guess for the first iteration), \mathbf{J} is its Jacobian matrix, \mathbf{f} is a vector-valued function derived from the governing equations, and ϵ is the damping factor which varies between 0.5 and 0.9 in this study for different cases to optimize the convergence speed.

Here the linear system of equations (3.45a) is solved using the backslash operator

("\ \backslash ") in Matlab which computes the unknown vector \mathbf{x} in $\mathbf{A} \cdot \mathbf{x} = \mathbf{b}$, where \mathbf{A} is an $N \times N$ matrix and \mathbf{b} is a column vector with N components (Recktenwald, 2000). The employed algorithm to solve this equation depends on the structure of the matrix \mathbf{A} . Although generally the backslash operator implements the Gaussian elimination method, for the current case where \mathbf{A} is sparse and has real multiple diagonal elements, it attempts a Cholesky factorization instead. After a number of iterations when the value of the residual is smaller than the square root of the machine accuracy, 10^{-8} , the iterative solver converges and \mathbf{x}^{n+1} in (3.45b) is the solution vector.

3.4 Steady solver code verification

The present Matlab code which is employed to iteratively solve the Navier–Stokes equations is tested, comparing the numerical results with the Kovaszny flow which is an exact solution of the steady two-dimensional Navier–Stokes equations (Kovaszny, 1948). The Kovaszny flow in closed-form reads

$$\Psi = y - \frac{e^{\lambda x}}{2\pi} \sin 2\pi y, \quad (3.46a)$$

$$\Omega = \frac{\lambda^2 - 4\pi^2}{2\pi} e^{\lambda x} \sin 2\pi y, \quad (3.46b)$$

where

$$\lambda = \frac{\text{Re}}{2} - \sqrt{4\pi^2 + \frac{\text{Re}^2}{4}}, \quad (3.47)$$

depends only on the Reynolds number.

Since the Kovaszny flow exhibits a planar two-dimensional flow, to numerically treat it the implementation has to be done employing the bipolar coordinate system which has the axis of translation in third dimension (z -direction) instead of the toroidal coordinates with an axis of rotation (ϕ -direction) about $\eta = 0$; in other words, the scale factors are different for the third dimension. However, the formulations are the same for the two-dimensional case.

For the code verification an arbitrary computational domain is specified bounded with the intervals $\eta \times \xi \in [-1.5, 2.25] \times [\pi/2, 3\pi/2]$. For vorticity and stream function on all the boundaries Dirichlet boundary conditions are implemented which are derived from the exact solution (3.46). Then the stream function and vorticity are computed for all the interior grid-points using the iterative solver. The numerical results for streamlines

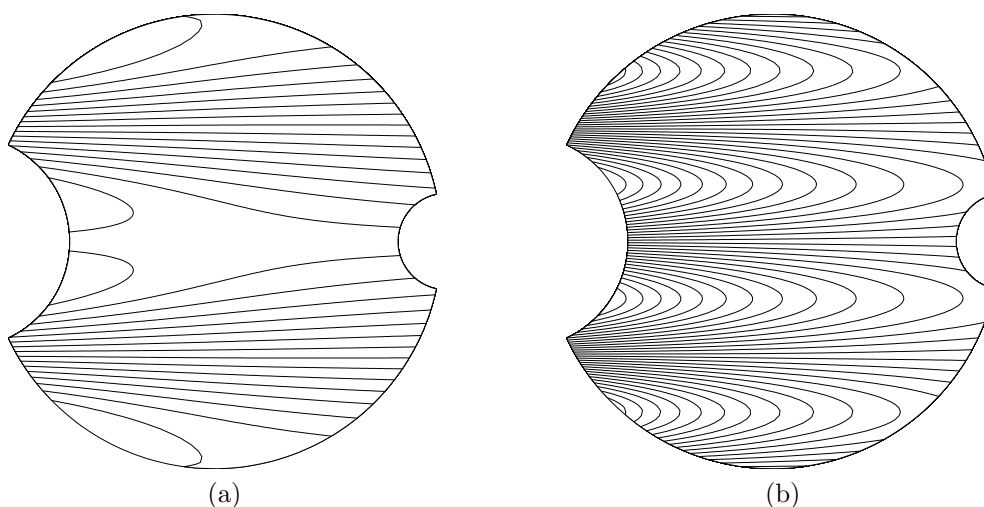


Figure 3.7: Computed stream function (a) and vorticity (b) for the Kovasznay flow at $\text{Re} = 40$. An arbitrarily chosen computational domain bounded by $\eta \times \xi \in [-1.5, 2.25] \times [\pi/2, 3\pi/2]$ has been considered.

and vorticity are plotted in figure 3.7.

Numerical computations are repeated for different grid sizes, from 40×40 up to 240×240 in order to study the rate of convergence of the numerical scheme. The infinity norm of the deviation between the exact and computed stream function is shown in figure 3.8 as a function of the grid size $N = \sqrt{N_\eta N_\xi}$. The slope of the curve confirms the second-order convergence rate of the iterative solver for the employed equidistant grid.

To assess the convergence of the grid some numerical results are presented in table 3.1 which lists the Stokes stream function extremum, $|\Psi|_{\max}$, together with the vorticity at

Grid size	Pr = 0.02		Pr = 4		Pr = 28	
	$ \Psi _{\max} \times 10^4$	$-\Omega_{\text{core}}$	$ \Psi _{\max} \times 10^4$	$-\Omega_{\text{core}}$	$ \Psi _{\max} \times 10^4$	$-\Omega_{\text{core}}$
50×25	5.697	0.0361	7.126	0.0452	5.406	0.0333
100×50	5.781	0.0353	7.148	0.0454	5.206	0.0327
200×100	5.832	0.0368	7.156	0.0446	5.133	0.0317
400×200	5.843	0.0367	7.163	0.0448	5.112	0.0317

Table 3.1: Stokes stream function extremum $|\Psi|_{\max}$ and vorticity Ω_{core} at the center of the toroidal vortex for different non-equidistant grids $N_\eta \times N_\xi$. The parameters are $\text{Re} = 100$, $\text{Bi} = 0.1$, $\text{Gr} = 0$, and $\alpha = \pi/2$.

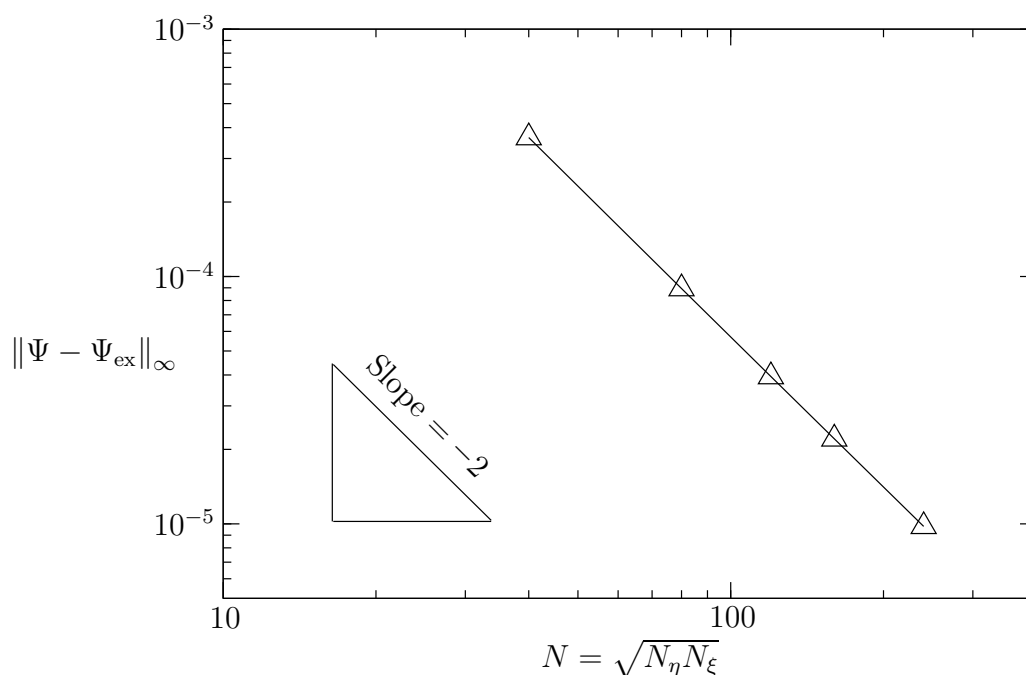


Figure 3.8: Infinity norm of the numerical error of Ψ on a uniform grid as a function of grid size for $N_\eta = N_\xi$ (equidistant grid).

the position of $|\Psi|_{\text{max}}$ (center of the toroidal vortex, see figure 4.1), Ω_{core} , for a number of different grid sizes. A grid size of $N_\eta \times N_\xi = 200 \times 100$ has been chosen for all the computations according to the obtained results. However, in some cases with extremely high gradients near the liquid-gas interface or the flat substrate, finer grids with the size of maximum $N_\eta \times N_\xi = 400 \times 200$ have been employed. The reason for having twice the number of nodes in η -direction as compared to ξ -direction is traced back to the nature of the toroidal coordinate system in which the grid points are accumulating close to the focus of the coordinate system $(a, 0)$. Therefore, more nodes in this direction are required to keep the aspect ratio of each computational cell within a reasonable limit (see figure 3.3). However, in case of droplets with a larger (smaller) contact angle, $\alpha > 90^\circ$ ($\alpha < 90^\circ$), the number of nodes in ξ -direction has been increased (decreased) accordingly.

The energy equation is verified considering a creeping flow ($\text{Re} \rightarrow 0$) in the absence of gravity ($\text{Gr} = 0$) in sessile droplets of different contact angles ($\alpha = 105^\circ$ and $\alpha = 75^\circ$), with $\text{Bi} \rightarrow \infty$. With these assumptions the convective heat transfer is negligible and the temperature along the free surface is equal to the ambient temperature at the same level. Therefore, pure conductive heat transfer is expected in the domain. The horizontal isotherms shown in figure 3.9 confirm the pure conduction within the domain for these two different drop shapes.

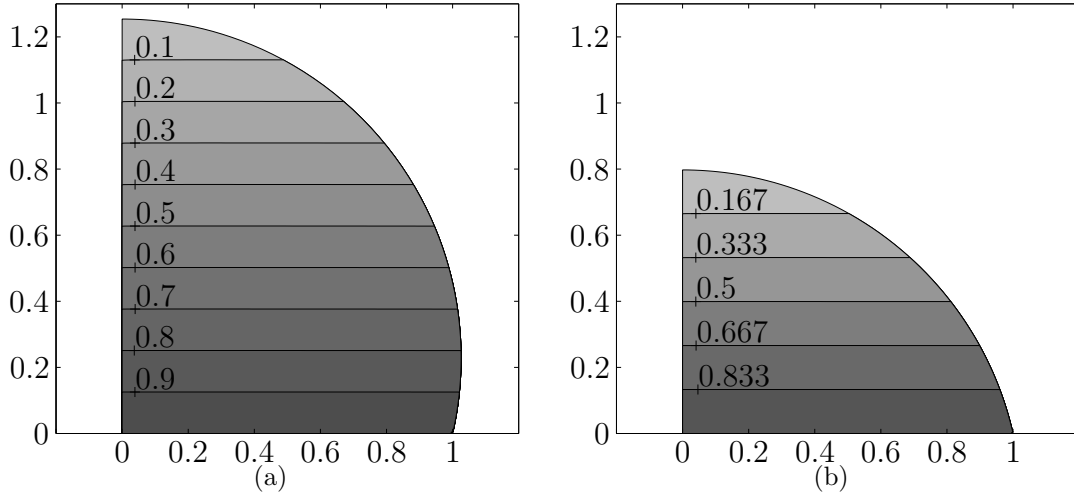


Figure 3.9: Isotherms; labels show the non-dimensional temperature $\theta_0 \in [0, 1]$ for droplets with contact angles of (a) 105° and (b) 75° . The parameters are $Re \rightarrow 0$, $Pr = 4$, $Bi \rightarrow \infty$, and $Gr = 0$.

3.5 Linear stability equations

Recalling the normal mode ansatz (2.24) and considering two-dimensional axisymmetric perturbations ($m = 0$), the solution of (2.19) can be obtained using the vorticity-stream function formulation as in the basic state

$$\psi(\eta, \xi, t) = \Psi_0 + \tilde{\psi}, \quad \omega(\eta, \xi, t) = \Omega_0 + \tilde{\omega}, \quad \theta(\eta, \xi, t) = \theta_0 + \tilde{\theta}, \quad (3.48)$$

and the normal modes can be written as

$$\begin{pmatrix} \tilde{\psi} \\ \tilde{\omega} \\ \tilde{\theta} \end{pmatrix}(\eta, \xi, t) = \begin{pmatrix} \hat{\psi} \\ \hat{\omega} \\ \hat{\theta} \end{pmatrix}(\eta, \xi) e^{-\gamma t} + c.c. \quad (3.49)$$

with $\gamma = \mu + i\omega \in \mathbb{C}$. Inserting (3.48) in the governing equations (3.24), subtracting the basic flow, and linearizing the equations by neglecting the quadratic terms, the linear stability equations (thermocapillary scaling) read

$$0 = \hat{\omega} + [\partial_{\eta\eta} + \partial_{\xi\xi} - H_2 - H_3 \partial_\xi] \hat{\psi}, \quad (3.50a)$$

$$\begin{aligned} \gamma \text{Re} \hat{\omega} = & q^2 \left[\partial_{\eta\eta} + \partial_{\xi\xi} - \left(H_2 + \text{Re} \frac{q}{\sinh \eta} \partial \Psi_0 \right) \partial_\eta \right. \\ & \left. - \left(H_3 - \text{Re} \frac{q}{\sinh \eta} \partial_\eta \Psi_0 \right) \partial_\xi \right] \hat{\omega} - \text{Re} \frac{q^3}{\sinh \eta} \left[\partial_\xi \hat{\psi} \partial_\eta - \partial_\eta \hat{\psi} \partial_\xi \right] \Omega_0 \\ & - \frac{\text{Gr}}{\text{Re}} \left[(\cosh \eta \cos \xi - 1) \partial_\eta + (\sinh \eta \sin \xi) \partial_\xi \right] \hat{\theta}, \end{aligned} \quad (3.50b)$$

$$\begin{aligned} \gamma \text{Ma} \hat{\theta} = & \left[\partial_{\eta\eta} + \partial_{\xi\xi} - \left(H_2 + \text{Ma} \frac{q}{\sinh \eta} \partial \Psi_0 \right) \partial_\eta \right. \\ & \left. - \left(H_3 - \text{Ma} \frac{q}{\sinh \eta} \partial_\eta \Psi_0 \right) \partial_\xi \right] \hat{\theta} - \text{Ma} \frac{q}{\sinh \eta} \left[\partial_\xi \hat{\psi} \partial_\eta - \partial_\eta \hat{\psi} \partial_\xi \right] \theta_0. \end{aligned} \quad (3.50c)$$

The boundary conditions for this case are similar to the basic flow case with some minor modifications. The boundary conditions for vorticity and stream function remain unchanged, whereas the boundary conditions for temperature are slightly different at the flat plate and the contact line. Moreover, a Neumann boundary condition is imposed at the symmetry line. The set of boundary conditions reads

$$\left. \begin{aligned} \hat{\psi} &= 0, \\ \partial_\xi \hat{\theta} &= \text{Bi} \hat{\theta}, \\ \partial_\eta \hat{\theta} &= -\hat{\omega} + \frac{2q^2 \sin \xi}{\sinh \eta} \partial_\xi \hat{\psi} \end{aligned} \right\} \text{ on } \xi = \pi/2 \text{ (free surface),} \quad (3.51a)$$

$$\partial_\eta \hat{\theta} = 0, \quad \hat{\psi} = \hat{\omega} = 0, \quad \text{on } \eta = 0, \text{ (vertical axis),} \quad (3.51b)$$

$$\hat{\theta} = 0, \quad \hat{\psi} = \partial_\eta \hat{\psi} = 0, \quad \text{on } \eta = \eta_{\max}, \text{ (contact line),} \quad (3.51c)$$

$$\hat{\theta} = 0, \quad \hat{\psi} = \partial_\xi \hat{\psi} = 0, \quad \text{on } \xi = \pi, \text{ (flat plate).} \quad (3.51d)$$

Similarly, for the case of pure buoyant flow we can write the linear stability equations in vorticity-stream function form. The linear stability equations in this case are

$$0 = \hat{\omega} + [\partial_{\eta\eta} + \partial_{\xi\xi} - H_2 - H_3 \partial_\xi] \hat{\psi}, \quad (3.52a)$$

$$\begin{aligned} \gamma\hat{\omega} = & q^2 \left[\partial_{\eta\eta} + \partial_{\xi\xi} - \left(H_2 + \frac{q}{\sinh \eta} \partial \Psi_0 \right) \partial_\eta \right. \\ & \left. - \left(H_3 - \frac{q}{\sinh \eta} \partial_\eta \Psi_0 \right) \partial_\xi \right] \hat{\omega} - \frac{q^3}{\sinh \eta} \left[\partial_\xi \hat{\psi} \partial_\eta - \partial_\eta \hat{\psi} \partial_\xi \right] \Omega_0 \end{aligned} \quad (3.52b)$$

$$- \text{Gr} \left[(\cosh \eta \cos \xi - 1) \partial_\eta + (\sinh \eta \sin \xi) \partial_\xi \right] \hat{\theta},$$

$$\begin{aligned} \gamma \text{Pr} \hat{\theta} = & \left[\partial_{\eta\eta} + \partial_{\xi\xi} - \left(H_2 + \text{Pr} \frac{q}{\sinh \eta} \partial \Psi_0 \right) \partial_\eta \right. \\ & \left. - \left(H_3 - \text{Pr} \frac{q}{\sinh \eta} \partial_\eta \Psi_0 \right) \partial_\xi \right] \hat{\theta} - \text{Pr} \frac{q}{\sinh \eta} \left[\partial_\xi \hat{\psi} \partial_\eta - \partial_\eta \hat{\psi} \partial_\xi \right] \theta_0, \end{aligned} \quad (3.52c)$$

with the same boundary conditions as in (3.51a) except along the free surface where a free-slip boundary condition has to be imposed. Considering this boundary condition from the basic state (3.37) we have

$$\hat{\omega} - \frac{q^2 \sin \xi}{\sinh \eta} \partial_\xi \hat{\psi} = 0. \quad (3.53)$$

In both cases, the stability problem represents a real, singular, generalized eigenvalue problem in the form of

$$\mathbf{A} \hat{\mathbf{x}} = \gamma \mathbf{B} \hat{\mathbf{x}}, \quad (3.54)$$

where $\hat{\mathbf{x}} = (\hat{\psi}, \hat{\omega}, \hat{\theta})^T$ are the eigenvectors, \mathbf{A} is a non-singular, asymmetric coefficient matrix, and \mathbf{B} is a diagonal singular coefficient matrix. The generalized eigenvalue problem (3.54) is solved using the Matlab's *eigs* command which employs an implicitly restarted Arnoldi iteration (Arnoldi, 1951; Mahajan et al., 1991; Lehoucq and Sorensen, 1996). However, since \mathbf{B} is singular, this method cannot be directly implemented. Therefore, a two-step transformation which serves as a preconditioner for the eigenvalue problem is implemented, as thoroughly discussed in the work of Lanzerstorfer and Kuhlmann (2012). The first step is a shift-invert transformation with zero shift, which gives the eigenvalues with the smallest absolute value, and the second step is a Cayley transformation to assure that no critical eigenvalue is missed in the first step (Kooper et al., 1995).

As it is explained above, in an axisymmetric two-dimensional linear stability problem, the most dangerous mode can be found by obtaining the smallest real part of the decay rate, μ_{\min} . The flow is linearly stable or unstable, if $\mu_{\min} > 0$ or $\mu_{\min} < 0$, respectively. For more details on eigenvalue-detection strategies and methods of root-finding, readers

Chapter 3 Numerical Implementation

are referred to Wright and Trefethen (2001) and Lanzerstorfer and Kuhlmann (2012).

Chapter 4

Basic State Results

In this chapter, the computational results are presented for four general cases of sessile/hanging drops attached to heated/cooled substrates, varying a wide range of parameters such as contact angle α , Re, Pr, Bi, and Gr. For all cases, the numerical results are provided in streamlines and isotherms shown on the left and right half of each droplet, respectively. Streamlines and isotherms are generally at equidistant levels. The direction of the fluid flow in vortices is indicated by plus/minus sign (\pm) for counter-clockwise/clockwise rotation at the core of each vortex. However, when not indicated, the direction of the flow is clockwise on the left half of the droplet. In most of the cases, a list of quantitative data is provided in a table in order to facilitate the comparisons. For simplicity, all the subscripts "0" of the basic state variables are omitted, e.g. $\Psi_0 \Rightarrow \Psi$.

4.1 Heated substrate

For the case of the droplet attached to a heated plate, the dimensionless temperature of the atmosphere varies linearly between the substrate, $\theta_a(0) = 1$, and a distance l above (or below) the substrate, $\theta_a(l) = 0$, where l is the dimensionless maximum height of the droplet. This temperature difference leads to heat transfer between the liquid droplet and the passive ambient which generates a temperature gradient along the liquid-gas interface and in the bulk liquid. The interfacial temperature gradient results in a surface tension gradient which drives the fluid flow, whereas the bulk temperature gradient leads to buoyant flow motion in presence of gravity. In this section, results for thermocapillary-driven, buoyancy-driven, and mixed buoyant-thermocapillary-driven flows are presented.

4.1.1 Thermocapillary-driven flow

In the absence of gravity, thermocapillary stresses along the liquid-gas interface are the only driving forces. Generally, the aim of this work is to provide a parametric study for both sessile and hanging droplets, but in the zero gravity conditions there is no difference between these two setups. Therefore, a sessile droplet is presented for all the zero gravity cases.

The first parameter to be considered is the thermocapillary Reynolds number, Re . Figure 4.1 shows the flow and temperature field for three different liquids ($Pr = 0.02$, 4, and 28 representing liquid metal, acetone, and silicon oil, respectively) when the Reynolds number varies. Each column presents a liquid material with different Prandtl number, and the Reynolds number increases from top to bottom. For a very low Reynolds number, $Re = 1$, the flow and temperature fields are nearly the same for all Prandtl numbers. The effect of the thermocapillarity on the fluid flow for $Pr = 0.02$ is negligible for the given range of Reynolds numbers as thermal diffusion dominates. This can be visually observed comparing figures 4.1a with 4.1m. However, for higher Prandtl numbers, the convective heat transport along the free surface can be observed when the Reynolds number increases especially for the case of $Pr = 28$ (see figure 4.1o). A more quantitative comparison of these cases is provided in table 4.1 which lists the temperature at the apex of the droplet, θ_{apex} , as well as the stream function extremum, $|\Psi|_{\text{max}}$, for the given cases in figure 4.1.

For larger Reynolds numbers, a thermal boundary layer develops along the liquid-gas interface. The evolution of this boundary layer is illustrated in figure 4.2 for $Pr = 28$ and $Bi = 1$. As the thermal boundary layer develops by increasing the Reynolds number, a region with a constant temperature grows at the center of the toroidal

Re	Pr = 0.02		Pr = 4		Pr = 28	
	θ_{apex}	$ \Psi _{\text{max}} \times 10^4$	θ_{apex}	$ \Psi _{\text{max}} \times 10^4$	θ_{apex}	$ \Psi _{\text{max}} \times 10^4$
1	0.8871	5.777	0.8870	5.792	0.8862	5.882
10	0.8871	5.782	0.8858	5.932	0.8782	6.798
100	0.8871	5.832	0.8758	7.156	0.9013	5.133
250	0.8870	5.922	0.8807	6.987	0.9214	3.665
1000	0.8864	6.413	0.9121	4.727	0.9449	2.189

Table 4.1: Temperature at the drop's apex and stream function extremum $\max |\Psi|$ for the cases shown in figure 4.1.

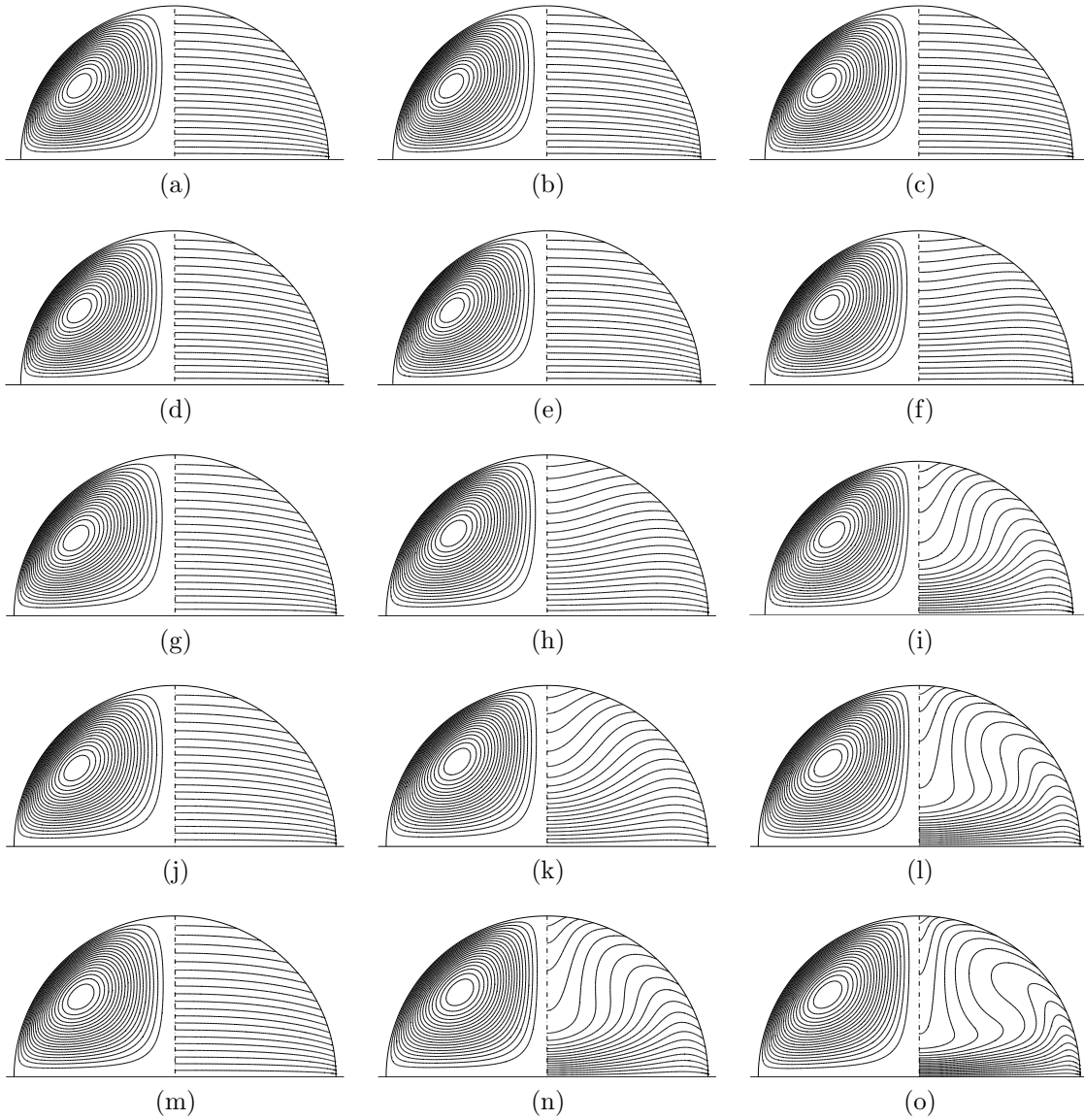


Figure 4.1: Reynolds number variation for $Pr = 0.02$ (left column), $Pr = 4$ (middle column), and $Pr = 28$ (right column), for $Gr = 0$, $\theta_w = 1$, $\alpha = \pi/2$, and $Bi = 0.1$. (a,b,c) $Re = 1$, (d,e,f) $Re = 10$, (g,h,i) $Re = 100$, (j,k,l) $Re = 250$, (m,n,o) $Re = 1000$. For each droplet: streamlines (left) and isotherms (right).

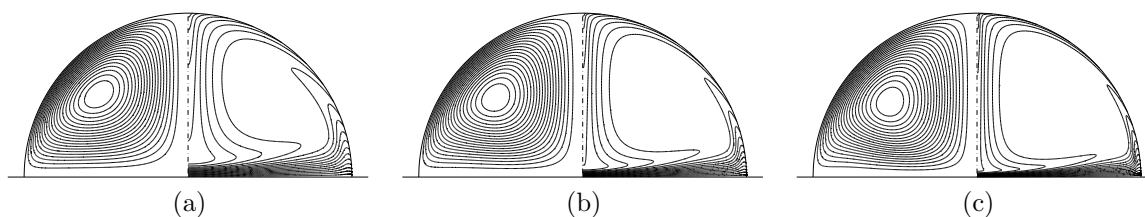


Figure 4.2: Thermal boundary layer evolution for $Pr = 28$, $Bi = 1$, $Gr = 0$, $\theta_w = 1$, $\alpha = \pi/2$, (a) $Re = 1000$, (b) $Re = 3000$, and (c) $Re = 8000$.

vortex. For $Re = 8000$ which is presented in figure 4.2c, this constant temperature region occupies all the inner bulk of the droplet which leads to large temperature gradients along the boundaries, especially close to the substrate. For such cases with steep gradients close to the boundaries, a computational grid with higher resolution is employed to ensure the accuracy. Here a larger Biot number is chosen to further strengthen the thermal boundary layer. The difference can be seen by comparing figures 4.1o and 4.2a with the same parameters except the Biot number. The influence of the Biot number on the flow field will be further discussed later in this chapter.

The stream function profiles are shown in figure 4.3a for a constant Marangoni number $Ma = 2800$, which can be obtained by varying Reynolds and Prandtl numbers simultaneously. In this figure, the stream function is plotted as a function of ξ along a line $\eta = \text{constant}$ which passes through the extremum of $|\Psi|$, as illustrated in figure 4.3b. For $Pr = 0.02$ the flow structure is different from the higher Prandtl number cases, since the flow is inertial ($Re = Ma/Pr = 1.4 \times 10^5$). However, the structure of the toroidal vortex is quite similar for the higher Prandtl numbers. By increasing the Prandtl number the curves converge to a limit curve. Furthermore, figure 4.4 illustrates the streamlines and the isotherms for some of the cases discussed in figure 4.3.

Although the flow behaves differently for low and high Prandtl numbers, the temperature field is quite similar for all the cases. In order to confirm these similarities, table 4.2 lists some characteristic parameters for different Prandtl numbers and for a constant Marangoni number. Even though for $Pr = 0.02$ the stream function extremum, vorticity, and the position of vortex center is quite different from the other cases, the temperature at the apex of the droplet is roughly the same as the ones for larger Prandtl numbers.

In order to thoroughly analyze the vortex structure for different liquids, i.e. different Prandtl numbers, a wide range of Marangoni numbers has to be considered. Figure 4.5 shows the global extremum of the stream function as a function of Marangoni

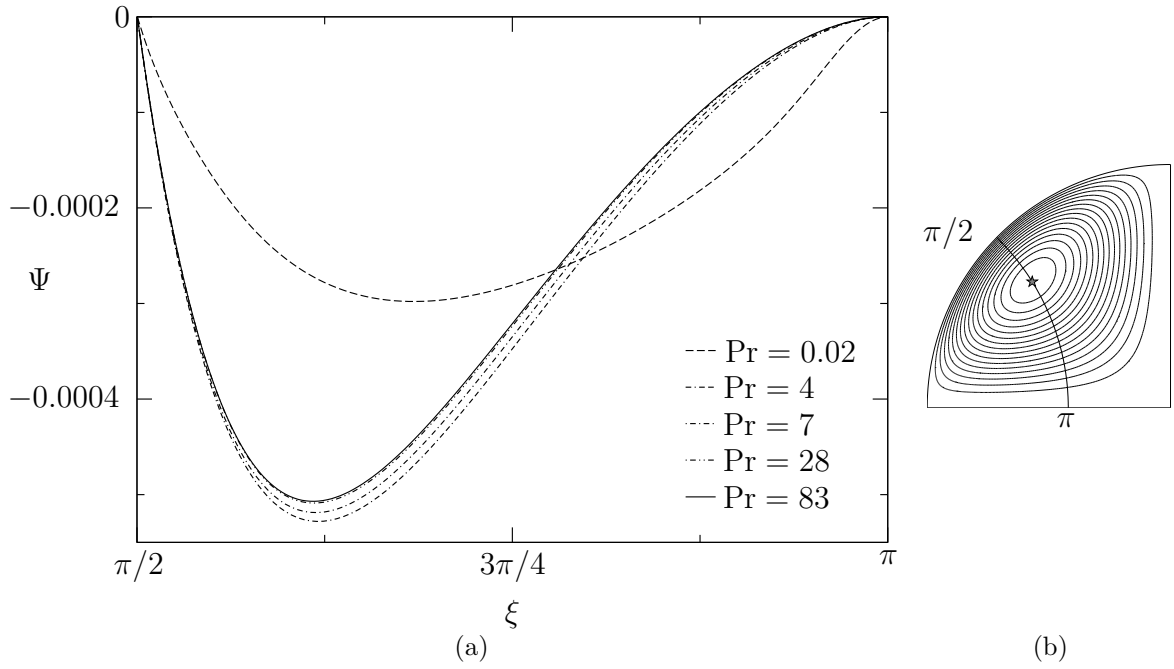


Figure 4.3: (a) Stream function Ψ versus ξ along a line $\eta = \text{constant}$ which passes through the streamfunction minimum Ψ_{\min} ; see (b). The parameters are $\text{Ma} = \text{RePr} = 2800$, $\text{Bi} = 0.1$, $\text{Gr} = 0$, $\theta_w = 1$, and $\alpha = \pi/2$.

Pr	$ \Psi _{\max} \times 10^4$	Ω_{core}	θ_{apex}	Center of vortex ($ x , y$)
0.02	2.979	-0.0133	0.8915	(0.574, 0.392)
4	5.280	-0.0323	0.9043	(0.547, 0.531)
7	5.188	-0.0317	0.9032	(0.558, 0.524)
28	5.101	-0.0312	0.9021	(0.568, 0.518)
83	5.070	-0.0314	0.9025	(0.568, 0.521)

Table 4.2: Stream function extremum, vorticity at the vortex core, apex temperature, and coordinate of the center of the vortex in Cartesian coordinates (x, y) for different Prandtl numbers. The parameters are the same as in figure 4.3.

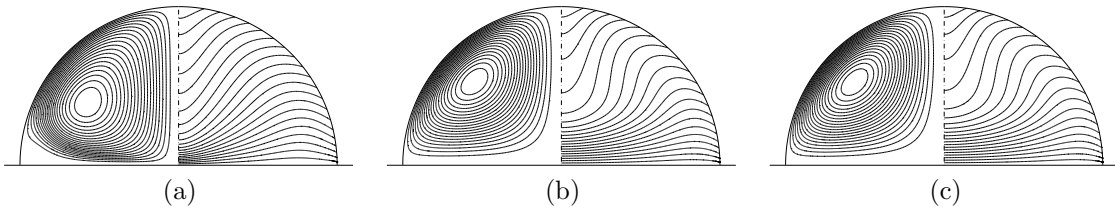


Figure 4.4: Constant Marangoni number, $\text{Ma} = 2800$ for $\text{Bi} = 0.1$, $\text{Gr} = 0$, $\theta_w = 1$, $\alpha = \pi/2$, (a) $\text{Pr} = 0.02$, (b) $\text{Pr} = 4$, and (c) $\text{Pr} = 28$.

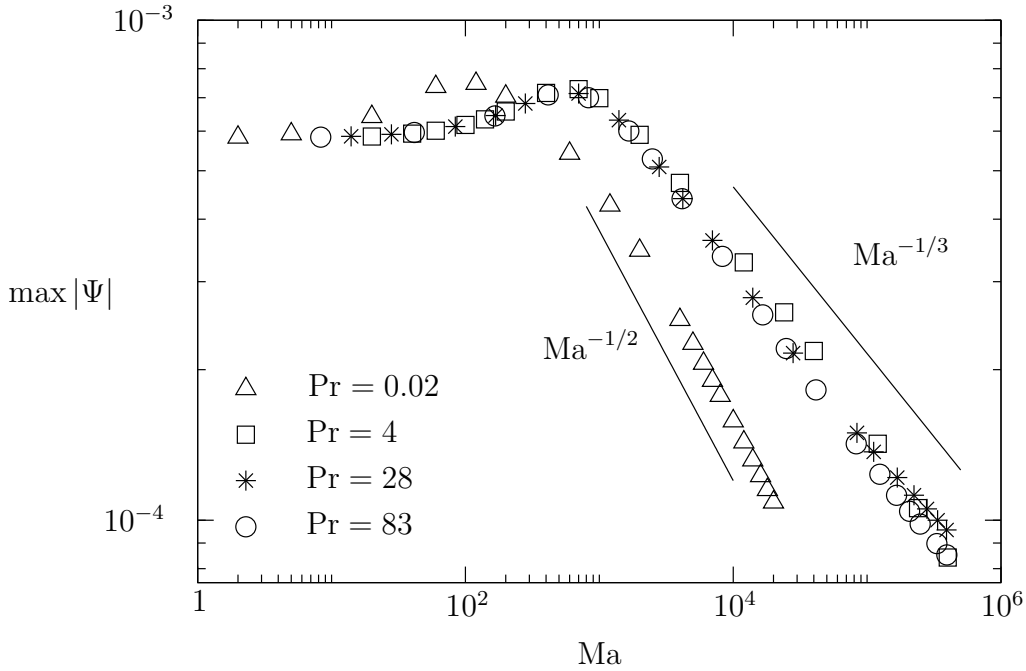


Figure 4.5: Maximum of $|\Psi|$ as a function of Ma (thermocapillary scaling, see table 2.1). The parameters are $Bi = 0.1$, $Gr = 0$, $\theta_w = 1$, and $\alpha = \pi/2$.

number for different liquid materials. In all the cases, the stream function extremum increases by increasing the Marangoni number up to a maximum value and then decreases monotonically. However, for the presented setup, this maximum is almost constant (at $Ma \approx 700$) except for the low Prandtl number case in which the maximum occurs at $Ma \approx 100$.

For $Pr = 0.02$ in the asymptotic case of large Marangoni numbers, the trend of the curve is well estimated by the slope of $-1/2$. However, the asymptotic trend in the case of higher Prandtl numbers is different and has the slope of approximately $-1/3$. Although there are some deviations from this slope, e.g. for $Pr = 28$, generally this asymptotic trend is fitted well to all liquids with $Pr > 1$. This scaling ($\max |\Psi| \sim Ma^{-1/3}$) is close to the classical inertial conductive scaling (Kuhlmann, 1999) as the temperature is nearly evenly distributed over the free surface. Nevertheless, confirming both asymptotic trends analytically is still an open question. It should be noted that the boundary layers are very thin in the limit of large Marangoni numbers. As a result, the cut-out of the domain, r_{cut} (see figure 3.5), may affect the evolution of boundary layers. To avoid this, for all computations in the limit of large Marangoni numbers, the value of η_{max} has been modified such that $r_{\text{cut}} < 10^{-6}$. This modification of the computational domain ensures that the evolution of boundary layers are not affected by r_{cut} .

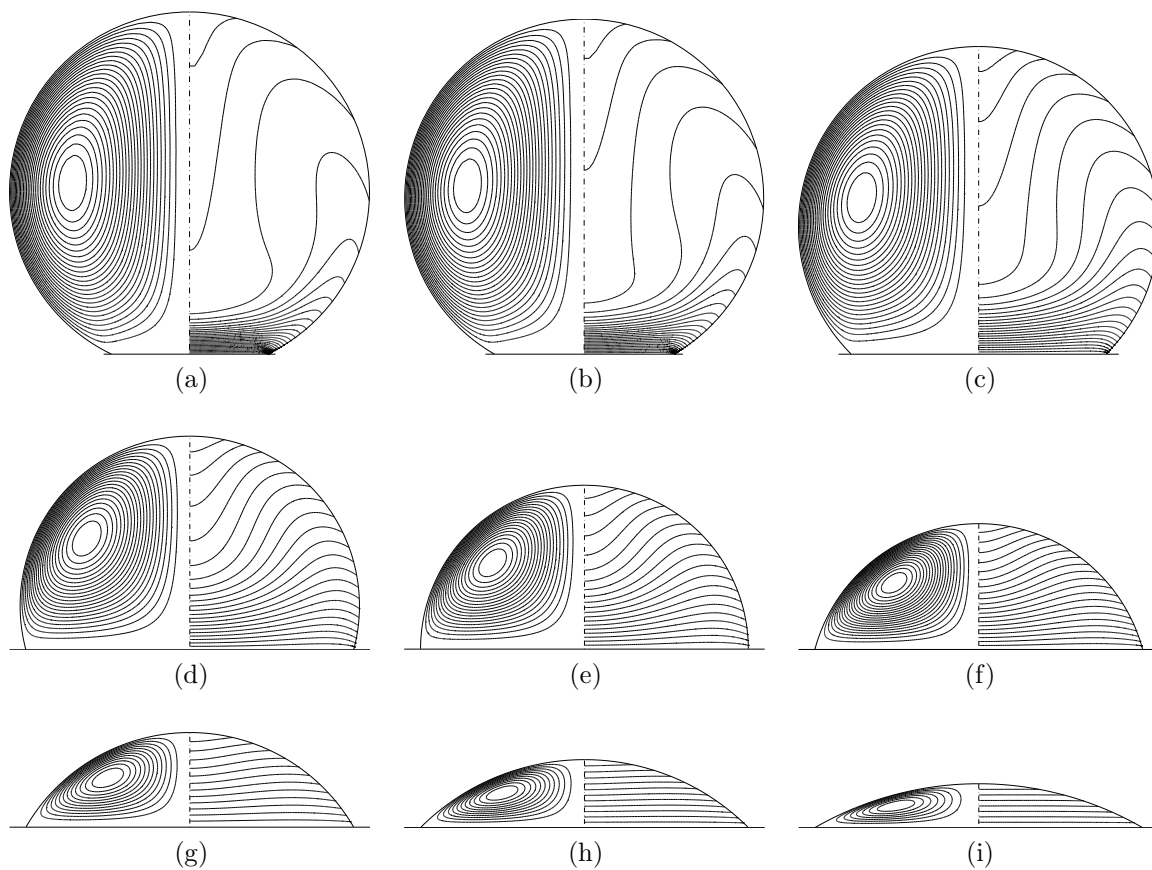


Figure 4.6: Streamlines and isotherms for (a) $\alpha = 155^\circ$, (b) $\alpha = 150^\circ$, (c) $\alpha = 144^\circ$, (d) $\alpha = 105^\circ$, (e) $\alpha = 90^\circ$, (f) $\alpha = 75^\circ$, (g) $\alpha = 60^\circ$, (h) $\alpha = 45^\circ$, and (i) $\alpha = 30^\circ$. The parameters are $Re = 250$, $Pr = 4$, $Gr = 0$, $\theta_w = 1$, and $Bi = 0.1$.

The next important parameter to be considered is the contact angle. Depending on the substrate material, the droplet can have different shapes with different contact angles; from very large contact angle for hydrophobic surfaces to shallow drops with small contact angles for hydrophilic substrates. Employing the toroidal coordinates, it is quite straightforward to generate different droplet shapes by adjusting only ξ_{\min} which fits to the liquid-gas interface.

Drops with a wide range of contact angles are shown in figure 4.6. For the same parameters, the convection is vigorous for droplets of large contact angles (see the isotherms in figures 4.6a to 4.6c). In this case, the downward flow along the symmetry line compresses the isotherms close to the substrate at the center of the droplet. Moreover, along the free surface the convective heat transport is much stronger than in the shallow droplets, e.g. figure 4.6i, where the heat transfer is mainly conductive

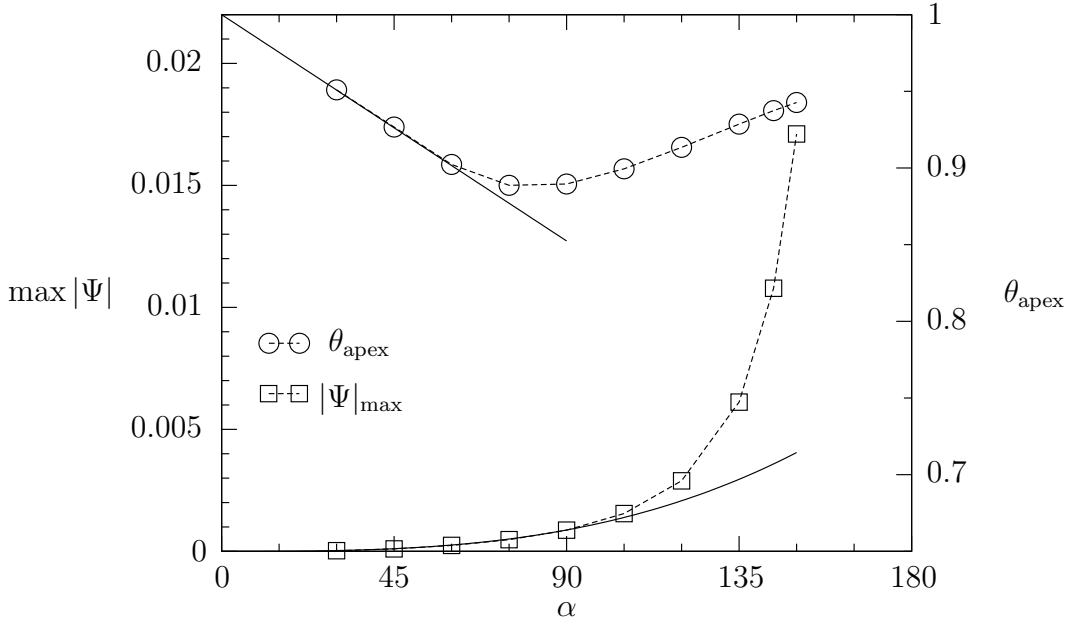


Figure 4.7: Stream function extremum $|\Psi|_{\max}$ (left axis, squares) and the temperature at the apex of the droplet θ_{apex} (right axis, circles) versus the contact angle α . Parameters as in figure 4.6. The dashed lines are guides to the eye. The full lines represent the approximations $\max |\Psi| = 1.2 \times 10^{-9} \alpha^3$ and $\theta_{\text{apex}} = 1 - 1.64 \times 10^{-3} \alpha$.

and the isotherms are straight and almost parallel. Comparing the temperature field for large and shallow droplets shows that the temperature distribution in droplets of small contact angles is much more uniform than the ones of large contact angles which confirms a much weaker thermocapillary convection in shallow droplets.

The effect of the contact angle variation on the fluid flow and the temperature field is compared in more detail in figure 4.7, which illustrates the temperature at the droplet's apex, θ_{apex} , as well as the stream function extremum, $|\Psi|_{\max}$, as functions of the contact angle α . In the asymptotic limit of shallow droplets ($\alpha \rightarrow 0$), the maximum thickness of the droplet is proportional to the contact angle $l \sim \alpha$. Considering the effective temperature difference, $\theta_{\text{eff}} = 1 - \theta_{\text{apex}}$, for the thermocapillary-driven flow, an order-of-magnitude consideration of heat transfer boundary condition of (3.31a) yields

$$\frac{1}{l}(1 - \theta_{\text{apex}}) \sim \text{Bi} \theta_{\text{apex}}. \quad (4.1)$$

Therefore, assuming $\theta_{\text{apex}} = 1 - \epsilon$ where ϵ is a small value, the effective driving temperature scales as

$$\frac{\epsilon}{1 - \epsilon} \approx \epsilon = \text{Bi} l \Rightarrow 1 - \theta_{\text{apex}} \sim \alpha. \quad (4.2)$$

Furthermore, a balance between viscous stresses and thermocapillary forces from the thermocapillary stress condition (3.31a) yields the following scaling for the stream function

$$\partial_\eta \theta \sim \Omega \approx \partial_{\xi\xi} \Psi \Rightarrow |\Psi|_{\max} \sim \overbrace{l^2}^{\sim \alpha^2} \underbrace{(1 - \theta_{\text{apex}})}_{\sim \alpha} \Rightarrow |\Psi|_{\max} \sim \alpha^3. \quad (4.3)$$

The scalings given in (4.2) and (4.3) are both confirmed with the computational results which are shown in figure 4.7. For the presented case, the following approximations fit well to the plotted curves

$$\max |\Psi| = 1.2 \times 10^{-9} \alpha^3, \quad (4.4a)$$

$$1 - \theta_{\text{apex}} = 1.64 \times 10^{-3} \alpha. \quad (4.4b)$$

By increasing the contact angle, neither the stream function nor the apex temperature follow the approximated trends indicated in (4.4). The stronger increment of the stream function leads to an amplified convective heat transport from the hot substrate along the liquid-gas interface toward the apex. Correspondingly, the apex temperature increases as it is presented in figure 4.7. The strengthened convection for large contact angles which is discussed above is supported by the geometry as for thermocapillary liquid bridges considered by Kuhlmann et al. (1999) and also Nienhüser and Kuhlmann (2002). In case of a hot substrate, the highest thermocapillary stresses along the free surface occur close to the contact line. For contact angles $\alpha > \pi/2$ the driving force along the free surface accelerates the flow and consequently enhances the convective heat transport, whereas for $\alpha < \pi/2$ it deflects and decelerates the flow close to the contact line.

The most influential parameter to be considered is the Biot number. Considering the current setup in which the heat transfer through the liquid-gas interface leads to a temperature deviation along the free surface and consequently enables the thermocapillary driving force, the rate of heat transfer which is characterized by the Biot number is of great importance. Figure 4.8 presents streamlines and isotherms varying the Biot number. Since for $\text{Bi} = 0$ we have an adiabatic liquid-gas interface, the temperature in the whole computational domain is uniform and no driving force exists. Therefore, there is no fluid flow in the domain and consequently no streamlines and isotherms are available for $\text{Bi} = 0$. For a very small Biot number as in figure 4.8a, a very weak temperature difference appears along the free surface which leads to a thermocapillary-driven

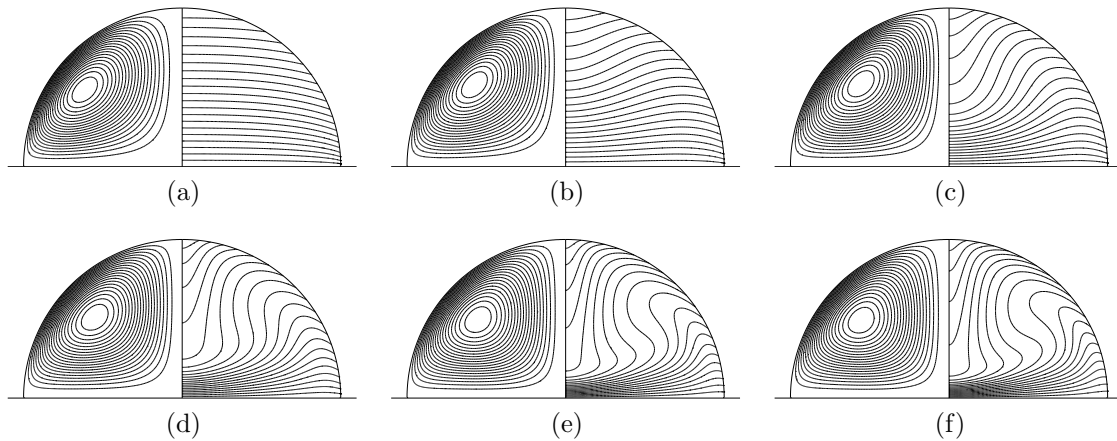


Figure 4.8: Biot number variation; (a) $Bi = 0.005$, (b) $Bi = 0.05$, (c) $Bi = 0.2$, (d) $Bi = 1$, (e) $Bi = 5$, and (f) $Bi = 20$. The parameters are $Re = 250$, $Pr = 4$, $Gr = 0$, $\theta_w = 1$, and $\alpha = \pi/2$.

Bi	$ \Psi _{\max} \times 10^4$	Ω_{core}	θ_{apex}	Center of vortex
0.005	0.337	-0.0021	0.9935	(0.613, 0.482)
0.05	3.857	-0.0244	0.9339	(0.574, 0.523)
0.2	10.88	-0.0655	0.8093	(0.556, 0.519)
1	25.01	-0.1431	0.5417	(0.549, 0.508)
5	45.21	-0.2477	0.2016	(0.555, 0.490)
20	53.56	-0.2938	0.0478	(0.554, 0.490)

Table 4.3: Stream function extremum, vorticity at the vortex core, apex temperature, and coordinate of the center of the vortex in Cartesian coordinates (x, y) for different Biot numbers. The parameters are the same as in figure 4.8.

force driving the flow toward the apex. By increasing the Biot number, this driving force enhances and the thermocapillary-driven vortex becomes stronger. The stronger toroidal vortex magnifies the internal convective heat transport within the domain as shown in figures 4.8d to 4.8f.

Table 4.3 lists some characteristics of the flow for the cases given in figure 4.8. Comparing the temperature at the droplet's apex as well as the stream function extremum shows a strong influence of the Biot number on the flow field. For instance, the stream function extremum grows more than two orders of magnitude and the temperature at the apex decays almost to zero when the Biot number varies from $Bi = 0.005$ to $Bi = 20$. However, comparing the rate of change of the stream function and the position of the center of vortex for large Biot numbers shows that these parameters converge to

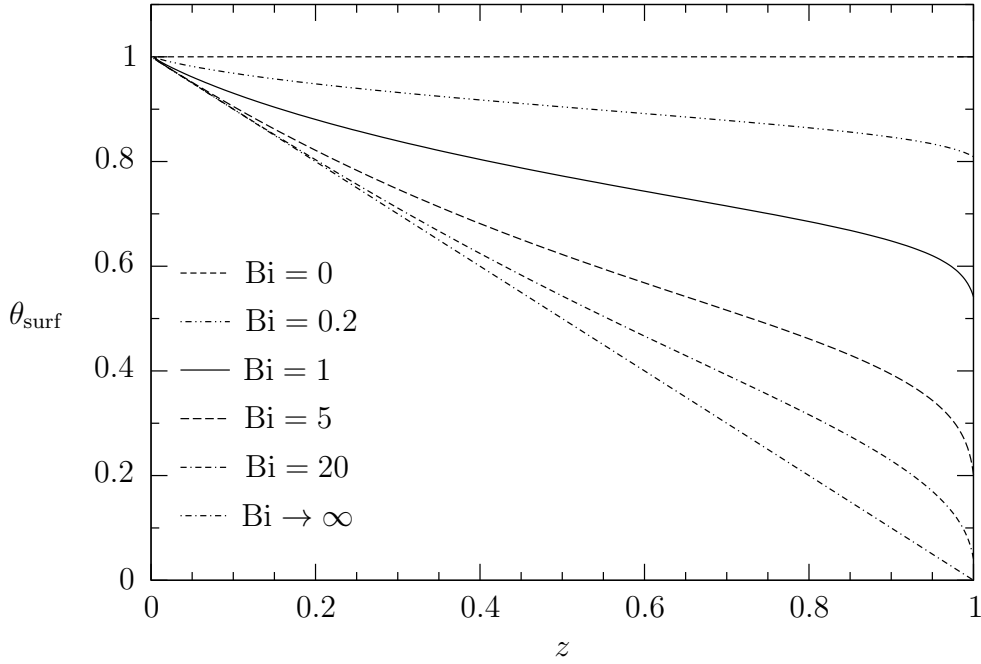


Figure 4.9: Temperature distribution along the liquid-gas interface θ_{surf} as function of the distance z from the plate for different Bi numbers. The parameters are the same as in figure 4.8.

a limit. In other words, by further increasing the Biot number, the flow behavior will not considerably change.

To further analyze the effect of Biot number on the fluid flow, the temperature distribution along the liquid-gas interface is illustrated in figure 4.9 for different Biot numbers including both the limiting cases of $\text{Bi} = 0$ and $\text{Bi} \rightarrow \infty$. As discussed above, for $\text{Bi} = 0$ the temperature is constant in the domain and along the free surface ($\theta_{\text{surf}} = \theta_w = 1$). On the contrary, when the Biot number tends to infinity, the temperature along the liquid-gas interface is imposed by the passive ambient gas, in which the temperature distribution is linear with respect to the height z . Therefore, in case of $\text{Bi} \rightarrow \infty$ the temperature distribution along the free surface is also linear. The temperature profiles for other relatively large Biot numbers which are plotted in figure 4.9 (e.g. $\text{Bi} = 5, 20$) show a convergence to the asymptotic case of $\text{Bi} \rightarrow \infty$.

Finally, figure 4.10 presents the temperature of the droplet's apex as a function of the contact angle α for wide range of Biot numbers covering four orders of magnitude $\text{Bi} = 0.1, 1, 10, \text{ and } 100$. For the adiabatic liquid-gas interface, $\text{Bi} = 0$, the apex temperature is equal to the equilibrium temperature of the bulk $\theta_{\text{apex}} = 1$. The curve for $\text{Bi} = 0.1$ and its asymptotic scaling for the limit of small contact angles have been

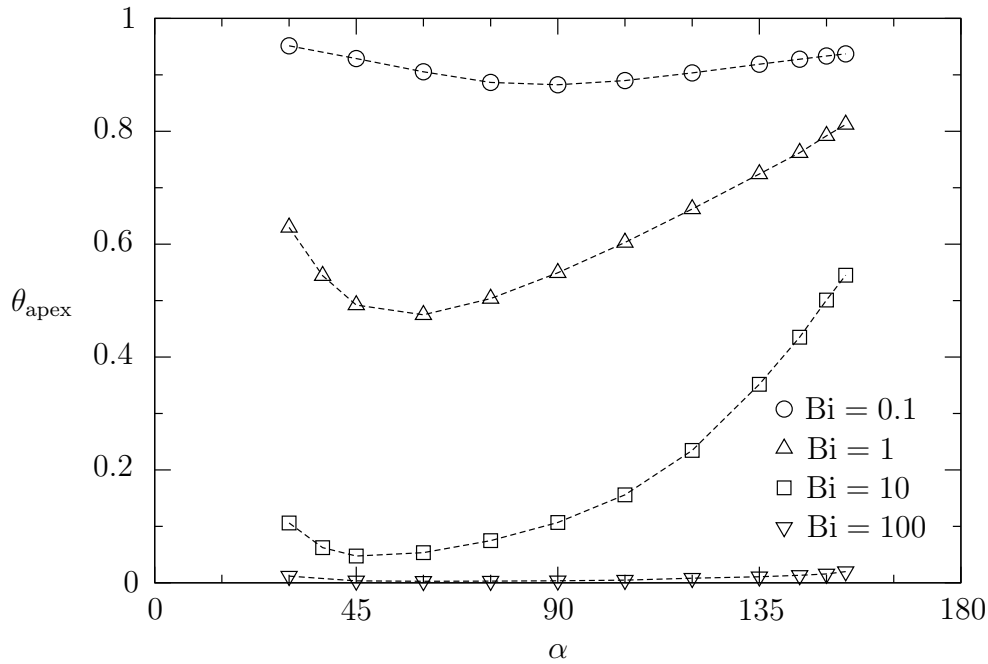


Figure 4.10: Drop's apex temperature, θ_{apex} , as a function of the contact angle, α , for different Biot numbers. The parameters are $Re = 250$, $Pr = 4$, $Gr = 0$, and $\theta_w = 1$.

discussed in figure 4.7. By increasing the Biot number, the rate of heat exchange along the liquid-gas interface increases and consequently, the temperature of the apex decreases. Considering the cases $Bi = 1$ and $Bi = 10$, by decreasing the contact angle it can be seen that the temperature increases, which is similar to the case of $Bi = 0.1$ but with different slopes depending on the Biot number. By further increasing the Biot number ($Bi = 100$), the apex temperature converges to the asymptotic case of $Bi \rightarrow \infty$. Therefore, the apex temperature tends to zero independent of the contact angle. For all cases presented, the apex temperature increases by increasing the contact angle (only beyond the minimum of each curve) due to an enhanced convective heat transport along the free surface as discussed earlier in this subsection.

4.1.2 Buoyancy-driven flow

In the previous subsection, the effect of pure thermocapillary driving force (zero gravity case, $Gr = 0$) on the flow in liquid droplets was discussed. Another important driving force to be considered is the buoyancy in the presence of gravity, where $Gr \neq 0$. In

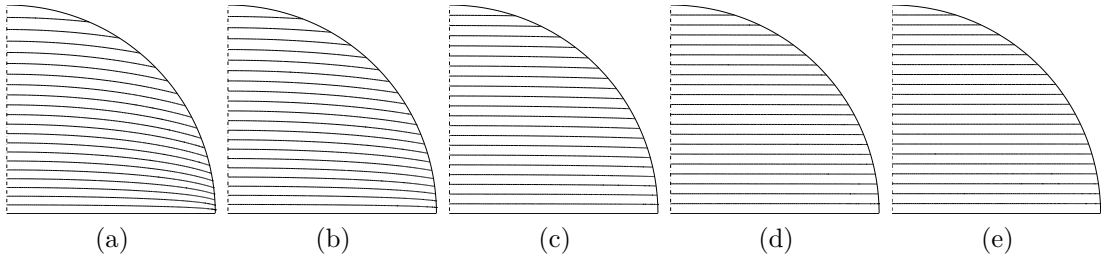


Figure 4.11: Isotherms in the absence of thermocapillarity and gravity. The parameters are $\text{Pr} = 28$, $\text{Gr} = 0$, $\theta_w = 1$, $\alpha = \pi/2$, and (a) $\text{Bi} = 0.1$, (b) $\text{Bi} = 1$, (c) $\text{Bi} = 10$, (d) $\text{Bi} = 100$, (e) $\text{Bi} = 10^5$.

this case, the last term on the right side of (3.24b)

$$-\frac{\text{Gr}}{\text{Re}} \left[(\cosh \eta \cos \xi - 1) \partial_\eta + (\sinh \eta \sin \xi) \partial_\xi \right] \theta \quad (4.5)$$

is non-zero. Since $\text{Gr}/\text{Re} \sim R^2$, this term vanishes again for small droplets when $R \rightarrow 0$. In other words, the thermocapillary force dominates buoyancy for the droplets of small radius. However, for a range of low Reynolds and relatively high Grashof numbers buoyancy affects the flow. For such cases, these two driving forces form different flow structures within the droplet which will be discussed later. Nevertheless, the investigation of the effect of pure buoyant driving force on the fluid flow in droplets is essential prior to study the combined buoyant-thermocapillary flow.

In order to treat the pure buoyant flow, instead of the thermocapillary scaling which is used in the case of thermocapillary-driven flow, the viscous scaling of the governing equations is employed as presented in (3.33). Furthermore, the thermocapillary boundary conditions along the liquid-gas interface (3.26a) have to be replaced by a free-slip boundary condition which is given in (3.37).

In the absence of buoyancy and thermocapillary stresses, the Biot number is the only parameter determining the temperature field. Figure 4.11 shows the isotherms for different Biot numbers in a droplet with the contact angle of 90° . For small Biot numbers, the isotherms are horizontal close to the centerline but slightly bent toward the contact line. By increasing the Biot number, the isotherms become horizontal and nearly parallel within the whole domain. In the limit of $\text{Bi} \rightarrow \infty$ the free surface temperature equals the ambient temperature and the isotherms are fully parallel.

As discussed above, for a high Biot number, e.g. $\text{Bi} = 100$, the flow is at the state of rest with nearly parallel horizontal isotherms (see figure 4.11d). This thermal stratification

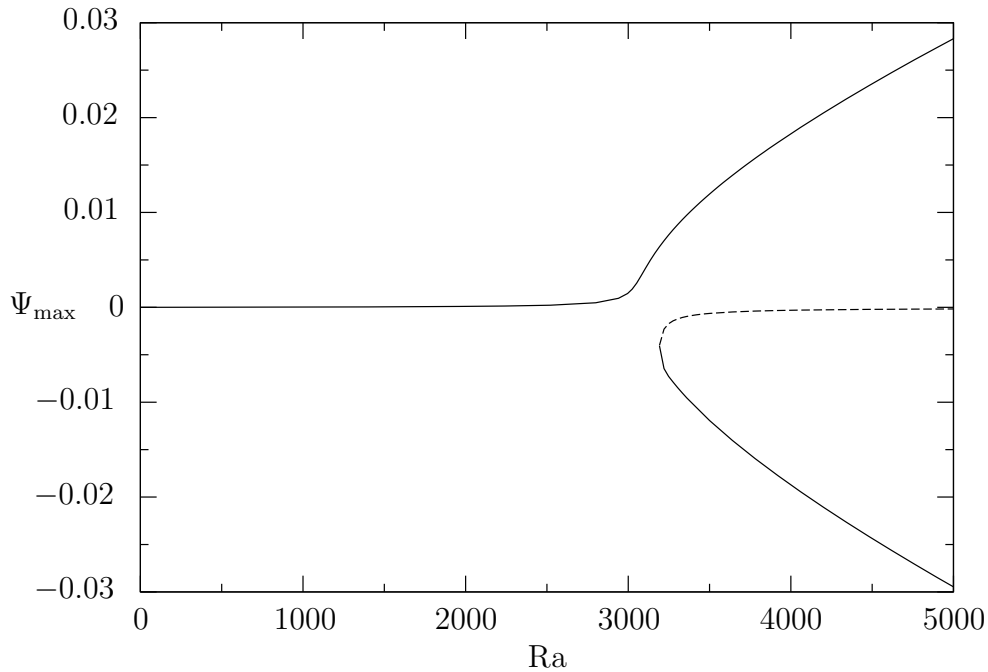


Figure 4.12: Extremum of Ψ as a function of the Rayleigh number for $\text{Pr} = 28$, $\alpha = \pi/2$, $\text{Bi} = 100$, and $\theta_w = 1$.

within a droplet sitting on a heated substrate can be unstable for a certain Rayleigh number, $\text{Ra} = \text{GrPr}$, when the thermal expansion coefficient is positive $\beta > 0$. In order to find the neutral Rayleigh number Ra_n at which convection sets in, we start from the basic state with $\text{Ra} = 0$ and increase the Rayleigh number gradually by increasing the level of gravity Gr . Figure 4.12 shows the evolution of the stream function extremum of the steady state as a function of the Rayleigh number. For a wide range of Rayleigh numbers the stream function remains nearly zero. However, due to a weak horizontal temperature gradient for a finite value of Biot number, a weak flow is detected for any non-zero value of Rayleigh number. For $\text{Ra} \approx 3080 \pm 50$, the value of the stream function starts growing with a relatively steep slope which shows that the fluid flow is developing. This flow has a toroidal structure (see figure 4.13d) with an upward flow direction along the centerline.

For $\text{Ra} > 3200$, more than one branch of numerical solutions exist as shown in figure 4.12. One set of solutions corresponds to a toroidal vortex with a reverse flow direction contrary to the one discussed before, and the other branch of the solutions exhibits a weak flow which tends to zero by increasing the Rayleigh number. This plot with three solution branches for $\text{Ra} > 3200$ exhibits a pitchfork bifurcation diagram which is weakly perturbed due to an imperfect vertical temperature gradient. The upper and lower solid branches which are almost symmetrical with respect to the horizontal axis

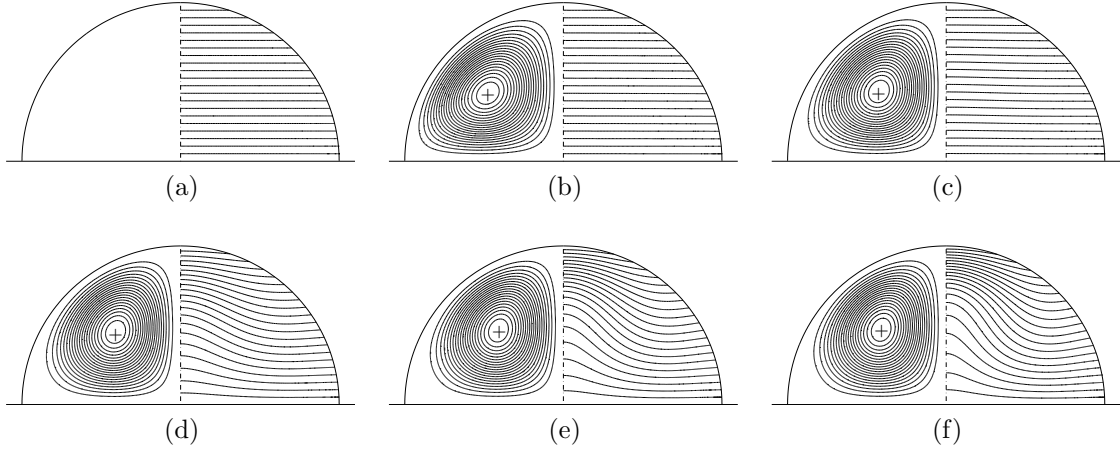


Figure 4.13: Streamlines and the temperature field for pure buoyant flow corresponding to the upper solid branch in figure 4.12. ”+” sign indicates the upward flow direction along the centerline. The parameters are $Pr = 28$, $\alpha = \pi/2$, $\theta_w = 1$, $Bi = 100$, and (a) $Ra = 0$, (b) $Ra = 1400$, (c) $Ra = 2800$, (d) $Ra = 3360$, (e) $Ra = 3920$, (f) $Ra = 4480$.

($\Psi = 0$) present the stable solutions, while the center dashed line branch indicates the unstable solution.

Figures 4.13 to 4.15 show the streamlines and the temperature field for the solutions at the upper, center, and lower branches, respectively. For zero gravity case ($Ra = 0$), no flow is detected since no driving force acts on the fluid (figure 4.13a). By increasing the Rayleigh number up to $Ra \approx 3000$, a very weak flow is detected due to the imperfect temperature distribution as it was explained before. Comparing the streamlines corresponding to the upper (figures 4.13d to 4.13f) and the lower stable branches (figures 4.15a to 4.15c) show that the vortex structures are very similar for any Rayleigh number, but the flow direction is reversed. The respective temperature fields illustrate different directions of the convection within the domain in these two cases.

The symmetric bifurcation diagram can be obtained considering $Bi \rightarrow \infty$ for which the isotherms are exactly parallel. However, because of the numerical errors, a perfectly symmetric diagram cannot be obtained. Moreover, it is not possible to apply $Bi \rightarrow \infty$ in the computations. Therefore, we impose a fixed linear temperature distribution along the liquid-gas interface employing the same function as in the passive ambient temperature. This is numerically equivalent to set $Bi \rightarrow \infty$. With this setup, it is possible to obtain the pitchfork bifurcation as it is illustrated in figure 4.16. Similar to the diagram obtained for $Bi = 100$ in figure 4.12, two stable (solid lines) and one

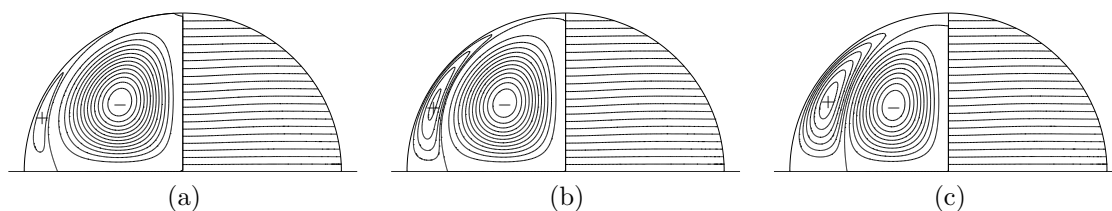


Figure 4.14: Streamlines and the temperature field for pure buoyant flow corresponding to the dashed line in figure 4.12. The minus/plus sign (\mp) indicates the clockwise/counter-clockwise rotation. The parameters are $Pr = 28$, $\alpha = \pi/2$, $\theta_w = 1$, $Bi = 100$, and (a) $Ra = 3360$, (b) $Ra = 3920$, (c) $Ra = 4480$.

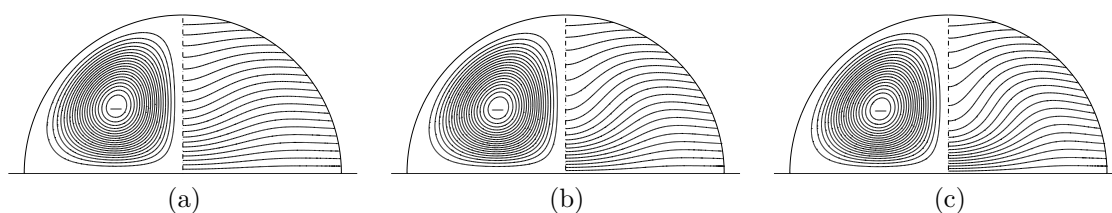


Figure 4.15: Streamlines and the temperature field for pure buoyant flow corresponding to the lower solid branch in figure 4.12. "-" sign indicates the downward flow direction along the centerline. The parameters are $Pr = 28$, $\alpha = \pi/2$, $\theta_w = 1$, $Bi = 100$, and (a) $Ra = 3360$, (b) $Ra = 3920$, (c) $Ra = 4480$.

unstable (dashed line) branches are detected when the Rayleigh number exceeds a certain value. For the case of nearly perfect pitchfork bifurcation, this value is called the neutral Rayleigh number which is found to be $Ra_c \approx 3100 \pm 10$.

It is important to know how the flow behaves between the two limits $Bi = 0$ and $Bi \rightarrow \infty$. Figure 4.17 shows the previously discussed cases of $Bi = 100$ and $Bi \rightarrow \infty$ in comparison to three other Biot numbers ($Bi = 0.1, 1$, and 10), to illustrate different trends for different Biot numbers. It should be mentioned that only the positive half of the vertical axis is shown to make it easier to compare the curves. For $Bi = 0.1$, the curve has a shallow slope which results in a very weak flow even for very high Rayleigh numbers. The reason for that is a relatively strong horizontal temperature gradient within the domain for such a low Biot number. Increasing the Biot number to $Bi = 1$ leads to a slightly weaker flow in subcritical regime, i.e. $Ra < 3000$, and a stronger flow for higher Rayleigh numbers $Ra > 3000$ for which the slope of the curve increases by increasing the Rayleigh number. By further increasing the Biot number, a turning point appears somewhere in the interval of $Ra \in [2800, 3200]$, and the curves tend to converge to the asymptotic case of $Bi \rightarrow \infty$. This turning point exists also for low

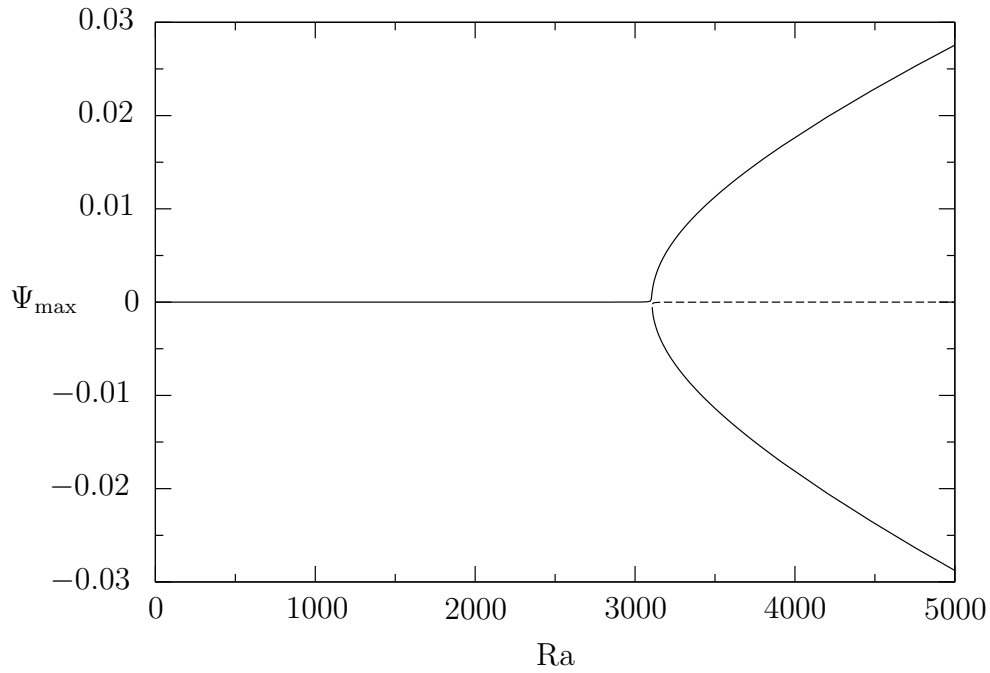


Figure 4.16: Extremum of Ψ as a function of the Rayleigh number for $\text{Pr} = 28$, $\alpha = \pi/2$, $\theta_w = 1$, and $\text{Bi} \rightarrow \infty$.

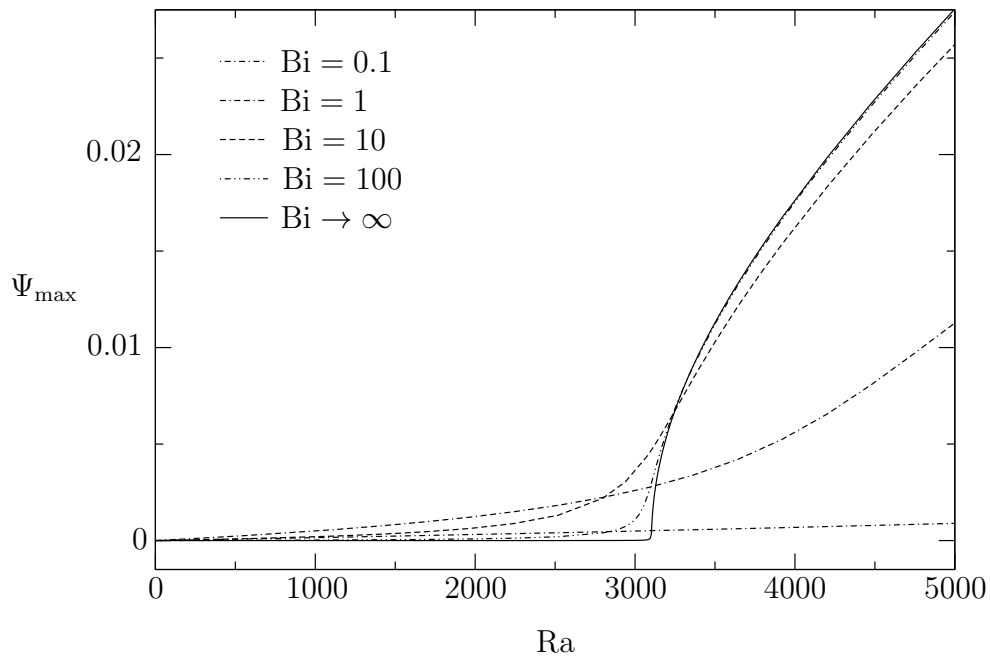


Figure 4.17: Maximum of Ψ as a function of the Rayleigh number for $\text{Pr} = 28$, $\alpha = \pi/2$, $\theta_w = 1$, and $\text{Bi} = 0.1, 1, 10$, and 100 as well as $\text{Bi} \rightarrow \infty$.

Prandtl numbers, but at much higher Rayleigh numbers.

4.1.3 Thermocapillary-buoyant flow

To study the evolution of combined thermocapillary-buoyant flow in liquid droplets, a wide range of Reynolds, Prandtl, and Grashof numbers have to be considered. As shown in figure 4.18, different flow patterns are obtained for various liquid materials with $Pr = 0.02$ (left column), $Pr = 4$ (middle column), and $Pr = 83$ (right column). The general strategy to obtain the flow field is to start with a pure thermocapillary case in which $Gr = 0$. In this case, only a single toroidal vortex appears (downward flow along the axis $\eta = 0$) for all liquid materials. However, the temperature field is different for different Prandtl numbers. By increasing the gravity level, different flow structures are realized depending on the temperature distribution in the domain. In order to show various combination of the counter-rotating vortices, many different cases have been considered varying Reynolds, Prandtl, Biot, and Grashof numbers. Figure 4.18 presents only three selected setups in which the flow evolves differently by increasing the gravity level.

In the case of a low Prandtl number $Pr = 0.02$, the structure of the temperature field initiates an upward buoyant flow along the drop's centerline (opposite to the thermocapillary effect on the free surface) by increasing the gravity level. Consequently, the buoyant driving force generates a counter-rotating toroidal vortex near the centerline which is illustrated in figure 4.18d (counter-clockwise rotation, '+'). By further increasing the Grashof number, the buoyancy-driven vortex grows in size and starts to occupy the whole domain, squeezing the counter-rotating thermocapillary-driven vortex toward the liquid-gas interface (figures 4.18g, 4.18j, and 4.18m). Finally, for the current case with $Re = 25$ and $Bi = 0.5$, the buoyancy-driven vortex completely dominates the flow for $Gr > 3000$.

For $Pr = 4$ the temperature field is slightly different (see figure 4.18b). Considering a constant vertical distance, z , from the substrate, the maximum temperature is found to be somewhere between the contact line and the center of the droplet. Therefore, for a strong enough gravity level as in figure 4.18h, the buoyancy-driven vortex which is attached to the substrate appears at the described position close to the contact line. By increasing the Grashof number, this vortex grows in size and intensity and again squeezes the thermocapillary-driven vortex, but this time toward the centerline (figures 4.18k and 4.18n). In this case, although thermocapillarity drives the flow along free surface from the contact line toward the apex, the flow is opposing the thermocapillary

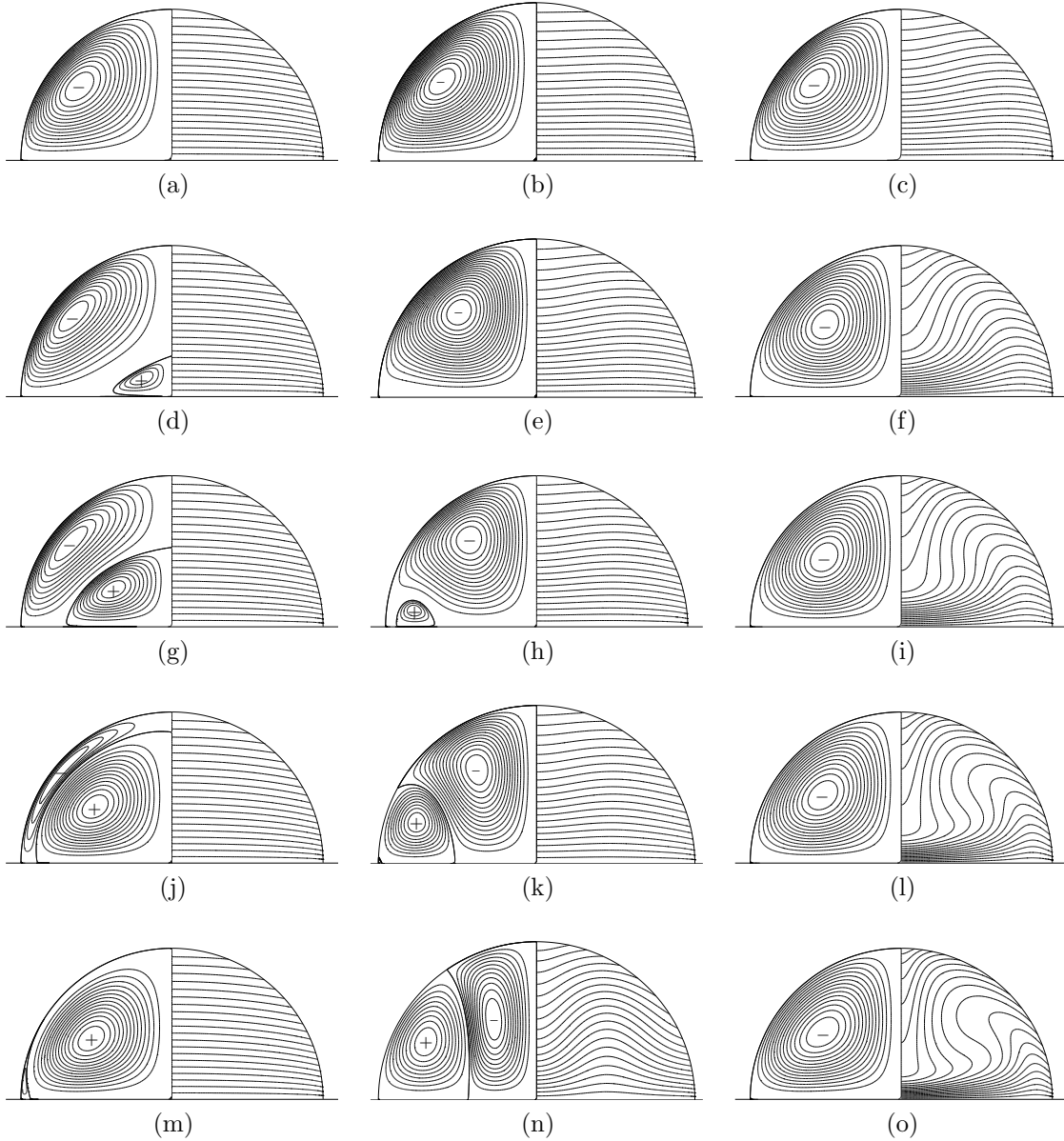


Figure 4.18: Combined thermocapillary-buoyant flow for $Bi = 0.5$, $\alpha = \pi/2$, and $\theta_w = 1$. Left column: $Pr = 0.02$ and $Re = 25$ for $Gr = 100, 1300, 1600, 2400$, and 3000 . Middle column: $Pr = 4$ and $Re = 10$ for $Gr = 100, 1000, 1400, 2000$, and 4000 . Right column: $Pr = 83$ and $Re = 1$ for $Gr = 10, 100, 200, 500$, and 1000 .

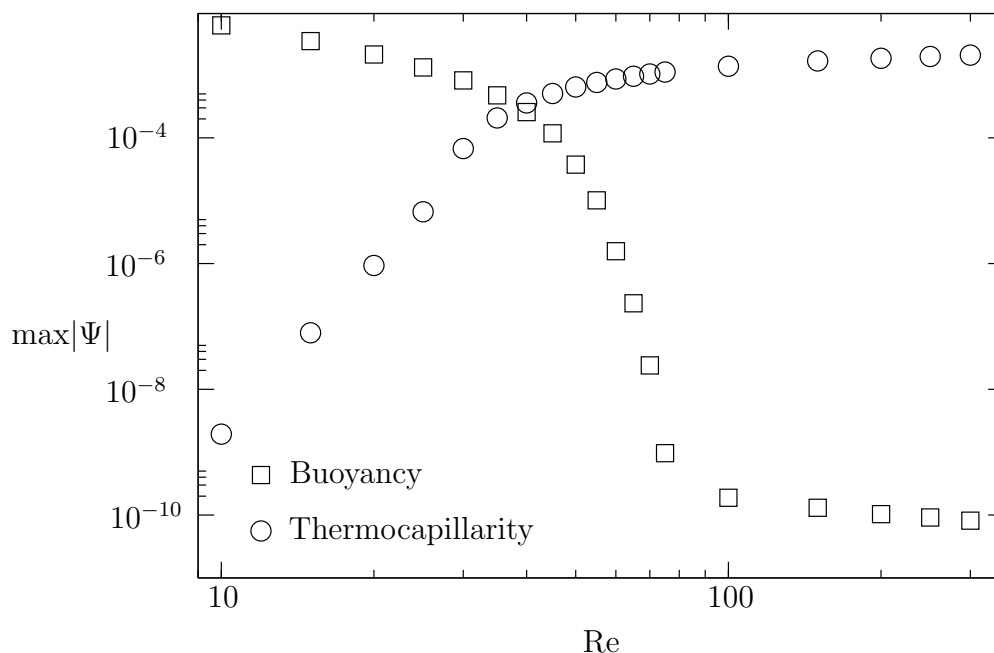


Figure 4.19: Stream function extrema $|\Psi|_{\max}$ for the buoyancy-driven vortex ($\Psi_{\max} > 0$) as well as thermocapillary-driven vortex ($\Psi_{\min} < 0$) as functions of the Reynolds number. The parameters are $\text{Pr} = 0.02$, $\text{Bi} = 0.5$, $\text{Gr} = 3000$, $\alpha = \pi/2$, and $\theta_w = 1$.

forces in the region where buoyancy is dominant. Therefore, along the free surface two different flow directions exist which leads to an upward flow from an intermediate radial distance from the droplet's center. The resulting convective heat transport can be seen considering the isolines sketched in figure 4.18n.

Finally, the flow evolution subject to the combined thermocapillary-buoyant flow is considered for $\text{Pr} = 83$ (figure 4.18, right column). In this case, the maximum temperature at a constant distance from the substrate is detected very close to the contact line. Consequently, the buoyant force drives the flow upward along the free surface and, unlike the previous cases in which the two driving forces compete, it amplifies the thermocapillary-driven vortex which has the same flow direction. By increasing the Grashof number, the convective heat transport becomes stronger (see figures 4.18l and 4.18o), since the Rayleigh number is very large.

The competition between thermocapillarity and buoyancy can be also discussed by fixing the gravity level and varying the thermocapillary Reynolds number. In order to present this competition, a variation of the Reynolds number in the interval of $\text{Re} \in [10, 300]$ for the case of $\text{Pr} = 0.02$ and $\text{Gr} = 3000$ has been selected. In figure 4.19 the absolute values of the stream function extrema for the two counter-rotating

Gr	Ma = 28		Ma = 280		Ma = 2800	
	θ_{apex}	$ \Psi _{\text{max}} \times 10^3$	θ_{apex}	$ \Psi _{\text{max}} \times 10^3$	θ_{apex}	$ \Psi _{\text{max}} \times 10^3$
10	0.4451	3.325	0.4302	3.251	0.6214	1.738
80	0.4454	3.390	0.4209	2.888	0.6198	1.714
120	0.4458	3.623	0.4067	2.223	0.6154	1.649
240	0.4461	3.959	0.4043	1.744	0.6081	1.549
360	0.4462	4.244	0.4024	1.510	0.5998	1.446

Table 4.4: Temperature at the apex of the droplet, θ_{apex} , and the stream function extremum, $\max |\Psi|$, for the cases shown in figure 4.20.

vortices are plotted as functions of Reynolds number on logarithmic scales. Buoyancy dominates thermocapillarity for $\text{Re} < 40$. An example of this regime has been already discussed for $\text{Re} = 25$ in figure 4.18m. However, for $\text{Re} > 40$ the thermocapillary-driven force becomes dominant and the buoyancy-driven vortex vanishes with a steep slope.

In contrast to the cases discussed above for a sessile droplet sitting on a heated plate, the competition between the thermocapillary and buoyant forces does not lead to development of a counter-rotating vortex in a hanging droplet attached to a heated substrate. Figure 4.20 depicts the flow and temperature fields in droplets subject to different combination of thermocapillary and buoyant forces. In each column, the Marangoni number is constant (left column: $\text{Ma} = 28$, middle column: $\text{Ma} = 280$, and right column: $\text{Ma} = 2800$) and the level of gravity (Grashof number) increases from top to bottom. Comparing the streamlines and isotherms of each column, it is clear that the thermocapillarity dictates the flow direction even for higher gravity levels. In the middle column, by increasing the Grashof number, the buoyant forces exhibit a weak stabilizing effect by driving the flow in a reverse direction of the thermocapillary forces. This weak influence can be observed comparing the isotherms in figure 4.20b with the ones which are flattened in figure 4.20n. In left and right columns, it is difficult to visually distinguish the effect of buoyancy for different Grashof numbers. Therefore, some quantitative data are listed in table 4.4 for all droplets presented in figure 4.20, in order to facilitate the comparison. For $\text{Ma} = 2800$, by increasing the gravity level the stream function extremum decreases. This means that, similar to the middle column, buoyancy forces oppose the flow motion. In contrast, for $\text{Ma} = 28$, the values of stream function extremum for different Grashof numbers confirm that the buoyant forces enhance the thermocapillary-driven vortex. In other words, buoyancy drives the flow in the same direction of the thermocapillary stresses.

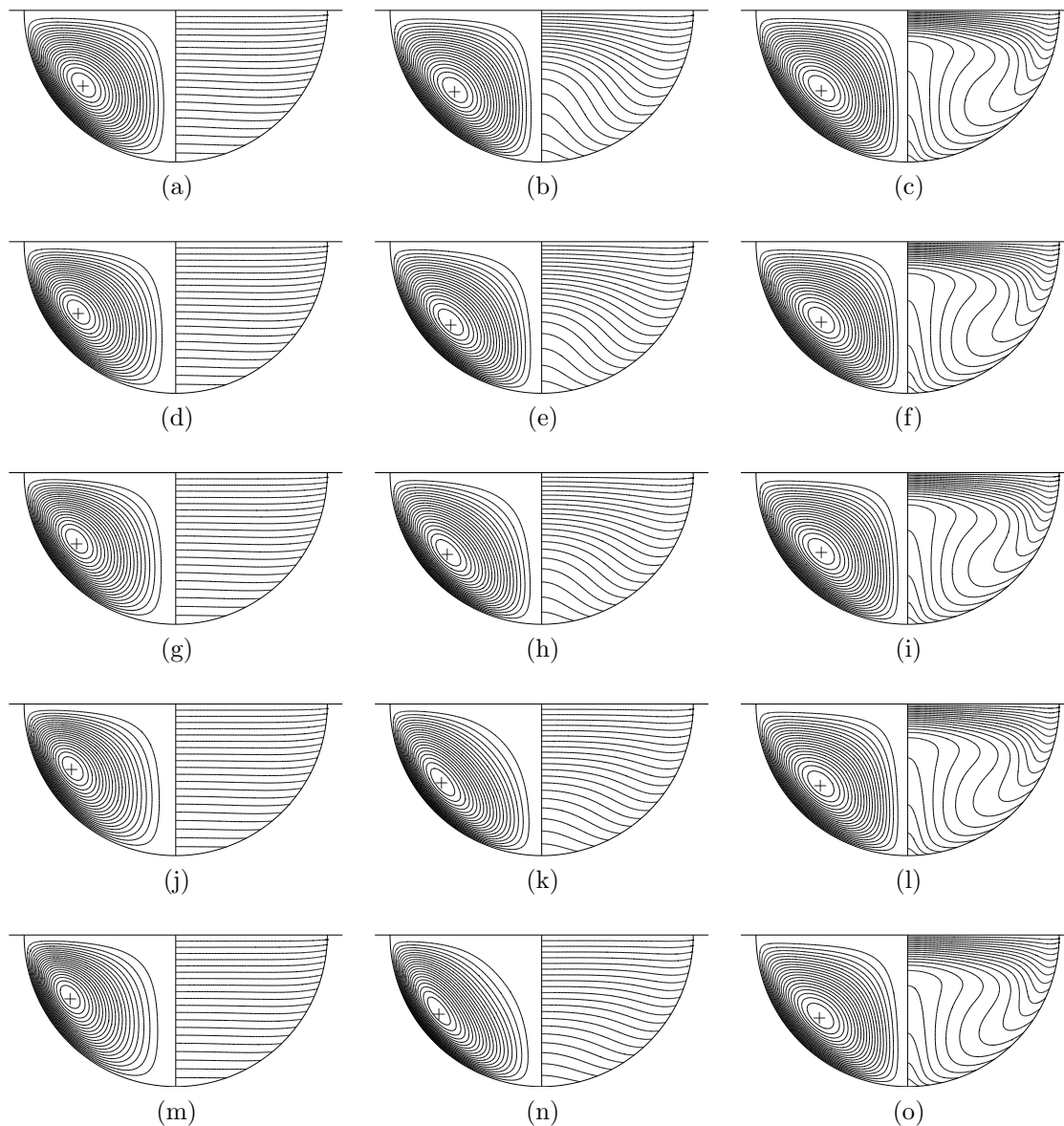


Figure 4.20: Combined thermocapillary-buoyant flow in a hanging droplet attached to a heated plate; $Ma = 28$ (left column), $Ma = 280$ (middle column), and $Ma = 2800$ (left column). The parameters are $Bi = 1$, $\alpha = 90^\circ$, and (a,b,c) $Gr = 10$, (d,e,f) $Gr = 80$, (g,h,i) $Gr = 120$, (j,k,l) $Gr = 240$, (m,n,o) $Gr = 360$.

4.2 Cooled substrate

For a droplet attached to a cooled plate in an ambient in which the dimensionless temperature varies linearly between the substrate $\theta_a(0) = 0$ and a distance l away from the substrate $\theta_a(l) = 1$, a temperature gradient arises within the liquid depending on the rate of heat transfer through the liquid-gas interface. Similar to the case of the heated plate in cooled ambient, this temperature gradient leads to a thermocapillary- or buoyant-driven flow, or a combination of these two flows, depending on the problem setup. In this section, a parametric study is presented for a droplet attached to a cooled plate varying Reynolds, Prandtl, Grashof, and Biot numbers as well as the contact angle.

4.2.1 Thermocapillary-driven flow

The temperature gradient along the liquid-gas interface results in thermocapillary stresses along the free surface which drives the flow toward the contact line (cold end of the free surface with $\theta = 0$). Therefore, unlike the case of heated plate, the flow direction is upward along the centerline. The structure of the flow for different Prandtl numbers is illustrated in figure 4.21, for $Re = 1, 10, 100, 250$, and 1000 . The flow and temperature fields are visually similar for all Prandtl numbers when $Re = 1$, as the thermocapillary driving force is weak. By increasing the Reynolds number, the flow evolves differently for each presented Prandtl number.

For $Pr = 0.02$ (left column), the Marangoni number is small (varies between 2 and 20); therefore, the temperature field remains nearly unchanged as Reynolds number increases. In case of higher Marangoni numbers (middle and right columns), the thermocapillarity is stronger which leads to the convective heat transport along the liquid-gas interface toward the contact line. As a result, a large temperature gradient forms close to the cold substrate which generates the only driving force within the domain since along the rest of the interface the temperature becomes almost constant (see e.g. 4.21o). The concentration of the temperature gradient and consequently strong thermocapillary stresses close to the contact line lead to displacement of the center of the vortex toward the contact line. Correspondingly, the streamlines are compressed in this region which confirms that the thermocapillarity drives the flow mainly in this part of the liquid-gas interface.

The apex temperature as well as the stream function extremum for the given cases in

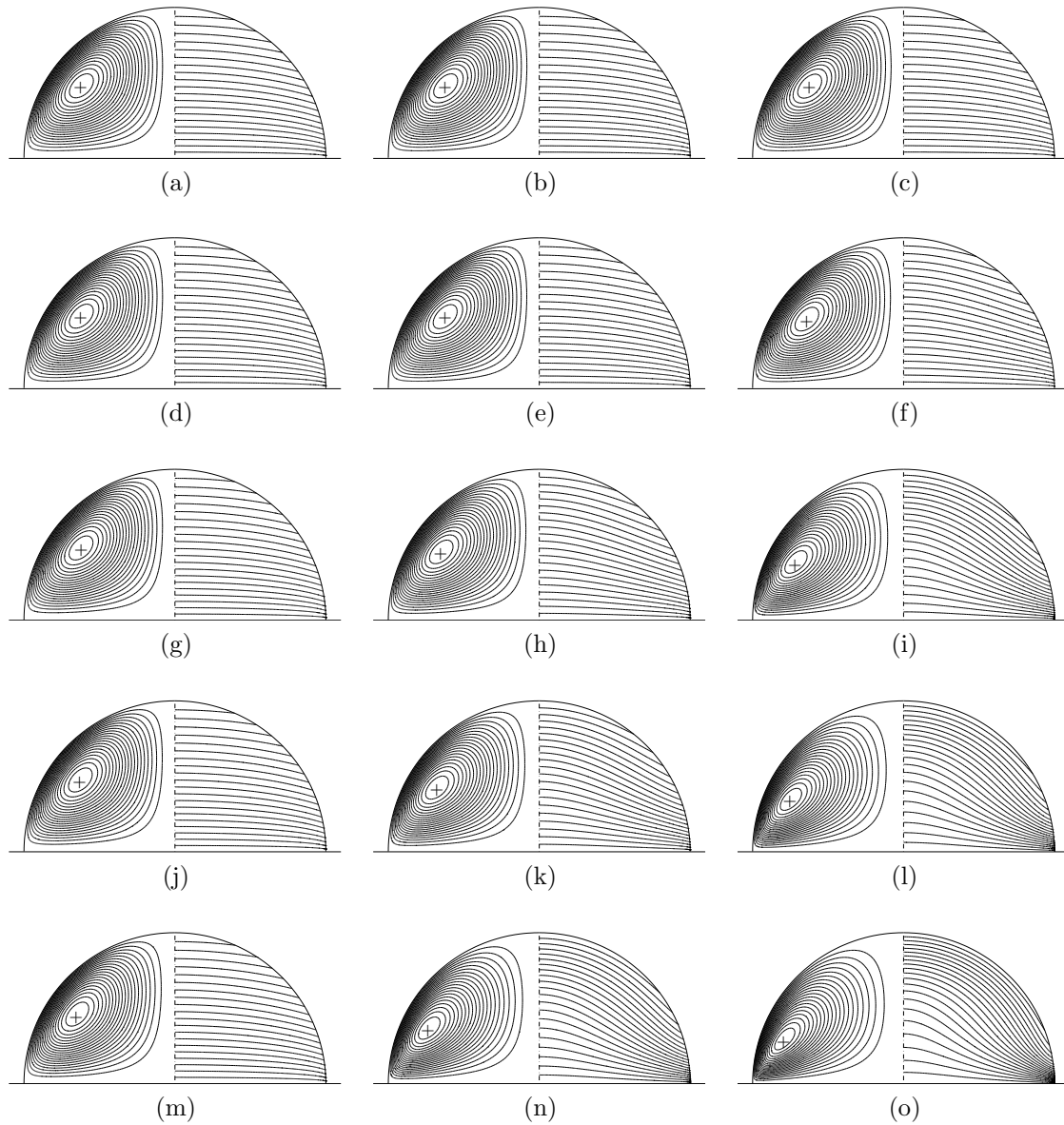


Figure 4.21: Reynolds number variation for $Pr = 0.02$ (left column), $Pr = 4$ (middle column), and $Pr = 28$ (right column), for $Gr = 0$, $\theta_w = 0$, and $Bi = 0.1$. (a,b,c) $Re = 1$, (d,e,f) $Re = 10$, (g,h,i) $Re = 100$, (j,k,l) $Re = 250$, (m,n,o) $Re = 1000$.

Re	Pr = 0.02		Pr = 4		Pr = 28	
	θ_{apex}	$ \Psi _{\text{max}} \times 10^4$	θ_{apex}	$ \Psi _{\text{max}} \times 10^4$	θ_{apex}	$ \Psi _{\text{max}} \times 10^4$
1	0.1128	5.775	0.1127	5.761	0.1119	5.671
10	0.1128	5.770	0.1115	5.623	0.1046	4.844
100	0.1127	5.721	0.1018	4.512	0.0795	2.182
250	0.1126	5.641	0.0923	3.449	0.0689	1.298
1000	0.1123	5.306	0.0755	1.796	0.0553	0.523

Table 4.5: Apex temperature and max $|\Psi|$ for the cases shown in figure 4.21.

figure 4.21 are listed in table 4.5. By increasing the Prandtl number for a constant Reynolds number, the stream function extremum decays and the apex temperature decreases. In the current case of a cooled plate, the effective temperature difference for thermocapillary driving is $\theta_{\text{eff}} = \theta_{\text{apex}}$ (rather than $1 - \theta_{\text{apex}}$ for the heated plate case). Therefore, the larger θ_{apex} for $\text{Pr} = 0.02$ means that the driving force is stronger in this case. This can be confirmed by comparing the stream function extremum for $\text{Pr} = 0.02$ and 28 which shows an order of magnitude difference for $\text{Re} = 1000$. Furthermore, increasing the Reynolds number results in a reduction of the temperature of the droplet's apex for all Prandtl numbers. However, this reduction is stronger when the Prandtl number is large due to the reduced thermal diffusivity.

The vortex structure for different Prandtl numbers is compared in figure 4.22 considering the same parameters as in figure 4.3. These curves are the stream function values which are plotted as functions of ξ along an $\eta = \text{constant}$ line which is shown in figure 4.22b. For a constant Marangoni number, $\text{Ma} = 2800$, all the curves cluster on top of one another for $\text{Pr} > 1$ having a peak of $|\Psi|_{\text{max}} \approx 2.2 \times 10^{-4}$, whereas the low Prandtl number case exhibits a separate curve with a lower peak at $|\Psi|_{\text{max}} \approx 1.5 \times 10^{-4}$. In order to compare the cases plotted in figure 4.22 quantitatively, table 4.6 lists some characteristic parameters for the discussed cases above. Apart from the first row which corresponds to the low Prandtl number $\text{Pr} = 0.02$, all the other quantities are quite similar for $\text{Pr} > 1$.

The maximum of the stream function as a function of a wide range of Marangoni numbers is plotted in figure 4.23 for four different liquids, $\text{Pr} = 0.02, 4, 28,$ and 83 . In contrast to the heated plate case (see figure 4.5) in which all the curves exhibit a maximum before decaying, a monotonically decreasing trend has been observed for all the considered cases of a droplet attached to a cooled plate. In the limit of large Marangoni numbers ($\text{Ma} > 10^3$), two different asymptotic trends are found for low and

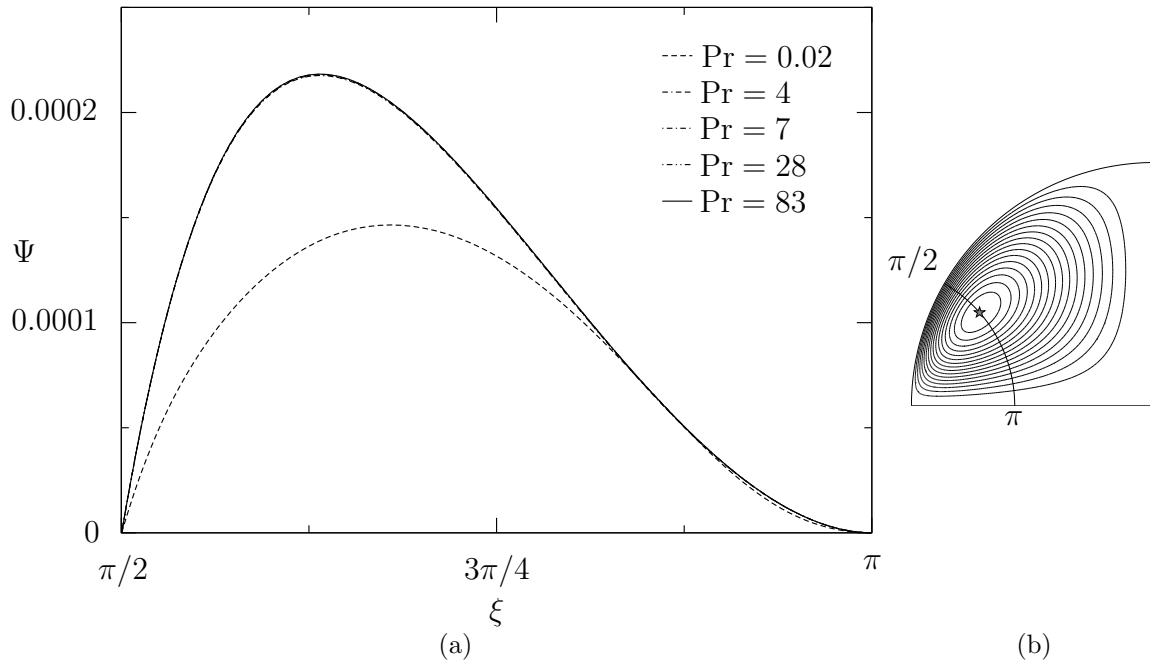


Figure 4.22: (a) Stream function Ψ versus ξ along an $\eta = \text{constant}$ line which passes through the stream function maximum Ψ_{max} ; see (b). The parameters are $Ma = RePr = 2800$, $Bi = 0.1$, $Gr = 0$, $\theta_w = 0$, and $\alpha = \pi/2$.

Pr	$ \Psi _{\text{max}} \times 10^4$	Ω_{core}	θ_{apex}	Center of vortex
0.02	1.465	0.0131	0.1033	(0.781, 0.256)
4	2.176	0.0153	0.0798	(0.720, 0.383)
7	2.179	0.0153	0.0796	(0.720, 0.383)
28	2.182	0.0153	0.0795	(0.720, 0.383)
83	2.183	0.0153	0.0794	(0.720, 0.383)

Table 4.6: Stream function extremum, vorticity at the vortex core, apex temperature, and coordinate of the center of the vortex in Cartesian coordinates (x, y) for different Prandtl numbers. The parameters are the same as in figure 4.22.

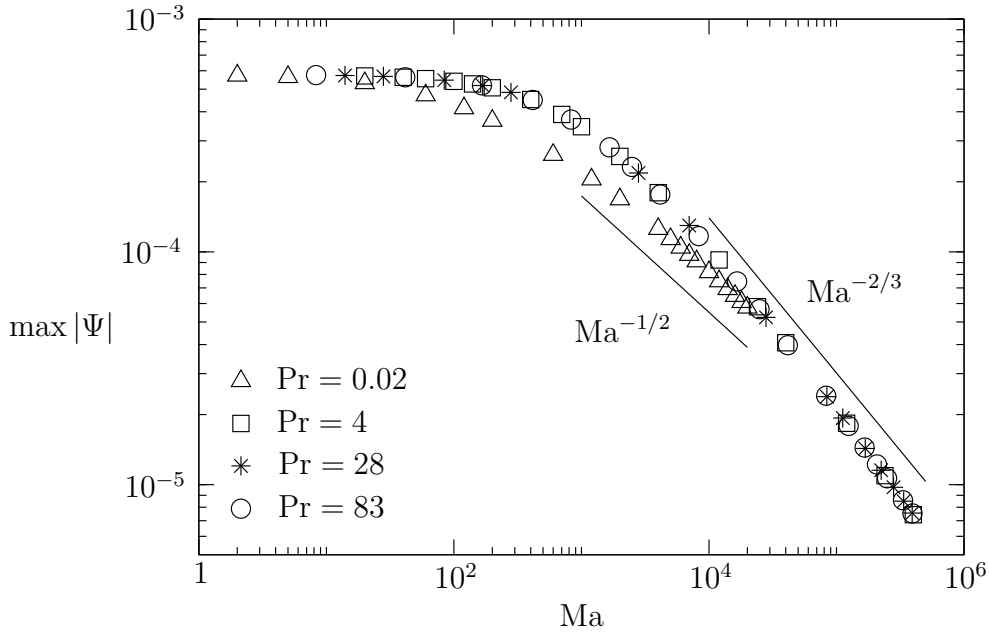


Figure 4.23: Maximum of $|\Psi|$ as a function of Ma . The parameters are $Bi = 0.1$, $Gr = 0$, $\theta_w = 0$, and $\alpha = \pi/2$.

high Prandtl numbers: $\max |\Psi| \sim Ma^{-1/2}$ for low Prandtl numbers which is similar to the slope given in figure 4.5, and $\max |\Psi| \sim Ma^{-2/3}$ for all higher Prandtl numbers which show a much stronger decay rate in comparison to the case of a heated plate.

The difference between the asymptotic slopes for high Prandtl numbers ($-1/3$ and $-2/3$ for heated and cooled plate, respectively) can be described comparing the temperature along the free surface of the heated and cooled plate cases for the same Marangoni number as presented in figure 4.24. In order to have the same scaling for the vertical axis of the graph, the effective surface temperature, $\theta_{\text{surf}}^{\text{eff}}$, is defined as

$$\theta_{\text{surf}}^{\text{eff}} = \begin{cases} 1 - \theta_{\text{surf}} & \text{(heated plate),} \\ \theta_{\text{surf}} & \text{(cooled plate).} \end{cases} \quad (4.6)$$

A continuous increase of effective surface temperature is detected for the heated plate case which means that along the whole free surface, the thermocapillarity drives the flow. In contrast, the effective surface temperature for the cooled plate exhibits a step increase close to the contact line ($z \rightarrow 0$); then for $z > 0.4$ becomes nearly flat which means that no temperature gradient is available for this part of the liquid-gas interface. The reduced length of active thermocapillarity over the free surface is found to be the reason for the reduction of the net driving force. As a result, the decay of

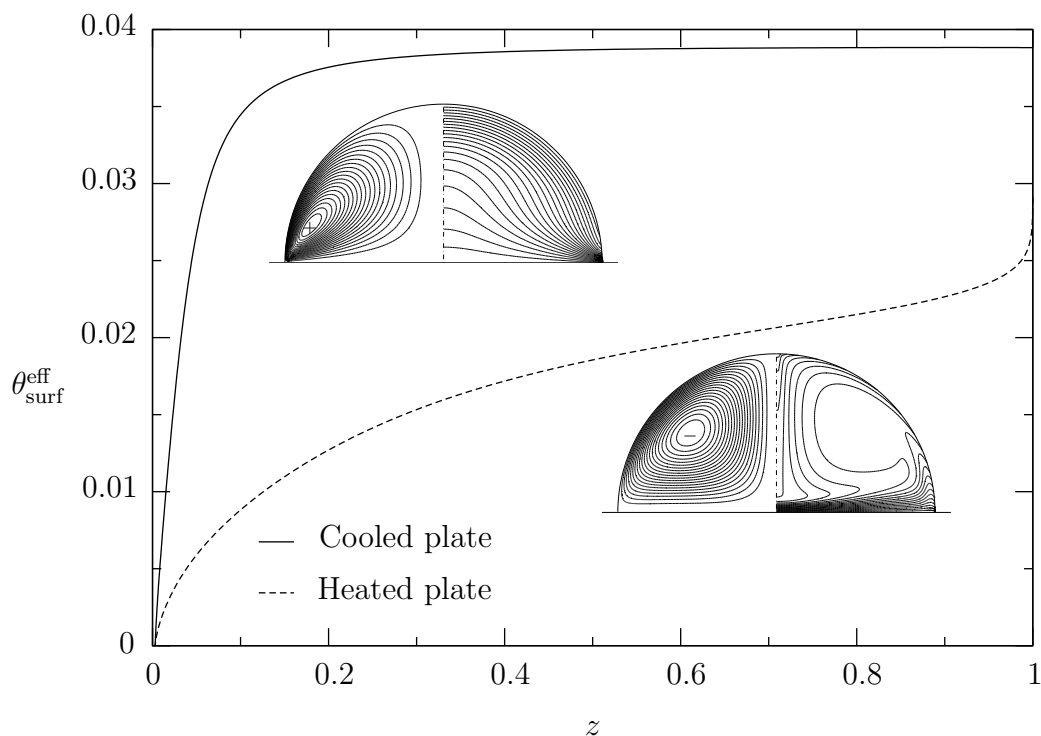


Figure 4.24: Effective surface temperature $\theta_{\text{surf}}^{\text{eff}}$ as a function of the distance z from the substrate. $\theta_{\text{surf}}^{\text{eff}} = \theta_{\text{surf}}$ for the case of cooled plate and $\theta_{\text{surf}}^{\text{eff}} = 1 - \theta_{\text{surf}}$ for heated plate. The parameters are $\text{Bi} = 0.1$, $\alpha = \pi/2$, $\theta_w = 0$, and $\text{Ma} = 2.8 \times 10^5$.

$\max |\Psi| \sim \text{Ma}^{-2/3}$ for the cooled plate case is confirmed to be steeper than the one for a heated plate, $\max |\Psi| \sim \text{Ma}^{-1/3}$.

In order to analyze the influence of the Biot number on the fluid flow, the presented case in figure 4.21h has been chosen with the parameters $\text{Re} = 100$, $\text{Pr} = 4$, and $\text{Bi} = 0.1$. The results for a wide range of Biot numbers are presented in figure 4.25 and more quantitative data are listed in table 4.7. Although the streamlines and isotherms are visually very similar, especially for $\text{Bi} > 10$ (see figures 4.25d, 4.25e, and 4.25f), comparing the parameters given in the table illustrates a strong variation of θ_{apex} and consequently, stream function and vorticity when the Biot number increases. The temperature difference between the apex of the droplet and the cooled plate varies from $\Delta\theta \approx 0.1$ for $\text{Bi} = 0.1$ to $\Delta\theta \approx 1$ in the limiting case of $\text{Bi} = 10^4$ which can be assumed to well approximate $\text{Bi} \rightarrow \infty$. As a result, the toroidal vortex becomes considerably stronger ($|\Psi|_{\text{max}}$ is more than an order of magnitude larger). Comparing the last two rows in table 4.7 verifies that all the given parameters are converging to an asymptotic limit when the Biot number tends to infinity.

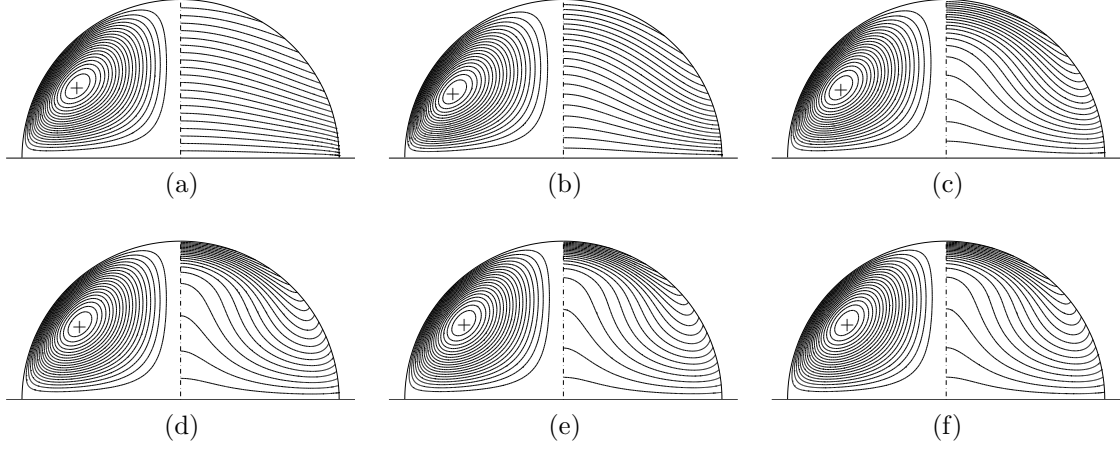


Figure 4.25: Biot number variation. The parameters are $Re = 100$, $Pr = 4$, $Gr = 0$, $\theta_w = 0$, $\alpha = \pi/2$, and (a) $Bi = 0.1$, (b) $Bi = 1$, (c) $Bi = 10$, (d) $Bi = 10^2$, (e) $Bi = 10^3$, (f) $Bi = 10^4$.

Bi	$ \Psi _{\max} \times 10^4$	Ω_{core}	θ_{apex}	Center of vortex
0.1	4.513	0.0286	0.1018	(0.654, 0.449)
1	16.488	0.1123	0.4108	(0.696, 0.415)
10	39.217	0.2572	0.7397	(0.665, 0.441)
10^2	56.728	0.3725	0.9421	(0.637, 0.474)
10^3	60.360	0.3941	0.9930	(0.625, 0.483)
10^4	60.783	0.3967	0.9991	(0.625, 0.483)

Table 4.7: Stream function extremum, vorticity at the vortex core, apex temperature, and coordinate of the center of the vortex in Cartesian coordinates (x, y) for different Biot numbers. The parameters are the same as in figure 4.25.

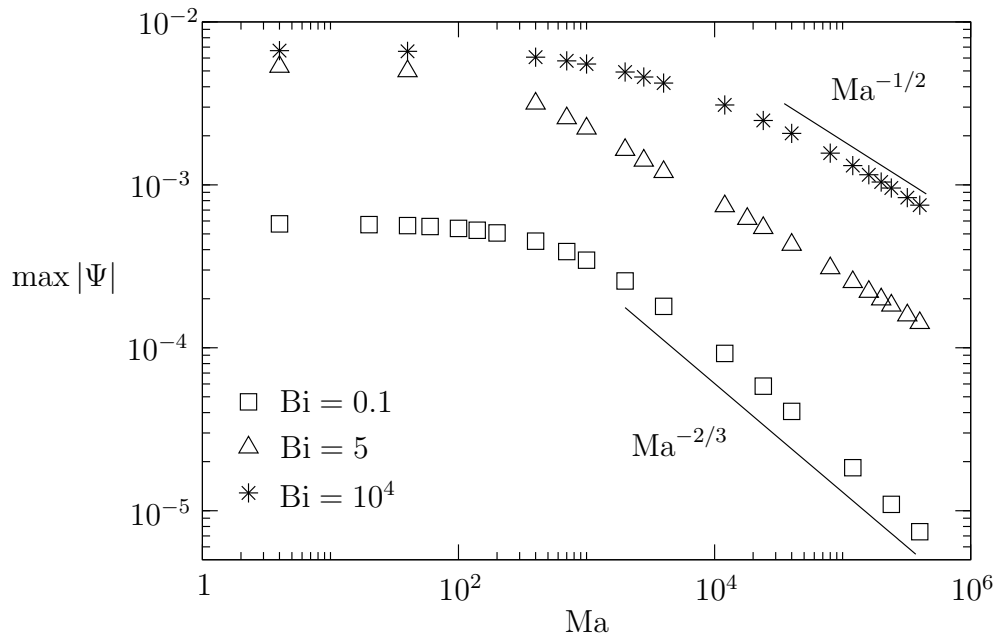


Figure 4.26: Maximum of stream function, $\max |\Psi|$, as a function of Marangoni number, Ma , for $Pr = 4$, $Gr = 0$, $\theta_w = 0$, $\alpha = \pi/2$ and different Biot numbers.

The influence of the Biot number on the asymptotic behavior of the flow is taken into account in figure 4.26, in which the stream function extremum is plotted as a function of Marangoni number for three Biot numbers, $Bi = 0.1, 5$, and 10^4 . As it is discussed before, for low Biot numbers, the temperature along a large part of the free surface becomes constant for high Marangoni numbers which leads to a steep decay of the stream function maximum when Marangoni number increases. However, by increasing the Biot number, the temperature at each point along the liquid-gas interface tends to the temperature of the ambient gas at the same vertical distance from the substrate. Therefore, the temperature is not constant along the free surface anymore and consequently, the thermocapillarity drives the flow along the whole free surface. As a result, for large Biot numbers the asymptotic behavior of the flow changes and scales with $\max |\Psi| \sim Ma^{-1/2}$ which is the same as the obtained scaling for the low Prandtl number case shown in figure 4.5.

4.2.2 Buoyancy-driven flow

For a droplet which is sitting on a cooled substrate the thermal stratification normal to the substrate is buoyantly stable when $\beta > 0$. In contrary, a droplet pending from a cooled plate in a heated ambient can be unstable. Therefore, the more attractive

case of a hanging droplet is chosen. The instability in a hanging droplet with the contact angle of 90° results in a similar pitchfork bifurcation as in the case of a sessile droplet on a heated plate (see figure 4.16). The equivalence is due to the symmetry of the linearized equations with respect to $\text{Gr} \rightarrow -\text{Gr}$ and $\Delta T \rightarrow -\Delta T$ in the absence of thermocapillary stresses. For this reason, instead of considering only the hanging droplet with the contact angle of 90° , the effect of contact angle variation on the fluid flow in hanging droplets subject to pure buoyant driving force is discussed.

Studying the fluid flow in a shallow hanging droplet subject to the pure buoyant forces is more interesting than considering droplets with large contact angles, as multiple convection cells develop by increasing the level of gravity. Therefore, we start with investigating the evolution of the flow in a shallow hanging droplet with the contact angle of $\alpha = 22.5^\circ$ in the absence of capillary instabilities in the limit $\text{Ca} \rightarrow 0$. For such a shallow droplet where the aspect ratio is relatively small, $l = L/R \approx 0.197$, it makes sense to scale the Grashof number with l instead of R . For the new scaling, we have

$$\text{Gr} = \frac{g\beta\Delta T l^3}{\nu^2}. \quad (4.7)$$

The scaling of the equations has been modified accordingly by substituting R with l . Similar to the heated plate, a high Biot number $\text{Bi} = 100$ has been chosen in order to obtain a linear temperature distribution within the domain with horizontal and almost parallel isotherms. Streamlines and isotherms for different Rayleigh numbers are plotted in figure 4.27. For a low level of gravity, e.g. $\text{Ra} = 280$, an extremely weak toroidal vortex develops, but the temperature field is hardly perturbed. Ideally, no flow should be detected for such a low Rayleigh number in case of a fully parallel isotherms. However, for the finite Biot numbers a weak flow develops for any non-zero Rayleigh number. By gradually increasing the Rayleigh number, a cat's eye structure evolves at the center of the toroidal vortex. For $\text{Ra} = 1580$ a separated counter-rotating vortex develops attached to the substrate which breaks the cat's eye structure and divides the single toroidal vortex into two vortices (figure 4.27c). This counter-rotating vortex grows in size and magnitude by a very small increment of the Rayleigh number and forms a convection cell between the two existing vortices (figure 4.27d).

Up to a certain Rayleigh number the temperature field remains nearly unperturbed (see figures 4.27a to 4.27d), whereas for higher Rayleigh numbers, the convective heat transport can be observed in the temperature field. Therefore, a good approximation of the neutral Rayleigh number for $\alpha = 22.5^\circ$ is found to be $\text{Ra}_n = 1750 \pm 100$ after comparing the temperature field for a wide range of Rayleigh numbers. In chapter 5, the exact value of the neutral Rayleigh number Ra_n for a wide range of contact angles

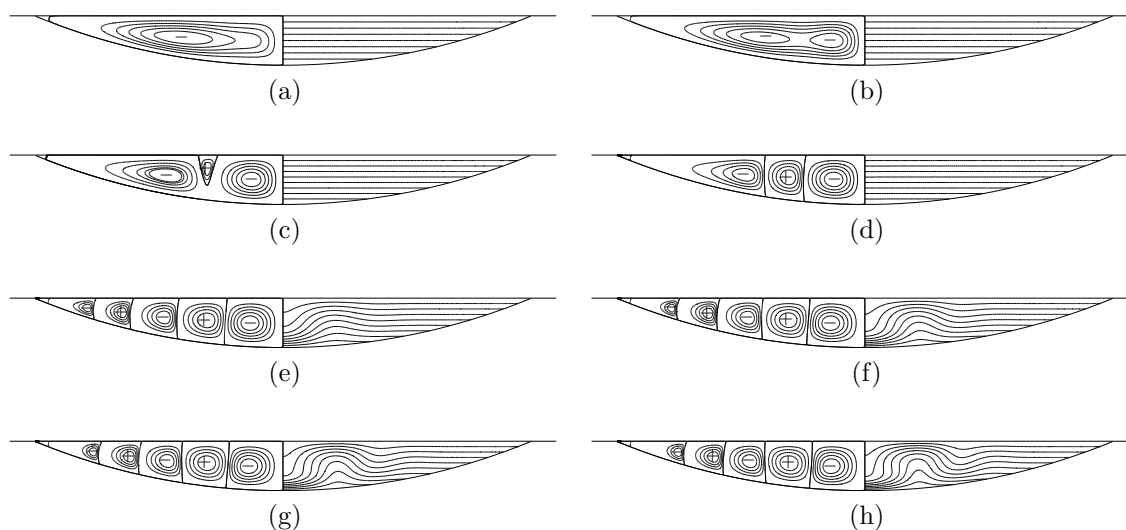


Figure 4.27: Pure buoyant flow in shallow drops hanging from a cooled substrate; Rayleigh number variation: (a) $Ra = 280$, (b) $Ra = 980$, (c) $Ra = 1580$, (d) $Ra = 1680$, (e) $Ra = 2240$, (f) $Ra = 2800$, (g) $Ra = 3360$, and (h) $Ra = 3920$. The parameters are $Pr = 28$, $\theta_w = 0$, $\alpha = 22.5^\circ$, and $Bi = 100$.

will be obtained by means of axisymmetric linear stability analysis. For $Ra > Ra_n$ thermal instabilities result in a chain of convection cells. This onset of instability is comparable, in order of magnitude, with the threshold of the linear stability for a planar fluid layer with one free and one rigid boundary, $Ra_c = 1100.65$ (Chandrasekhar, 1961) as the droplet is shallow. However, it should be noted that the observed convection cells in a droplet are toroidal (axisymmetric), whereas in a plane layer they are straight cylindrical rolls.

The number of convection cells in the droplet increases by further increasing the Rayleigh number on account of possibly two main reasons. On the one hand, the stronger vortices close to the centerline of the droplet drive weaker viscous eddies in the tapered region (Moffatt, 1964). On the other hand, the flow becomes locally unstable in the vicinity of the contact line for a much higher Rayleigh number than the one close to the centerline. In other words, introducing the local Rayleigh number

$$Ra_{\text{local}} = Ra \left(\frac{h(r)}{l} \right)^3, \quad (4.8)$$

which is scaled with the local height of the droplet at each radial distance from the centerline, $h(r)$, it is possible that Ra_{local} becomes larger than the neutral Rayleigh number in some regions of the domain.

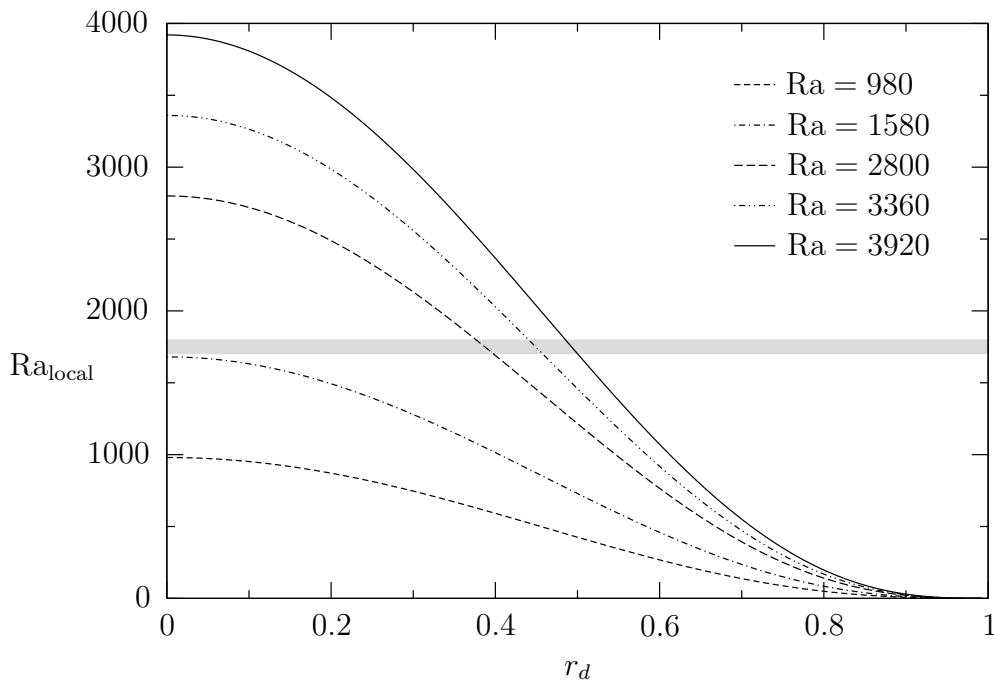


Figure 4.28: Local Rayleigh number Ra_{local} as a function of the dimensionless radial distance from the centerline $r_d = lr$ for $Pr = 28$, $\theta_w = 0$, and different Rayleigh numbers. The grey region is an approximation of the neutral Rayleigh number for the contact angle of $\alpha = 22.5^\circ$. The exact value of the neutral Rayleigh number will be given in chapter 5.

In order to examine the influence of the Rayleigh number on the evolution of the convective cells in the tapered region, figure 4.28 illustrates the local Rayleigh number as a function of the dimensionless radial distance from the centerline, $r_d = lr$, for different Rayleigh numbers. An estimate of the onset of instability is highlighted by the thick grey bar in the plot. The curves corresponding to the higher Rayleigh numbers ($Ra = 3360$ and 3920) indicate that the flow is locally stable for $r_d > 0.5$. However, for these cases the convection cells have already developed in this region (see figures 4.27g and 4.27h). As a result, the local instabilities cannot be considered as a reason for the evolution of these toroidal cells; therefore, the former reason (viscous eddies) gives a more convincing explanation of the flow behavior in the vicinity of the contact line. This can be confirmed even visually by comparing the structure of vortices in the convection cells, e.g. in figure 4.27h. In cells which are closer to the centerline, the center of each vortex lies almost on the center of its corresponding cell showing that a body force (buoyancy) drives the flow. On the contrary, the vortex center shifts to one side of the cell in the corner cells; consequently, the streamlines are compressed between the vortex center and the separating streamline, which shows that a surface force (viscosity) drives the vortex. Similar vortex structures have been observed in

other flows which are driven by viscous forces, mainly as a consequence of boundary confinements (Liron and Blake, 1981; Malyuga, 2005). Moffatt (1964) showed that the fluid flow close to a sharp corner when at least one of the boundaries is a rigid wall have to consist of a sequence of viscous eddies, in which the intensity and size decreases rapidly by approaching the corner. This argument holds for the current case of a shallow droplet attached to a flat substrate which exhibits a sharp corner with both rigid and free boundaries.

To analyze the structure of the flow in more details, the absolute values of the stream function along $\xi_{\text{mid}} = (\xi_{\text{max}} + \xi_{\text{min}})/2$ are plotted in figure 4.29 for different Rayleigh numbers. The algebraic mean of the ξ coordinate in the η - ξ plane is selected because it nearly passes through the stream function extremum of each convection cell. The logarithmic scale has been chosen for the vertical axis in order to make the visualization of the stream function extrema easier. It also facilitates the comparison of the flow structures for a wide range of Rayleigh numbers. It should be noted that the peak values shown in figure 4.29 do not represent the exact values associated with the stream function extremum in each cell because the described $\xi = \text{constant}$ line does not perfectly passes through the center of all vortices. However, they give a good estimate of the extremum values.

For $\text{Ra} = 980$ and 1580 the flow is thermally stable (see also the corresponding curves in figure 4.28) and as it is discussed before, the imperfect vertical temperature gradient leads to the observed weak flow. Two weak maxima are observed for $\text{Ra} = 980$ at $r_d \approx 0.1$ and 0.4 which correspond to the developed cat's eye structure (see figure 4.27b). However, the flow structure is different when Rayleigh number increases ($\text{Ra} = 1580$) and three maxima are detected. In this case, the convection cells, in which the flow direction reverses from one cell to the next one, have developed (see figure 4.27d). Since the absolute value of the stream function is plotted in figure 4.29, each local maximum represents a convection cell. For instance, for $\text{Ra} = 1580$, the second peak at $r_d \approx 0.3$ corresponds to the middle convection cell in figure 4.27d in which the flow direction is counter-clockwise ('+') and the other two peaks refer to the other two clockwise-rotating vortices ('-').

When the Rayleigh number exceeds the neutral Rayleigh number, $\text{Ra} > \text{Ra}_n$, the number of maxima increases to five for the current setup shown in figure 4.29. The local maxima for higher Rayleigh numbers present the intensity of each toroidal convection cell which grows by increasing the Rayleigh number. For these cases, it can be observed that only the first three cells which are closer to the centerline of the droplet are strong enough to visibly disturb the temperature field (see also figures 4.27f to 4.27h). The

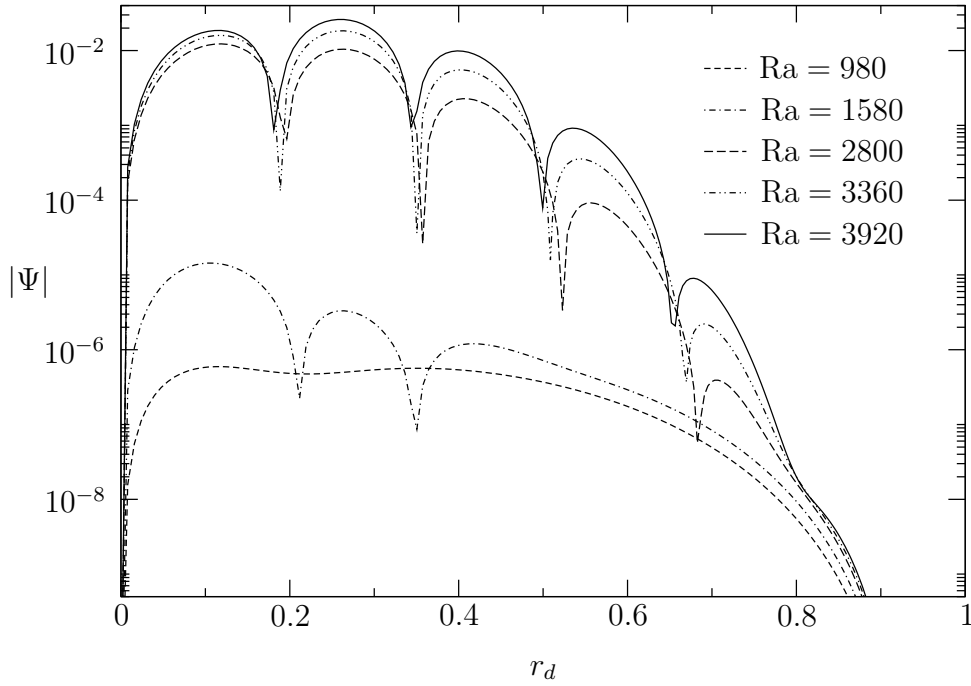


Figure 4.29: $|\Psi|$ along $\xi_{\text{mid}} = (\xi_{\text{max}} + \xi_{\text{min}})/2$ as a function of the dimensionless radial distance from the centerline r_d for $\text{Pr} = 28$, $\theta_w = 0$, $\alpha = 22.5^\circ$ and different Rayleigh numbers.

other toroidal vortices in the region of the subcritical local Rayleigh number ($r_d > 0.5$), have much weaker stream function extrema. Furthermore, in the vicinity of the contact line and for $r_d > 0.9$, the stream function tends to zero for all the cases independent of the Rayleigh number.

A shallow droplet with the contact angle of $\alpha = 22.5^\circ$ has been thoroughly investigated above. In order to study the influence of the contact angle on the fluid flow, droplets with different contact angles ($\alpha = 105^\circ, 60^\circ$, and 36°) are considered. Figure 4.30 illustrates the stream lines and isotherms for these droplets for $\text{Ra} = 3360$. The Rayleigh number is chosen to be large enough such that for all the presented cases, the flow becomes thermally unstable. Comparing the flow fields for the presented cases shows that the number of convection cells decreases by increasing the contact angle. To explain this, it is necessary to consider the shape of each convection cell. Introducing the aspect ratio for a convection cell

$$\Gamma_{\text{cell}} = \frac{h_{\text{cell}}}{w_{\text{cell}}}, \quad (4.9)$$

where h_{cell} and w_{cell} are the mean height and the mean width of a cell, respectively, it

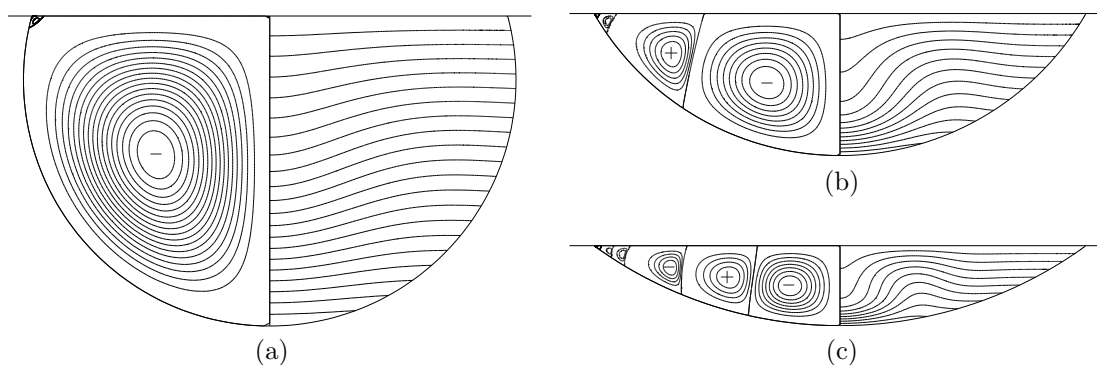


Figure 4.30: Pure buoyant flow in hanging droplets of different contact angles. (a) $\alpha = 105^\circ$, (b) $\alpha = 60^\circ$, and (c) $\alpha = 36^\circ$. Parameters are $Ra = 3360$, $Pr = 28$, $\theta_w = 0$, and $Bi = 100$.

can be claimed that the preferential aspect ratio is $\Gamma_{\text{cell}} \approx 1$ when the droplet is shallow enough such that the free surface can be assumed to be parallel to the substrate far from the contact line. This preferred aspect ratio can be examined for the discussed case of a droplet with the contact angle of $\alpha = 22.5^\circ$. Having in mind that the aspect ratio of the droplet is $l = L/R \approx 0.2$ and assuming the preferred aspect ratio of each convection cell to be $\Gamma_{\text{cell}} \approx 1$, one can expect to observe a chain of five convection cells for this droplet shape

$$N_{\text{cell}} = \frac{1}{l} \approx 5, \quad (4.10)$$

which is confirmed in figure 4.27h. In this case, the aspect ratio of each cell starting from the one close to the centerline of the droplet is $\Gamma \approx 0.93, 0.95, 0.91, 0.8$, and 0.35 , respectively. However, the aspect ratio cannot be exactly defined for larger contact angles in which the curvature of the liquid-gas interface increases. Nevertheless, it can give us a rough estimate. For instance, only one convective cell is observed for a droplet with a contact angle of $\alpha = 105^\circ$ in which the aspect ratio of the droplet is $l = 1.3$ (figure 4.30a). As another example, the droplet which is shown in 4.30b has the aspect ratio of $l \approx 0.6$ and two developed convection cells are evolved, $N_{\text{cell}} = 2$. The tiny cell close to the contact line is an extremely weak vortex which is viscously-driven.

4.2.3 Thermocapillary-buoyant flow

Unlike the case of a sessile droplet over a heated plate, there is no competition between the thermocapillary and buoyant forces in the case of combined thermocapillary-buoyant flow in hanging droplets attached to a cooled plate. That is because the tem-

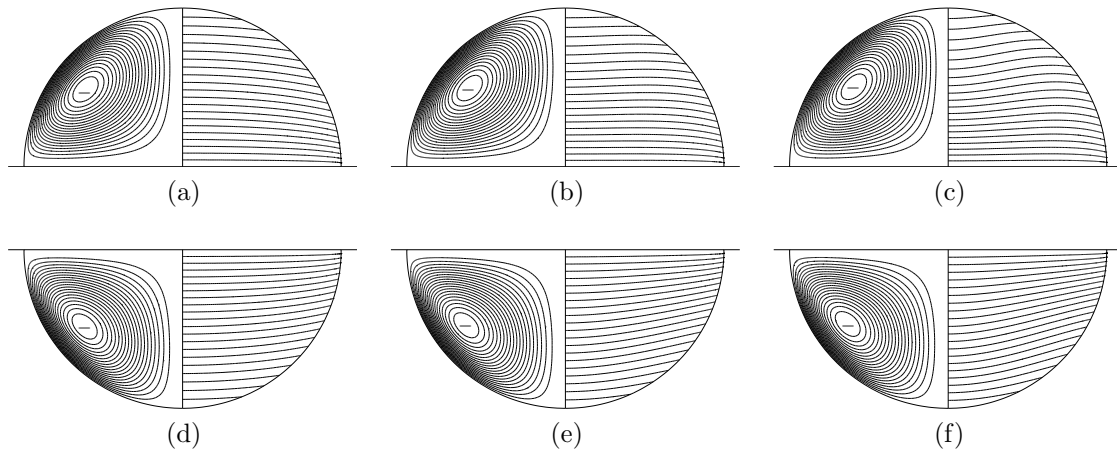


Figure 4.31: Streamlines and isotherms for sessile droplets sitting on a heated plate (upper row) as well as hanging droplets attached to a cooled plate (lower row) subject to the thermocapillarity. The parameters are $Bi = 0.5$, $\alpha = \pi/2$, $Gr = 0$, and (a,d) $Pr = 0.02$, $Re = 25$ (b,e) $Pr = 4$, $Re = 10$, (c,f) $Pr = 83$, $Re = 1$.

perature distribution is different in these two cases. To give a comparison between the temperature fields, figure 4.31 shows the isotherms for both heated (upper row) and cooled plate (lower row) cases in the absence of gravity ($Gr = 0$). The difference in the temperature distribution for three given Prandtl numbers is visually distinguishable in case of heated plate, which results in various buoyancy-driven flow motion if the level of gravity increases (see figure 4.18). In contrast, for all presented Prandtl numbers for the hanging droplets attached to a cooled plate, the temperature field has the same pattern with the isotherms which are bent slightly upwards close to the contact line. In this case, increasing the gravity level leads to the buoyancy-driven flow just in one direction (along the free surface toward the contact line), which is the same direction as the thermocapillary flow.

As discussed above, the buoyancy and thermocapillarity drive the flow in the same direction in case of a hanging droplet attached to a cooled plate independent of the Grashof, Prandtl, and thermocapillary Reynolds numbers. To prove this, figure 4.32 depicts the combined thermocapillary-buoyant flow in hanging droplets of different Prandtl numbers when the gravity level increases. Apart from the case of $Pr = 0.02$, for which the flow field and temperature distribution remain almost unchanged, increasing the gravity level enhances the thermocapillary-driven vortex and consequently amplifies the convective heat transport along the liquid-gas interface toward the contact line. This can be qualitatively seen comparing figures 4.32c and 4.32o. As a result, a large

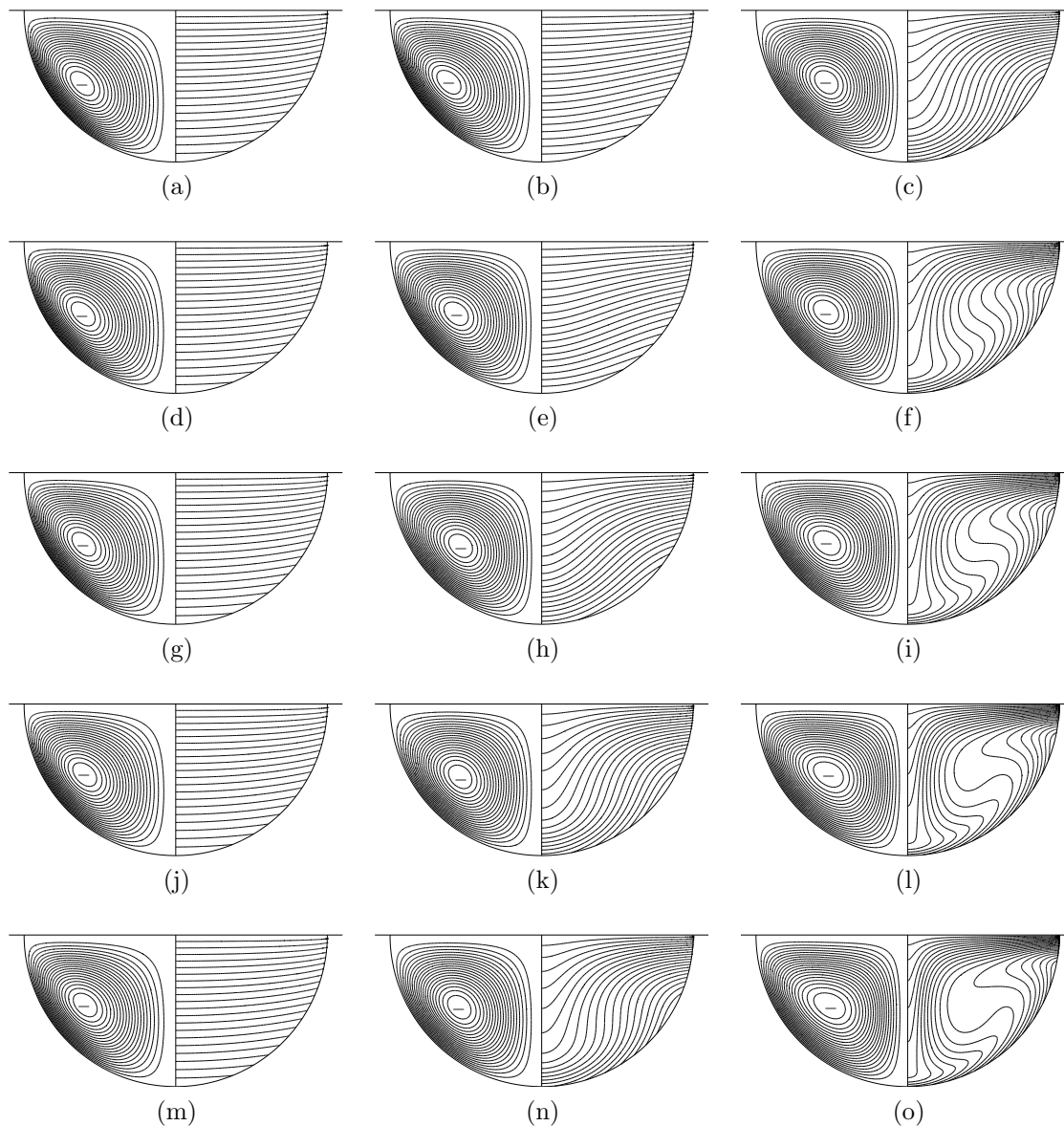


Figure 4.32: Combined thermocapillary-buoyant flow for $Bi = 0.5$, $\theta_w = 0$, and $\alpha = \pi/2$. Left column: $Pr = 0.02$ and $Re = 25$, middle column: $Pr = 4$ and $Re = 10$, and right column: $Pr = 83$ and $Re = 1$. The gravity level varies for all the columns from top to bottom with $Gr = 100, 500, 1000, 2000$ and 3000 .

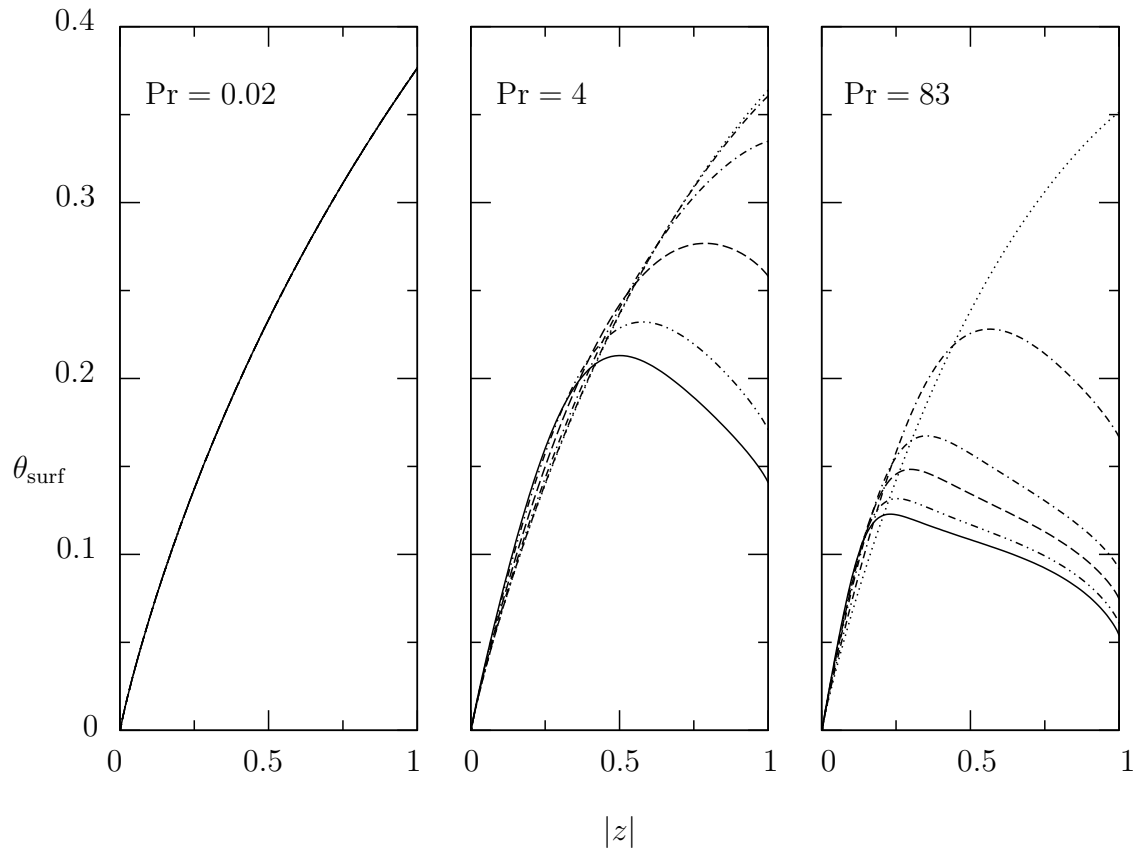


Figure 4.33: Free surface temperature as a function of distance $|z|$ from the substrate for the cases given in figure 4.32, with $\text{Gr} = 0$ (···), $\text{Gr} = 100$ (- - - - -), $\text{Gr} = 500$ (- · - · -), $\text{Gr} = 1000$ (- - - -), $\text{Gr} = 2000$ (· - · - ·), and $\text{Gr} = 3000$ (—).

temperature gradient appears in the cold corner and the cold fluid flows downward along the droplet's centerline (see e.g. figures 4.32n and 4.32o). This type of combined thermocapillary-buoyant convection results in an interesting evolution of the temperature distribution within the domain. As shown in figure 4.32h, the convective heat transport cools down the apex of the droplet and the maximum temperature in the domain shifts upward along the free surface. The location of the temperature maximum can be found at the free surface where both ends of a temperature isoline are fixed to the free surface. By increasing the gravity level, this point moves toward the cold corner. For higher Prandtl number, $\text{Pr} = 83$, the temperature maximum arrives very close to the contact line which leads to a larger temperature gradient in the vicinity of the cold corner (4.32o). In this case, a thermal boundary layer develops along the flat substrate.

Plotting the temperature along the free surface, θ_{surf} , as a function of the vertical distance from the substrate leads to a better understanding of the convection details.

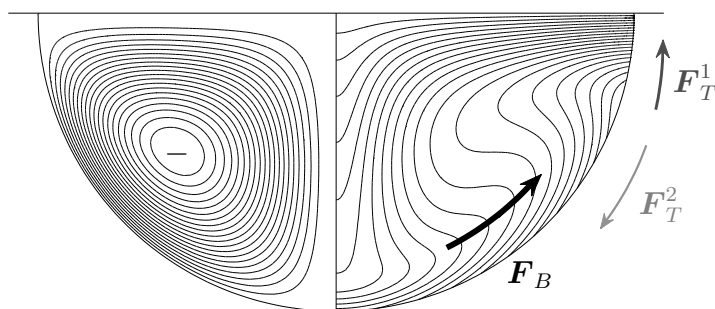


Figure 4.34: Driving forces acting on a hanging droplet: Buoyant body force, \mathbf{F}_B , and two opposing thermocapillary surface forces, \mathbf{F}_T^1 and \mathbf{F}_T^2 . The parameters are $Re = 10$, $Pr = 4$, $Bi = 0.5$, $Gr = 1000$, $\theta_w = 0$, and $\alpha = \pi/2$. The color and thickness of each arrow is proportional to the strength of each driving force.

The free surface temperatures of all the cases presented in figure 4.32 are sketched in figure 4.33. As expected, all the curves are lying on top of each other for $Pr = 0.02$ ($Ma = 1$) since the thermal convection is negligible even for large Grashof numbers. In contrast, the free surface temperature becomes more sensitive to the gravity level variation for higher Prandtl numbers. The maximum peaks appearing in case of $Pr = 4$ and 83 result in more complicated thermocapillary-driven forces which drive the flow in two opposing directions up- and downward along the free surface. However, for a range of low thermocapillary Reynolds numbers considered here, these opposing thermocapillary forces are weak compared to the dominating buoyancy.

All the discussed driving forces are sketched in figure 4.34, which perceptibly summarizes the direction and strength of the forces. Here \mathbf{F}_B represents the buoyant body force (thick, black arrow) which dominates the flow, whereas \mathbf{F}_T^1 and \mathbf{F}_T^2 are the two opposing thermocapillary forces. \mathbf{F}_T^2 (thin, light grey arrow) is much weaker than \mathbf{F}_T^1 (dark grey arrow) since the temperature gradient close to the cold corner is much larger than the one in the hot ambient side (see the corresponding curve in figure 4.33, right column, $Gr = 1000$).

The combined thermocapillary-buoyant convection results in even more complicated flow fields in case of shallow hanging droplets. In order to make it comparable with the pure buoyancy-driven flow (figure 4.27), identical parameters have been chosen, plus a moderate thermocapillary Reynolds number ($Re = 20$) such that the influence of both the driving forces could be recognized. The results are illustrated in figure 4.35 for the mentioned parameters varying the Rayleigh number. The pure thermocapillary-driven force (4.35a) leads to the development of a single toroidal vortex. Increasing the

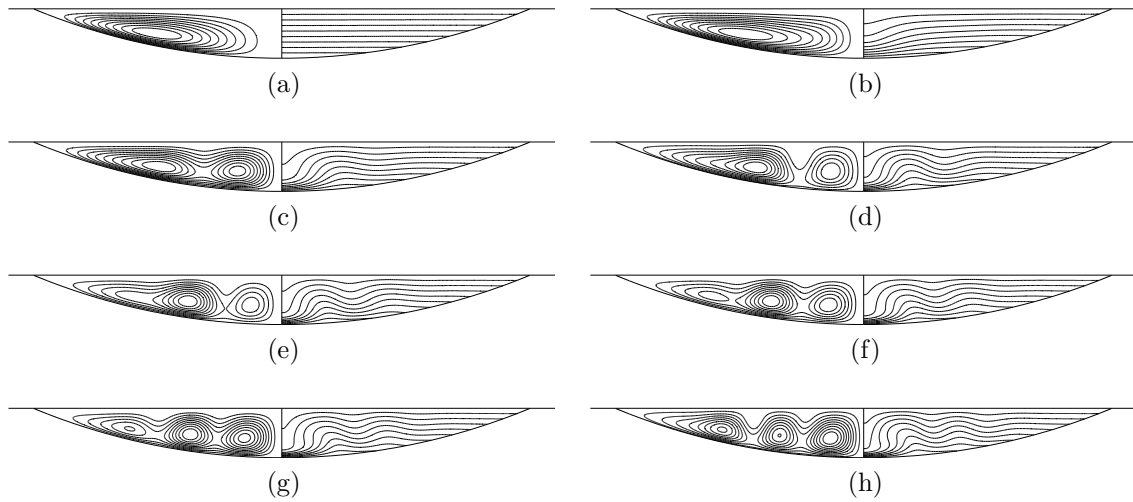


Figure 4.35: Mixed thermocapillary-buoyant flow in a shallow hanging droplet; gravity level variation for $Re = 20$, $Pr = 28$, $Bi = 100$, $\theta_w = 0$, and $\alpha = 22.5^\circ$. (a) $Ra = 0$, (b) $Ra = 1120$, (c) $Ra = 1960$, (d) $Ra = 2240$, (e) $Ra = 2800$, (f) $Ra = 3360$, (g) $Ra = 3920$, and (h) $Ra = 4480$.

gravity level enhances the convective heat transport and a cat's eye structure evolves as shown in figure 4.35c. This flow structure is visually similar and comparable to a pure buoyant case (see figure 4.27b) although the stream function magnitude is much larger in the combined case. For larger Rayleigh numbers, instead of a cellular flow pattern which was found for pure buoyant flow, a multi-roll structure develops consisting of a global circulation which envelops a series of co-rotating inner vortices. It can be claimed that the global circulation is mainly driven by the thermocapillarity along the surface, whereas the inner vortices are stimulated by the buoyancy which is a body force. The number of these inner vortices are less than the number of convective cells in pure buoyant flow as the co-rotating vortices are stretched in horizontal direction by the thermocapillary stresses, especially close to the contact line (figure 4.35h). For the current setup where the contact angle is $\alpha = 22.5^\circ$, the maximum number of co-rotating vortices is three.

Having the results for the buoyancy-driven, the thermocapillary-driven, and the combined thermocapillary-buoyant flows, it is desired to compare the flow behavior between these cases. However, it should be taken into account that the results are obtained employing two different scalings of the governing equations. Therefore, the value of stream function (or generally the velocity) has to be rescaled from one to the other, i.e. from thermocapillary to viscous scaling. This rescaling allows one to compare the results of different cases.

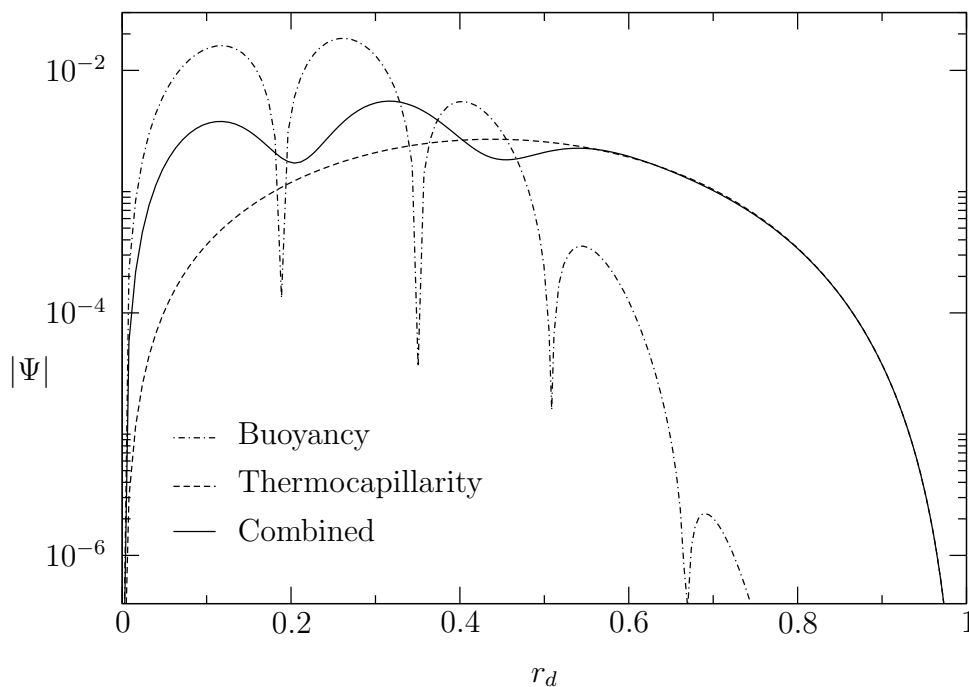


Figure 4.36: $|\Psi|$ along ξ_{mid} as a function of the dimensionless radial distance from the centerline r_d for the pure buoyant flow (figure 4.27g), pure thermocapillary-driven flow (figure 4.35a), and the combined thermocapillary-buoyant flow (figure 4.35f). The parameters are $\text{Pr} = 28$, $\text{Bi} = 100$, $\theta_w = 0$, and $\alpha = 22.5^\circ$.

The stream function magnitude along ξ_{mid} is exhibited in figure 4.36 for the three discussed cases: pure buoyancy-driven flow (figure 4.27g), pure thermocapillary-driven flow (figure 4.35a), as well as the combined thermocapillary-buoyant flow (figure 4.35f). At first glance, a slight difference in stream function magnitude can be observed between the buoyant flow and the other two types of flow although the gravity level is similar in all the cases ($\text{Ra} = 3360$). To find the reason for this difference, it is necessary to analyze the evolution of the flow from the pure thermocapillary-driven flow to a combined case by increasing the gravity level from $\text{Ra} = 0$ to 3360. Comparing these two cases (dashed and solid lines in figure 4.36) shows that the effect of buoyancy which tries to form the convective cells in the bulk is damped with the thermocapillary stresses driving a global flow along the free surface. The stream function for these two cases has the same order of magnitude. As a result, the combined flow consists a general circulation which envelops a series of co-rotating vortices as shown in figure 4.35h.

In the combined thermocapillary-buoyant flow and for $r_d < 0.5$, the buoyancy dominates the flow; therefore, the co-rotating vortices develop in this region. A series of

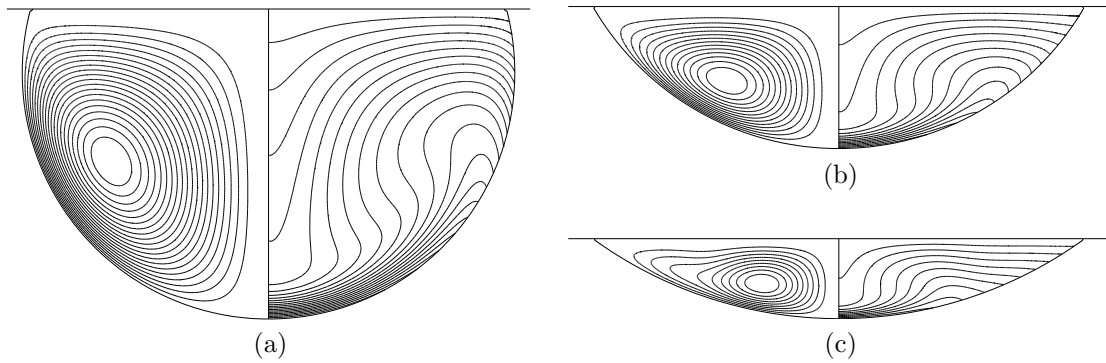


Figure 4.37: Mixed thermocapillary-buoyant flow in hanging droplets of different contact angles. (a) $\alpha = 105^\circ$, (b) $\alpha = 60^\circ$, and (c) $\alpha = 36^\circ$. Parameters are $Re = 20$, $Ra = 3360$, $\theta_w = 0$, and $Bi = 100$.

local extrema which is observed in the solid curve in figure 4.36 corresponds to these co-rotating flow structures. On the other hand, for $r_d > 0.5$ the thermocapillarity is dominant and the curves corresponding to the thermocapillary and combined flows are stacked on top of each other. The reason for that can be explained by the definition of the local Rayleigh number which is discussed before (see figure 4.28).

Referring to the case of pure buoyant flow (dash-dotted line in figure 4.36), the stream function is slightly larger than in the other two cases (thermocapillary and combined thermocapillary-buoyant flows) when $r_d < 0.5$. However, close to the cold corner, the local Rayleigh number is tending to zero in the pure buoyant case; therefore, the stream function decays in this region much steeper than in the cases in which thermocapillarity drives the flow. In addition, comparing the radial position of the peaks in the curves corresponding to the pure buoyant and combined flows show that the centers of the vortices in the case of combined flow are shifted radially outward substantially. In the combined flow, the thermocapillary force drives a global flow along the free surface from the apex of the droplet toward the contact line in this setup which suggests the reason for the displacement of vortices in the droplet. As a result, the number of co-rotating vortices (elliptic points) in the combined flow is always less than the number of convection cells in the pure buoyant flow. For the given contact angle of $\alpha = 22.5^\circ$, the number of visually observed convection cells is $N_{\text{cell}} = 5$ in the pure buoyant flow, while only three co-rotating vortices are detected in the combined thermocapillary-buoyant flow (see figures 4.27h and 4.35g).

The effect of contact angle variation on the combined thermocapillary-buoyant flow is illustrated in figure 4.37. By increasing the contact angle the thermocapillarity becomes

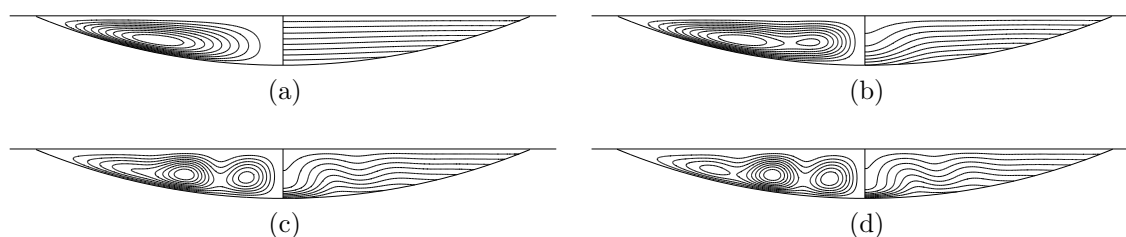


Figure 4.38: Mixed thermocapillary-buoyant flow in a shallow hanging droplet. Biot number variation for $Re = 20$, $Pr = 28$, $Ra = 3360$, $\theta_w = 0$, and $\alpha = 22.5^\circ$. (a) $Bi = 0.1$, (b) $Bi = 1$, (c) $Bi = 10$, and (d) $Bi = 100$. Temperature at the droplet's apex is (a) $\theta_{\text{apex}} = 0.152$, (b) $\theta_{\text{apex}} = 0.452$, (c) $\theta_{\text{apex}} = 0.783$, and (d) $\theta_{\text{apex}} = 0.964$.

stronger (see figure 4.7) and dominates the flow. In figure 4.37c, the streamlines are elongated toward the contact line, but the cat's eye structure is not generated as in figure 4.35f although all the parameters except the contact angle are the same in these two cases. For larger contact angles, the dominance of the thermocapillary stresses results in a single toroidal vortex. The thermal and thermocapillary convections in the bulk leads to compressed isotherms at the bottom of the droplet and consequently, development of a thermal boundary layer along the liquid-gas interface which becomes thinner by increasing the contact angle (figure 4.37a).

In all the combined thermocapillary-buoyant cases discussed above, a very large Biot number ($Bi = 100$) was considered in order to compare the results with the pure buoyant case. However, it is important to examine the influence of Biot number variation on the fluid flow. Figure 4.38 depicts the stream lines and isotherms for a wide range of Biot numbers. For a low Biot number $Bi = 0.1$, the effective temperature difference is small ($\theta_{\text{eff}} = \theta_{\text{apex}} = 0.152$); therefore, the buoyant forces are weak and the flow is mainly driven by the thermocapillarity. Yet, the flow is very weak and no convection can be observed in the temperature field in figure 4.38a. However, the buoyant forces become dominant by increasing the Biot number and again, a co-rotating flow structure evolves, starting with a two-vortex structure as shown in figure 4.38b and further developing to a three-vortex structure which is evident in figure 4.38d. For all the cases, the convective heat transfer is much stronger close to the droplet's centerline than in the vicinity of the cold corner.

As the final topic to be discussed in this chapter, the combined thermocapillary-buoyant flow in a sessile droplet attached to a cooled substrate is investigated, with similar parameters as in the presented case of hanging droplets attached to a heated plate (see

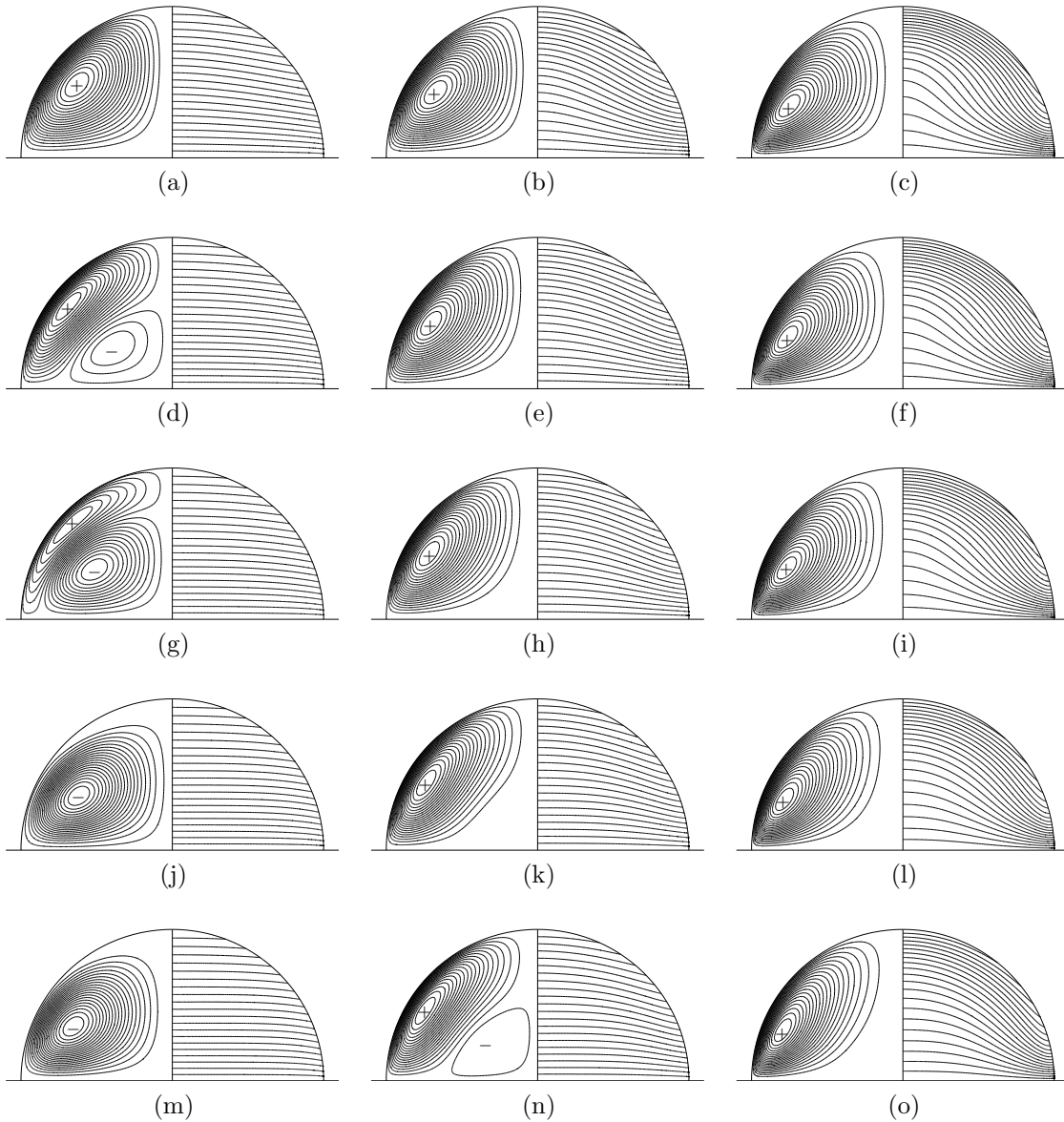


Figure 4.39: Combined thermocapillary-buoyant flow in a sessile droplet sitting on a cooled plate; $Ma = 28$ (left column), $Ma = 280$ (middle column), and $Ma = 2800$ (right column). The parameters are $Pr = 28$, $Bi = 1$, $\alpha = 90^\circ$, and (a,b,c) $Gr = 10$, (d,e,f) $Gr = 80$, (g,h,i) $Gr = 120$, (j,k,l) $Gr = 240$, (m,n,o) $Gr = 360$.

Gr	Ma = 28		Ma = 280		Ma = 2800	
	$\Psi_{\max} \times 10^3$	$\Psi_{\min} \times 10^3$	$\Psi_{\max} \times 10^3$	$\Psi_{\min} \times 10^3$	$\Psi_{\max} \times 10^3$	$\Psi_{\min} \times 10^3$
10	24.95	≈ 0	18.32	≈ 0	6.071	≈ 0
80	7.541	-1.373	14.36	≈ 0	5.840	≈ 0
120	3.538	-5.385	12.78	≈ 0	5.720	≈ 0
240	0.498	-16.14	9.576	-0.103	5.385	≈ 0
360	0.133	-23.39	7.617	-0.410	5.089	-0.006

Table 4.8: Stream function maximum, Ψ_{\max} (thermocapillary-driven vortex), and minimum, Ψ_{\min} (buoyancy-driven vortex), for the cases shown in figure 4.39.

figure 4.20). For a heated plate, the effects of buoyancy were found to be negligible. In contrast, as shown in figure 4.39, the buoyant effects on the flow field are more visible for sessile droplets on a cooled plate. Considering the left column (Ma = 28) in which the thermocapillary stresses are weak, the buoyant forces drive a counter-rotating vortex driven by horizontal gradients of temperature initiating from the center of the droplet. By increasing the Grashof number this vortex grows and dominates the flow. Consequently, the counter-clockwise thermocapillary-driven vortex (marked with '+' sign) is squeezed toward the liquid-gas interface (figure 4.39m).

For a relatively higher Marangoni number (middle column), the thermocapillary forces are stronger. Therefore, the buoyancy-driven vortex (a separation from the substrate due to the rise of hot fluid) can start to develop only for very high Grashof numbers (figure 4.39n). In the right column where the Marangoni number is even higher, competing buoyant forces are much smaller in magnitude and the flow is fully driven by the thermocapillary stresses along the free surface. Table 4.8 lists the strength of thermocapillary-driven as well as buoyancy-driven vortices which are presented in figure 4.39. According to the given values of the stream function extremum, buoyancy-driven vortex dominates the flow only in case of Ma = 28 and with Gr > 120. In all the other cases, the thermocapillary-driven vortex is much stronger than the buoyant one and dominates the flow field.

Chapter 5

Axisymmetric Linear Stability Analysis

In this section, an axisymmetric linear stability analysis is undertaken for the buoyancy-driven, thermocapillary-driven, and combined thermocapillary-buoyant-driven flows in liquid droplets. Solving the generalized eigenvalue problem (3.54), the leading eigenvalues, γ , with the smallest decay rate, μ , and corresponding two-dimensional eigenvectors, $\hat{\mathbf{x}}$, are detected. It is then possible to find the onset of axisymmetric instability by varying different parameters.

For the buoyancy-driven flow this leads to finding the onset of instability. On the other hand, existence of the onset of axisymmetric flow (wave number $m = 0$) in thermocapillary-driven flows has to be examined by varying the Marangoni number. Three-dimensional instabilities which occur at quite low Marangoni numbers have been found and thoroughly discussed for evaporating droplets (see Karapetsas et al., 2012). Nevertheless, the instabilities due to the pure thermocapillarity have not been studied yet. As a first step, the axisymmetric stability analysis of thermocapillary-driven flows in liquid droplets is provided in this chapter.

5.1 Pure buoyant flow

In case of the pure buoyant flow, parallel horizontal isotherms within the domain are considered as shown in figure 4.13a. This static vertical temperature gradient triggers an instability when the Rayleigh number reaches its neutral value, Ra_n (Chandrasekhar, 1961). Here the aim is to obtain the neutral Rayleigh number for droplets of different contact angles subject to a vertical thermal gradient, which has not been studied previously.

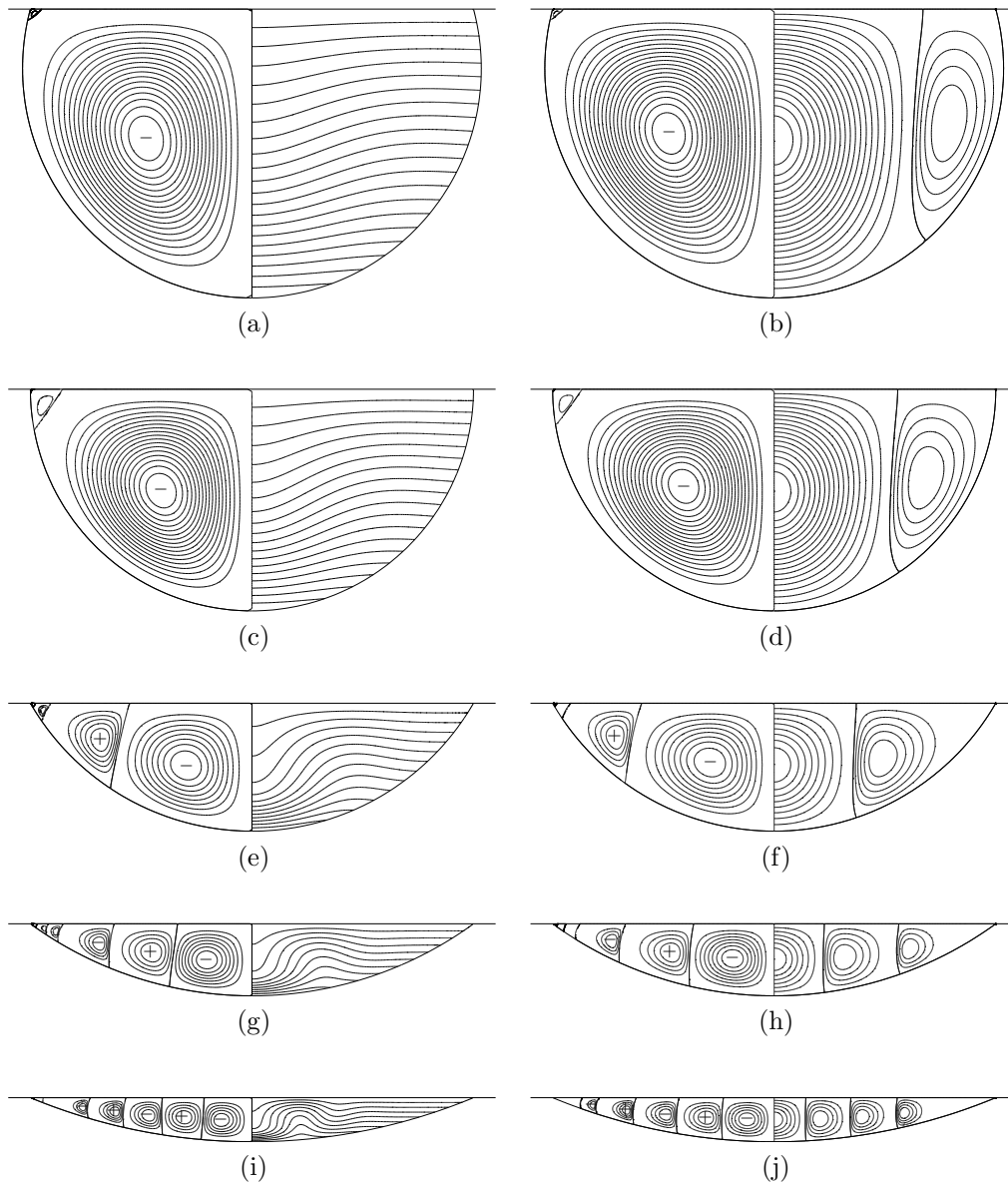


Figure 5.1: Streamlines and isotherms for an unstable flow ($Ra = 3920$, left column) and the eigenvector isolines corresponding to the neutral modes of stream function and temperature ($Ra = Ra_n$, right column). The parameters are $Pr = 28$, $\theta_w = 0$, $Bi \rightarrow \infty$, (a,b) $\alpha = 105^\circ$, (c,d) $\alpha = 90^\circ$, (e,f) $\alpha = 60^\circ$, (g,h) $\alpha = 36^\circ$, and (i,j) $\alpha = 22.5^\circ$

Hanging droplets of different contact angles which are shown in figures 4.27 and 4.30 have been considered. In order to find the most dangerous eigenvalues for each droplet, the generalized eigenvalue problem (3.54) is solved varying the Rayleigh number. By increasing the Rayleigh number ($Ra > Ra_n$), infinitesimal perturbations grow in time (Rayleigh-Bénard instability mechanism) and consequently, the flow becomes unstable (Lord Rayleigh, 1916).

The onset of instability is detected when the decay rate becomes negative, $\mu < 0$. Figure 5.1 shows the streamlines and isotherms in droplets with different contact angles when the flow is unstable ($Ra = 3920$, left column) as well as the eigenvector isolines corresponding to the neutral mode of stream function and temperature for the each droplet (right column) when $Ra = Ra_n$. The isolines of stream function of neutral mode (the left half of each droplet) exhibit the same structure (but much smaller amplitude) as the streamlines which are developed when the flow is unstable which is quite evident since the fluid flow within the droplet is initiated only by the buoyancy-driven perturbations. Similarly, comparing the deflections in isotherms (basic state results) with the position of separating isotherms corresponding to the neutral modes show that the solutions of the nonlinear supercritical equations (left column) are compatible with the axisymmetric neutral modes (right column). It should be mentioned that two sets of neutral solutions exist in which the eigenvectors have the same magnitude, but have different signs. In order to keep the results of the linear stability solver comparable with the obtained results of the basic state flow, only one branch of the solutions are presented here.

Figure 5.2 depicts the neutral Rayleigh number as a function of droplet's contact angle. To produce this neutral curve, the generalized eigenvalue problem has been solved for a wide range of contact angles $\alpha \in [9, 145]$ with the step size of $\Delta\alpha = 1$ in order to provide a high resolution stability curve. The resulting curve shows that in the limit of small contact angles, $\alpha \rightarrow 0$, for which the droplet can be assumed as an infinite axisymmetric thin film, the neutral Rayleigh number converges to $Ra_n^{\alpha \rightarrow 0} \approx 1700$. The obtained neutral Rayleigh number is comparable with the results presented by Vrentas et al. (1981) for an axisymmetric buoyancy-driven convection in cylindrical geometries (with a free-surface at the top) when the Prandtl number is large. They reported that the neutral Rayleigh number varies in the interval of $Ra_n \in [1100, 2000]$ depending on the aspect ratio of the cylindrical pool.

The neutral Rayleigh number is investigated for different Prandtl numbers ($Pr = 1, 4$, and 83). For all the cases, the same critical value has been detected, which shows that the obtained onset of instability is independent of the Prandtl number (Korpela et al.,

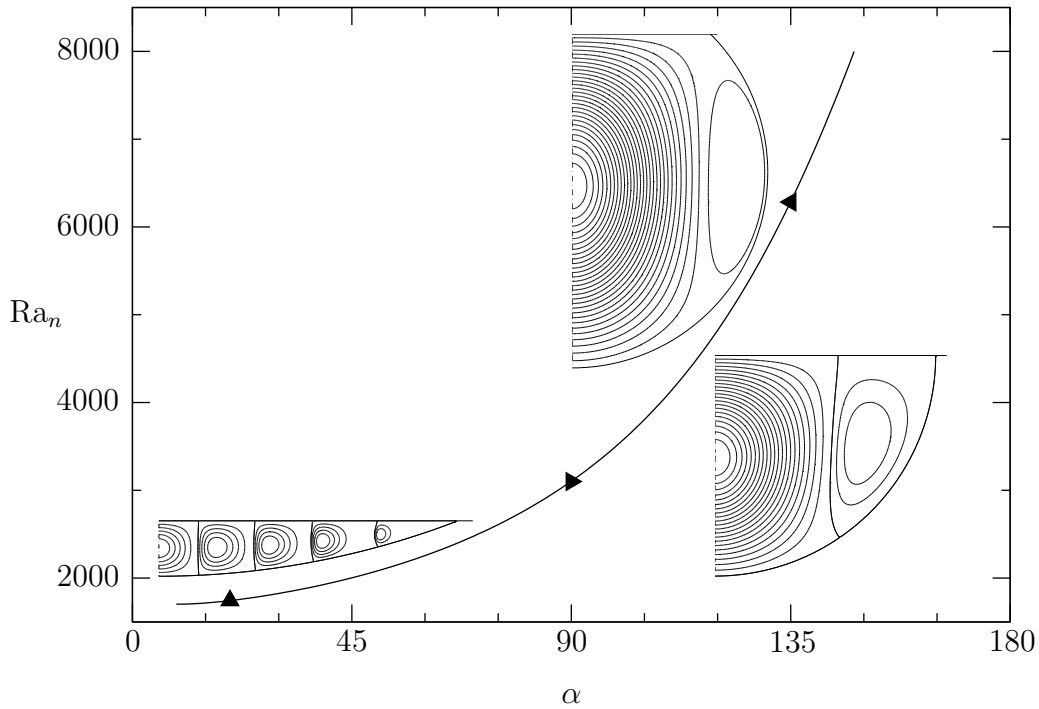


Figure 5.2: Neutral curve, pure buoyant flow with $\text{Bi} \rightarrow \infty$. Neutral mode isotherms are plotted for hanging droplets with three different contact angles $\alpha = 20^\circ$ (\blacktriangle), $\alpha = 90^\circ$ (\blacktriangleright), and $\alpha = 135^\circ$ (\blacktriangleleft). The parameters are the same as in figure 5.1

1973; Hwang and Cheng, 1973). This cannot be easily shown using the employed scaling of the governing equations because the Grashof number appears in the momentum equation (2.14a), while the Prandtl number shows up in the energy equation (2.14c). Instead, the independence of the neutral Rayleigh number from the Prandtl number is explained considering another scaling of the equations in the Boussinesq approximation as in Busse (1986). The governing equations for the total flow read

$$(\partial_t + \mathbf{u} \cdot \nabla) \mathbf{u} = \text{Pr} (-\nabla p + \nabla^2 \mathbf{u} + \text{Ra} \theta \mathbf{k}), \quad (5.1a)$$

$$\nabla \cdot \mathbf{u} = 0, \quad (5.1b)$$

$$(\partial_t + \mathbf{u} \cdot \nabla) \theta = \nabla^2 \theta. \quad (5.1c)$$

Substituting (2.16) into the governing equations (5.1), subtracting the basic flow, and linearizing the equations, we have

$$(\partial_t \tilde{\mathbf{u}} + \tilde{\mathbf{u}} \cdot \nabla \mathbf{U}_0 + \mathbf{U}_0 \cdot \nabla \tilde{\mathbf{u}}) = \text{Pr} (-\nabla \tilde{p} + \nabla^2 \tilde{\mathbf{u}} + \text{Ra} \tilde{\theta} \mathbf{k}), \quad (5.2a)$$

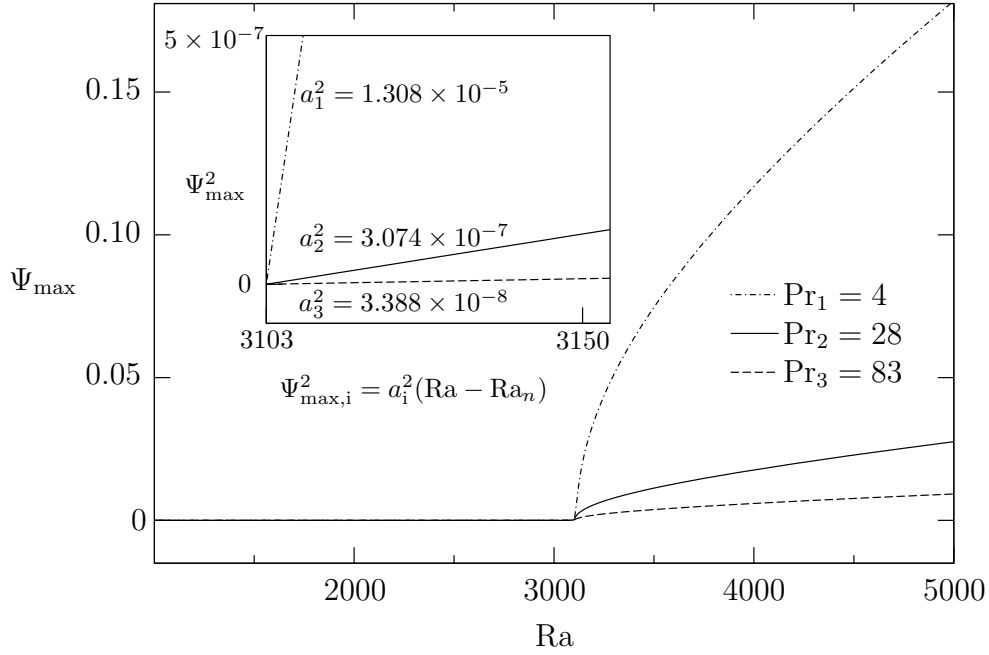


Figure 5.3: Maximum of Ψ as a function of the Rayleigh number for $\alpha = \pi/2$, $\theta_w = 0$, and $\text{Bi} \rightarrow \infty$. The inner graph presents fits to the expected square root law ($\Psi_{\max,i} = a_i \sqrt{\text{Ra} - \text{Ra}_n}$) for different Prandtl numbers.

$$\nabla \cdot \tilde{\mathbf{u}} = 0, \quad (5.2b)$$

$$\left(\partial_t \tilde{\theta} + \tilde{\mathbf{u}} \cdot \nabla \theta_0 + \mathbf{U}_0 \cdot \nabla \tilde{\theta} \right) = \nabla^2 \tilde{\theta}. \quad (5.2c)$$

Considering (5.2), the Prandtl and the Rayleigh numbers only appear in the momentum equation (5.2a). In the subcritical regime, the liquid is at rest (no flow motion); therefore, the basic flow terms are zero (second and third terms in the left hand side). Moreover, for the Rayleigh number corresponding to the neutral state, the perturbations neither grow nor decay (when the oscillation frequency $\omega = 0$). Consequently, the time derivative of the perturbations in the left hand side of (5.2a) becomes zero. As a result, in order to find the neutral Rayleigh number (5.2a) can be written as

$$-\nabla \tilde{p} + \nabla^2 \tilde{\mathbf{u}} + \text{Ra} \tilde{\theta} \mathbf{k} = 0. \quad (5.3)$$

The only dimensionless number in the governing equations is then the Rayleigh number, which confirms the independence of the neutral Rayleigh number from the Prandtl number. However, development of the flow field is not similar for different Prandtl numbers in the supercritical regime. In order to verify this, figure 5.3 sketches the

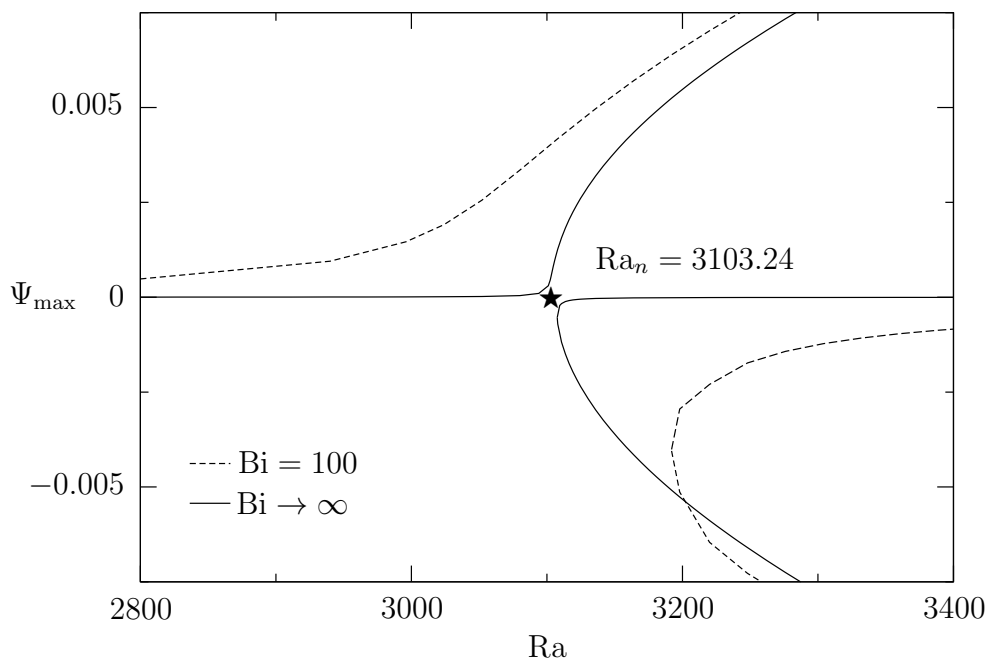


Figure 5.4: Extremum of Ψ as a function of the Rayleigh number for $\text{Pr} = 28$, $\theta_w = 0$, and $\alpha = \pi/2$. The '★' sign shows the neutral Rayleigh number obtained from the linear stability analysis.

upper branch of the pitchfork bifurcation for three different relatively large Prandtl numbers $\text{Pr} = 4, 28$, and 83 . It is clear that the neutral Rayleigh number remains unchanged for all the provided cases, whereas the development of the flow field in the supercritical regime is quite similar, with different amplitudes.

For the lowest Prandtl number presented here, $\text{Pr} = 4$, the Grashof number have to be much larger than the other cases to reach the neutral Rayleigh number $\text{Gr}_n = \text{Ra}_n/\text{Pr} \approx 776$. Therefore, in the supercritical regime, the extremum of the stream function (when $\text{Ra} > \text{Ra}_n$) is much larger for the low Prandtl number liquid ($\text{Pr} = 4$) than the other ones as it is shown in figure 5.3. In other words, the toroidal convection cell is stronger for lower Prandtl numbers. The fit to the expected square-root law

$$\Psi_{\max,i} = a_i \sqrt{\text{Ra} - \text{Ra}_n} \quad (5.4)$$

has been shown in the inner graph of figure 5.3 plotting Ψ_{\max}^2 as a function of Rayleigh number, in which constants a_i are given for different Prandtl numbers.

The onset of instability for a sessile droplet sitting on a heated plate and a hanging droplet attached to a cooled plate is found to be the same. Therefore, the neutral curve given in figure 5.2 is valid for both the cases. The basic state solutions obtained for a

sessile droplet subject to pure buoyant forces lead to detecting a pitchfork bifurcation (see figure 4.16) for a droplet with the contact angle of $\alpha = 90^\circ$. In order to compare the onset of instability obtained from the linear stability solver with the results of the basic state flow, the neutral Rayleigh number for $\alpha = 90^\circ$ is plotted together with the bifurcation curves for $\text{Bi} = 100$ as well as $\text{Bi} \rightarrow \infty$ in figure 5.4. As discussed before, the bifurcation curve in case of $\text{Bi} = 100$ is perturbed as a result of a temperature gradient imperfection (Mullin, 1993). Even for $\text{Bi} \rightarrow \infty$, the pitchfork bifurcation is not perfectly symmetrical due to the errors of the numerical scheme (Barten et al., 1989). Nevertheless, the turning point of the upper stable branch in both curves is very close to the obtained neutral Rayleigh number, $\text{Ra}_n = 3103.24$, which is highlighted in figure 5.4.

5.2 Thermocapillary flow

In this section, the axisymmetric stability of the thermocapillary-driven flow in sessile droplets sitting on a heated plate is investigated. Similar to the pure buoyant case, the generalized eigenvalue solver is employed, the basic state results are used as an input to the solver, and the linear stability of the flow is analyzed varying the most influential parameter in the thermocapillary driven flow, the Marangoni number. When the real part of the most dangerous eigenvalue becomes negative (because we are considering the decay rate), the flow will be axisymmetrically unstable. Then the corresponding Marangoni number is the neutral Marangoni number, Ma_n .

In order to find neutral axisymmetric instabilities in a sessile droplet attached to a heated plate with the contact angle of $\alpha = 90^\circ$, the most dangerous eigenvalues are found varying the Marangoni number for three different Biot numbers ($\text{Bi} = 0.1, 1$, and 20). The results are illustrated in figure 5.5 in logarithmic scale which shows that the real part of the most dangerous eigenvalue decays with the slope of -1 , $\Re(\gamma_{\min}) \sim \text{Ma}^{-1}$, independent of the Biot number. Therefore, it can be concluded that $\Re(\gamma_{\min})$ never turns negative for any value of Marangoni number. In other words, the thermocapillary-driven flow in a sessile droplet with a contact angle of 90° is linearly stable for the azimuthal mode $m = 0$. A similar behavior was obtained by Nienhüser and Kuhlmann (2002) for the thermocapillary-driven flows in non-cylindrical liquid bridges with a static free-surface shape. Since all the obtained most dangerous eigenvalues are real, it suffices to show γ_{\min} rather than $\Re(\gamma_{\min})$. It should be also noted that the results are independent of the Prandtl number, when the Prandtl number is relatively large ($\text{Pr} > 1$) and the only characterizing parameter is the Marangoni

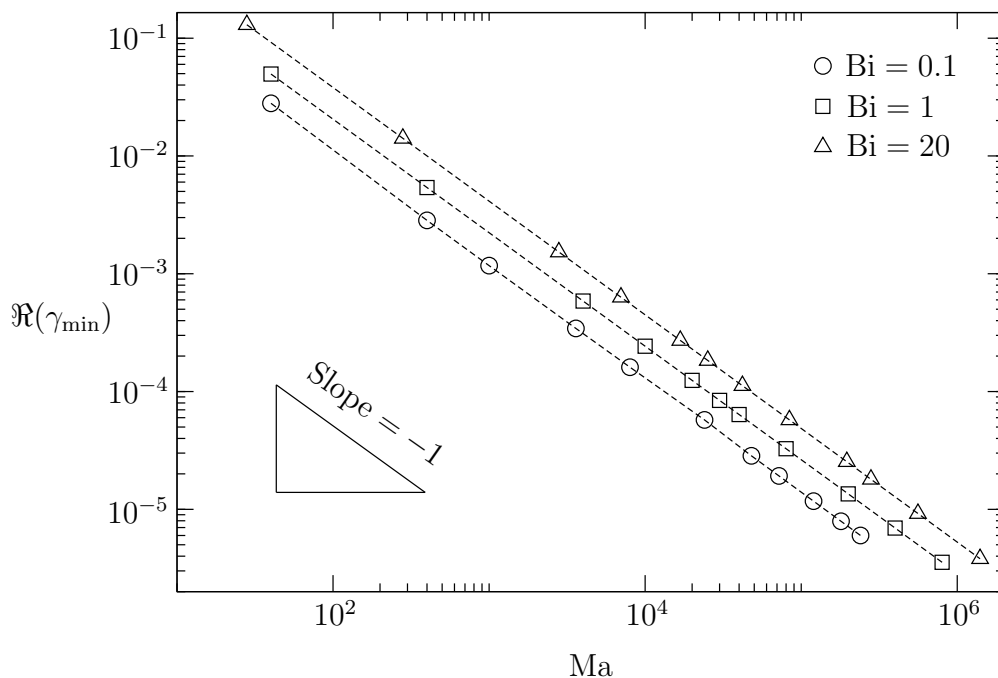


Figure 5.5: Real part of the most dangerous eigenvalue, $\Re(\gamma_{\min})$, as a function of Marangoni number for the thermocapillary-driven flow. The parameters are $Gr = 0$, $\theta_w = 1$, and $\alpha = 90^\circ$. The dashed lines are guides to the eye.

number. The discrete points which are plotted in figure 5.5 can be obtained employing any Prandtl number larger than 1 and modifying the Reynolds number.

In contrast, for very low Prandtl numbers, the eigenvalues and eigenvectors evolve quite differently. Figure 5.6 depicts the smallest eigenvalues as a function of Marangoni number for a relatively large Prandtl number as well as for $Pr = 0.02$. Although the flow in case of low Prandtl number is also linearly stable, the slope of the curve is different from the other Prandtl numbers ($\gamma_{\min} \sim Ma^{-0.8}$). Moreover, the eigenvectors which are sketched for the same Marangoni number, exhibit different structures. The stream function perturbations form a single toroidal vortex when $Pr > 1$, while for the low Prandtl number the main central toroidal vortex is bounded between two weaker counter-rotating vortices, one close to the apex and the other in the vicinity of the contact line. The differences between low and high Prandtl numbers were also identified in the basic state results (see figures 4.5 and 4.23).

The stream function and temperature neutral modes (which are decaying exponentially in time) for different Marangoni numbers are shown in the right column of figure 5.7. The corresponding basic state flow and temperature fields for each case is sketched side by side in the left column of the same figure. The stream function perturbations for

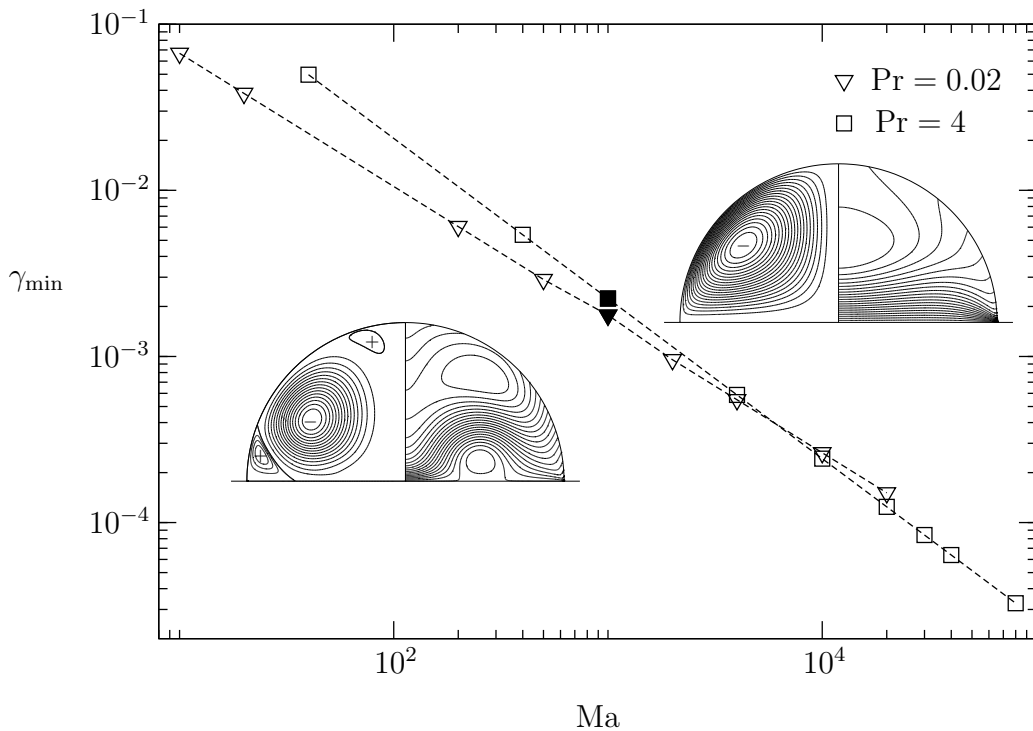


Figure 5.6: The most dangerous eigenvalue, γ_{\min} , as a function of Marangoni number for the thermocapillary-driven flow. The parameters are $Bi = 1$, $Gr = 0$, $\theta_w = 1$, and $\alpha = 90^\circ$. The dashed lines are guides to the eye.

low Marangoni numbers form two counter-rotating vortices where the clockwise vortex ('-') is stronger in magnitude. These vortices develop due to the surface tension which drives the perturbations in two opposite directions; one from the contact line upward, and the other from the apex of the droplet downward along the free surface. The perturbation isotherms illustrate the corresponding thermal gradients along the liquid-gas interface. By increasing the Marangoni number, the structure of the flow field for the basic state results and the neutral modes become similar. For $Ma = 4000$, the clockwise vortex shown in figure 5.7h dominates the perturbation field and exhibits nearly the same structure as in the streamlines of the basic state which are plotted in figure 5.7g. A weak deflection of the streamlines close to the contact line (figure 5.7g) and the small counter-clockwise vortex ('+') in figure 5.7h are in the same region. Furthermore, the perturbation isotherms exhibit a single core oblate shape structure for low Marangoni numbers as it is shown in figure 5.7b, whereas by increasing the Marangoni number and the development of thermal boundary layers in the basic state results, the single core turns into a toroidal structure with a strong gradient close to the substrate (figure 5.7f).

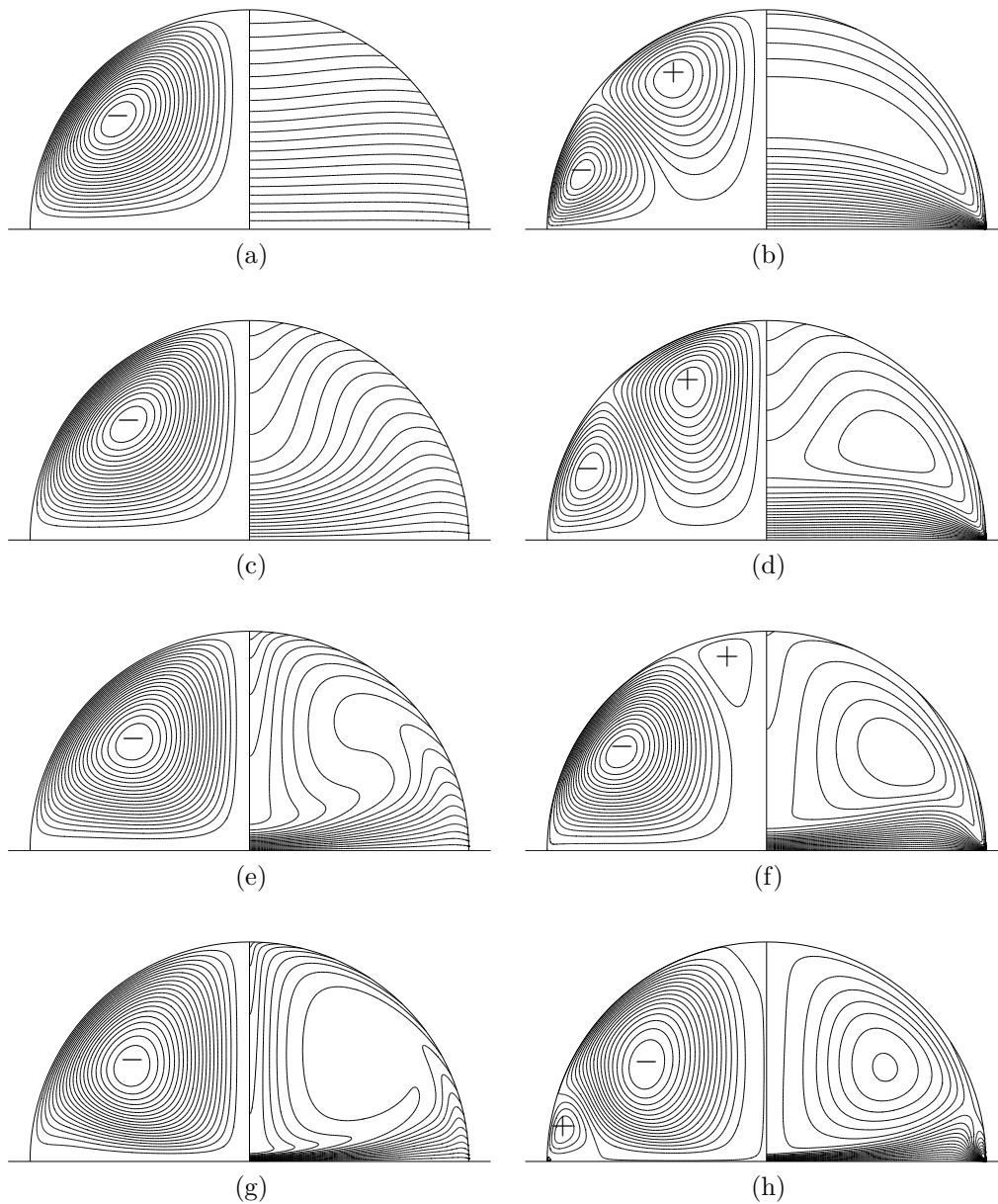


Figure 5.7: Streamlines and isotherms for thermocapillary-driven flow (left column) and the eigenvector isolines corresponding to the most dangerous mode of stream function and temperature (right column). The parameters are $Pr = 4$, $Bi = 1$, $Gr = 0$, $\theta_w = 1$, $\alpha = 90^\circ$, and (a,b) $Ma = 40$, (c,d) $Ma = 400$, (e,f) $Ma = 4000$, (g,h) $Ma = 4 \times 10^4$.

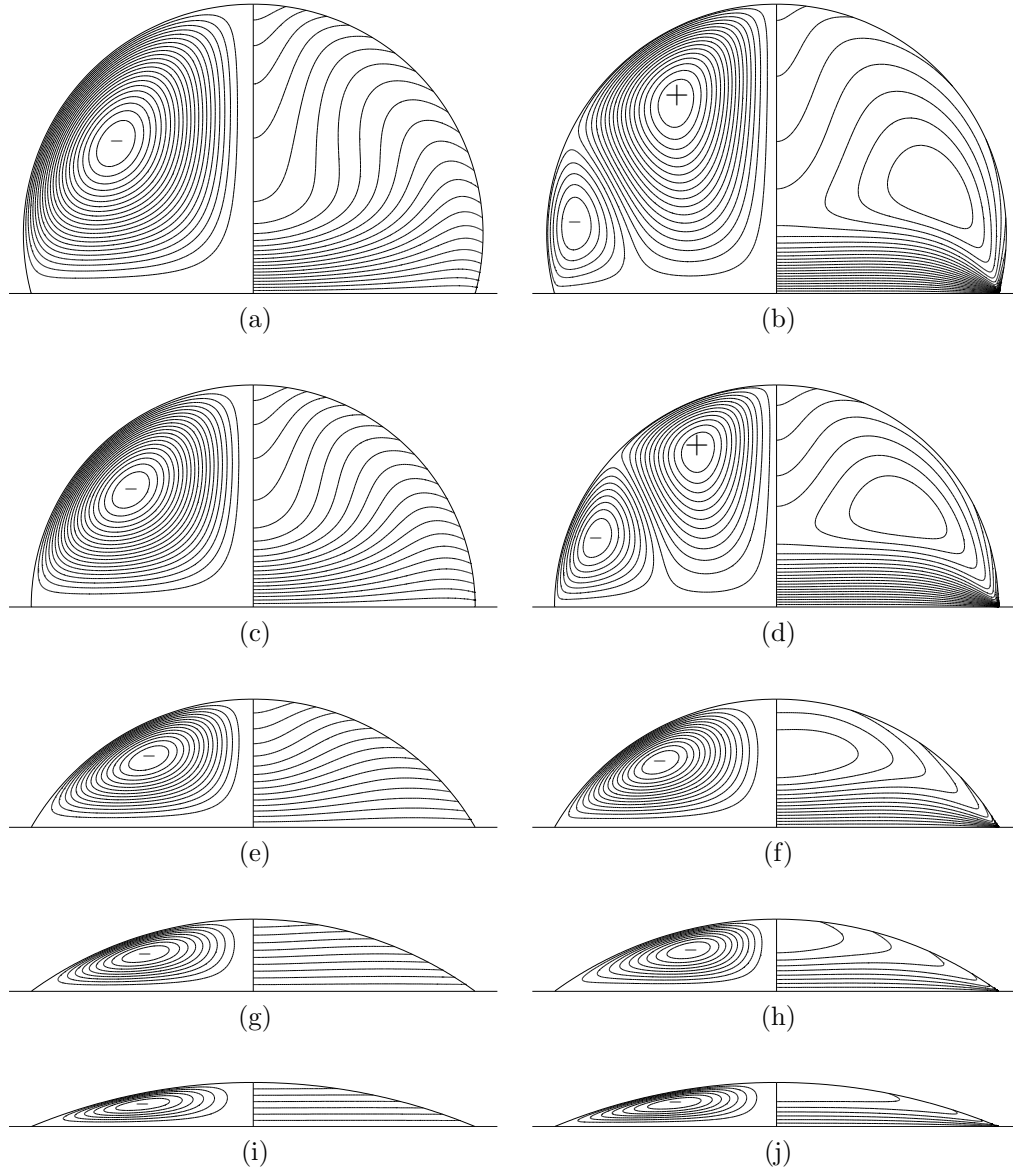


Figure 5.8: Streamlines and isotherms for thermocapillary-driven flow (left column) and the eigenvector isolines corresponding to the most dangerous mode of stream function and temperature (right column). The parameters are $Ma = 400$, $Pr = 4$, $Bi = 1$, $Gr = 0$, $\theta_w = 1$, and (a,b) $\alpha = 105^\circ$, (c,d) $\alpha = 90^\circ$, (e,f) $\alpha = 60^\circ$, (g,h) $\alpha = 36^\circ$, (i,j) $\alpha = 22.5^\circ$.

The evolution of perturbations in droplets with different contact angles are illustrated in figure 5.8 for a constant Marangoni number, $Ma = 400$. Similar to figure 5.7, the basic state results and the eigenvector isolines are plotted in the left and right columns, respectively. Patterns of the stream function perturbations for droplets with large contact angles exhibit two counter-rotating toroidal vortices and the perturbation isotherms have a toroidal structure, as it is discussed before. However, for shallower droplets, the perturbation isotherms become flatter and the thermal gradient along the free surface leads to surface tension stresses which drive the flow just in one direction (upward starting from the contact line). Therefore, the clockwise vortex, whose structure is very similar to the streamlines (left column), fully dominates the flow as shown in figures 5.8f, 5.8h, and 5.8j.

5.3 Combined thermocapillary-buoyant flow

In the previous section, it was proven that the pure thermocapillary-driven flow in liquid droplets is always linearly axisymmetrically stable (wave number $m = 0$). In this section, the axisymmetric stability of the mixed thermocapillary-buoyant flow in sessile droplets sitting on a heated plate as well as in hanging droplets attached to a cooled plate is discussed.

Figure 5.9 illustrates the development of stream function and temperature perturbations in droplets when the level of gravity increases. From left to right each row presents a constant Marangoni number ($Ma = 40, 400, \text{ and } 8000$, respectively) and the Grashof number is constant in each row which increases from top to bottom. As discussed in the previous chapter, the buoyancy dominates the flow only when the thermocapillary Reynolds number is relatively small. Comparing the evolution of perturbations when the Grashof number increases in the left and right columns (low and high Reynolds numbers, respectively) confirms this statement.

In the left column, by increasing the gravity level from $Gr = 10$ to $Gr = 100$, a counter-rotating toroidal vortex ('+') develops close to the centerline of the droplet as shown in figure 5.9d. However, the vortex is still weak in comparison to the thermocapillary-driven vortex ('-'), since the perturbation isotherms are quite similar in figures 5.9a and 5.9d. By increasing the gravity level further, the buoyancy-driven vortex fully dominates the flow and becomes stronger in magnitude. The pattern of thermal perturbations then gradually changes for higher Grashof numbers (see figures 5.9j and 5.9m).

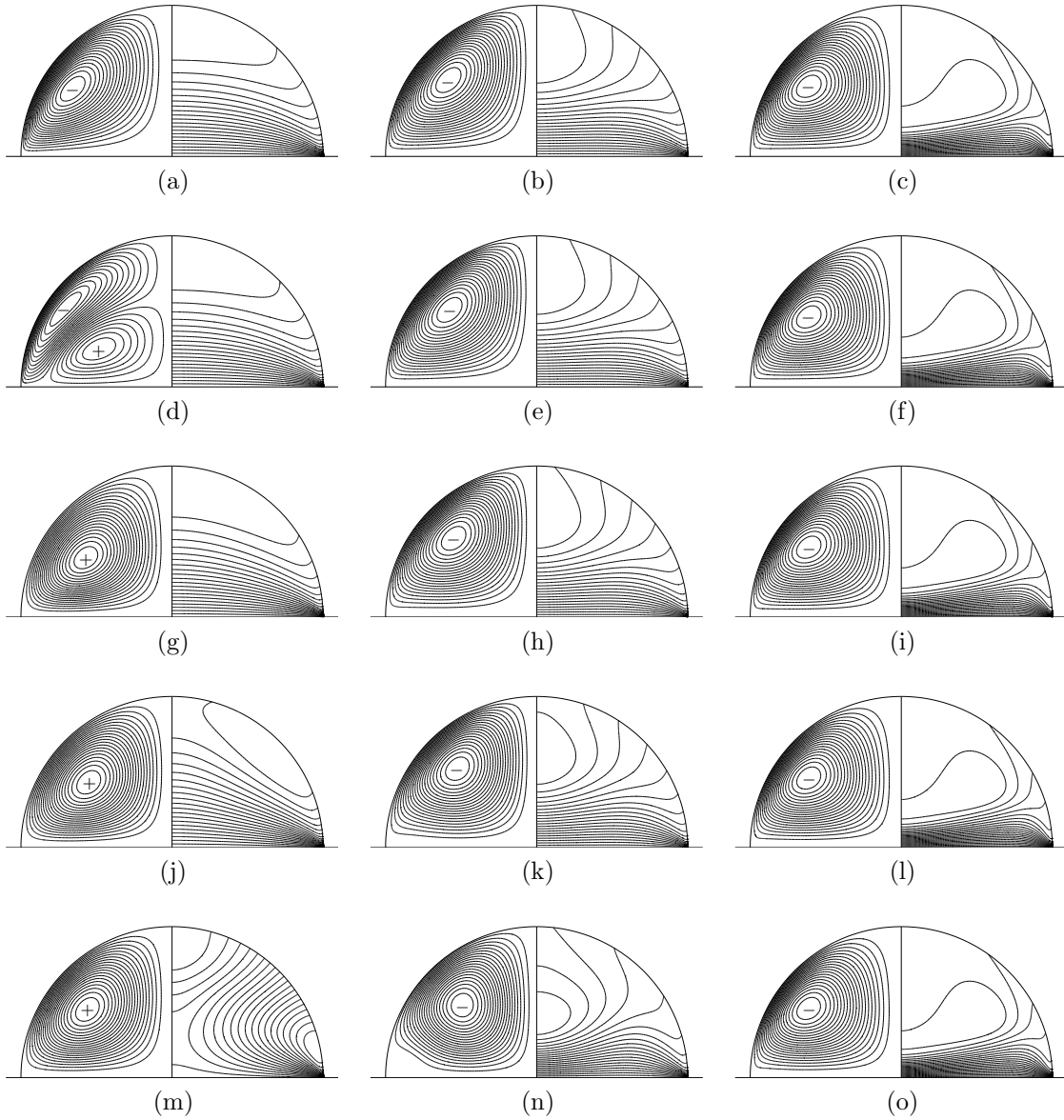


Figure 5.9: Isolines corresponding to the neutral modes of stream function and temperature for the combined thermocapillary-buoyant flow in a sessile droplet sitting on a heated plate; $Ma = 40$ (left column), $Ma = 400$ (middle column), and $Ma = 8000$ (left column). The parameters are $Pr = 4$, $Bi = 0.1$, $\alpha = 90^\circ$, and (a,b,c) $Gr = 10$, (d,e,f) $Gr = 100$, (g,h,i) $Gr = 500$, (j,k,l) $Gr = 1000$, (m,n,o) $Gr = 3000$.

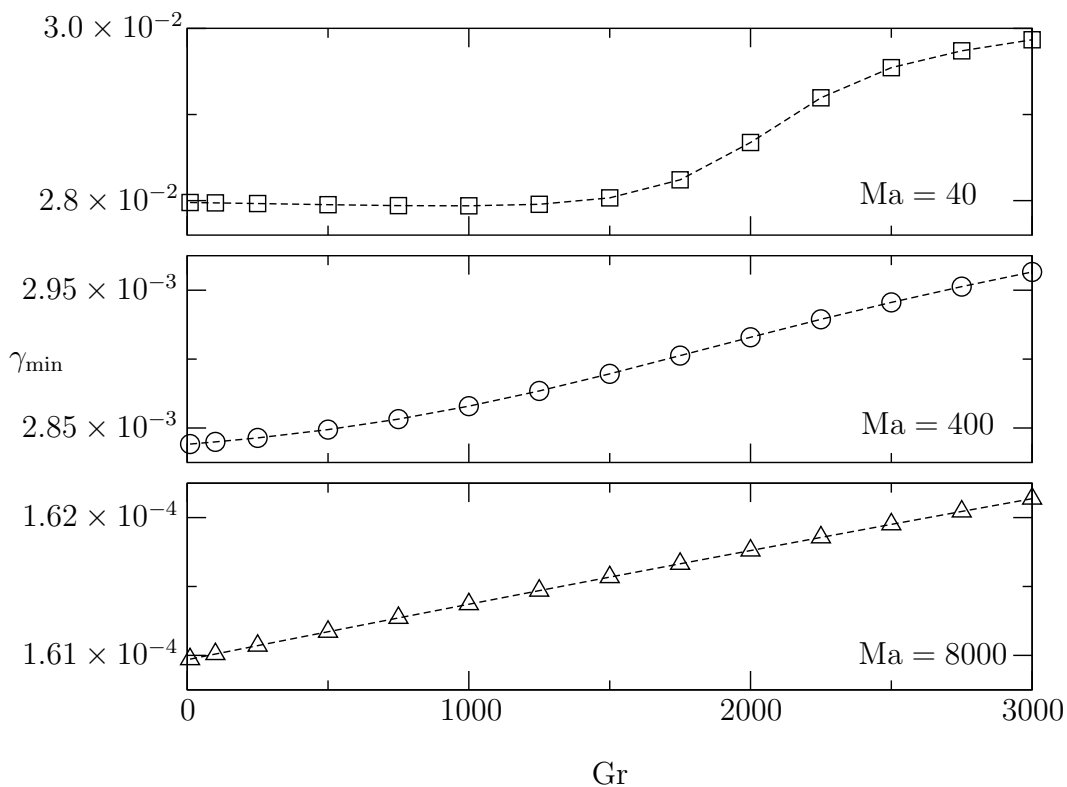


Figure 5.10: The most dangerous eigenvalue, γ_{\min} , as a function of the Grashof number, with the Marangoni number as a parameter, for the combined thermocapillary-buoyant flow in a sessile droplet sitting on a heated plate. The parameters are the same as in figure 5.9. The dashed lines are guides to the eye.

In contrast to the low Marangoni number case, the structure of perturbation isolines does not change by increasing the level of gravity for a high Marangoni number, $Ma = 8000$ (right column of figure 5.9). In other words, for a large enough Marangoni number, the flow is fully dominated by the thermocapillarity no matter how large the gravity level is. Similar conclusion has been given by Carpenter and Homay (1990) for the flow in a square cavity. For a moderate value of the Marangoni number ($Ma = 400$) which is shown in the middle column, a weak deflection of the stream function perturbations can be observed in figure 5.9n for a very large Grashof number, $Gr = 3000$. However, even for lower Grashof numbers, a slight difference in the perturbation isotherms can be observed comparing figures 5.9b and 5.9k which expresses a weak influence of the buoyancy.

Although the influence of the gravity level on the neutral mode is presented in figure 5.9, the stabilizing or destabilizing effect of buoyancy cannot be concluded from the plotted isolines. In order to study the effect of buoyancy on the stability of the liquid droplet

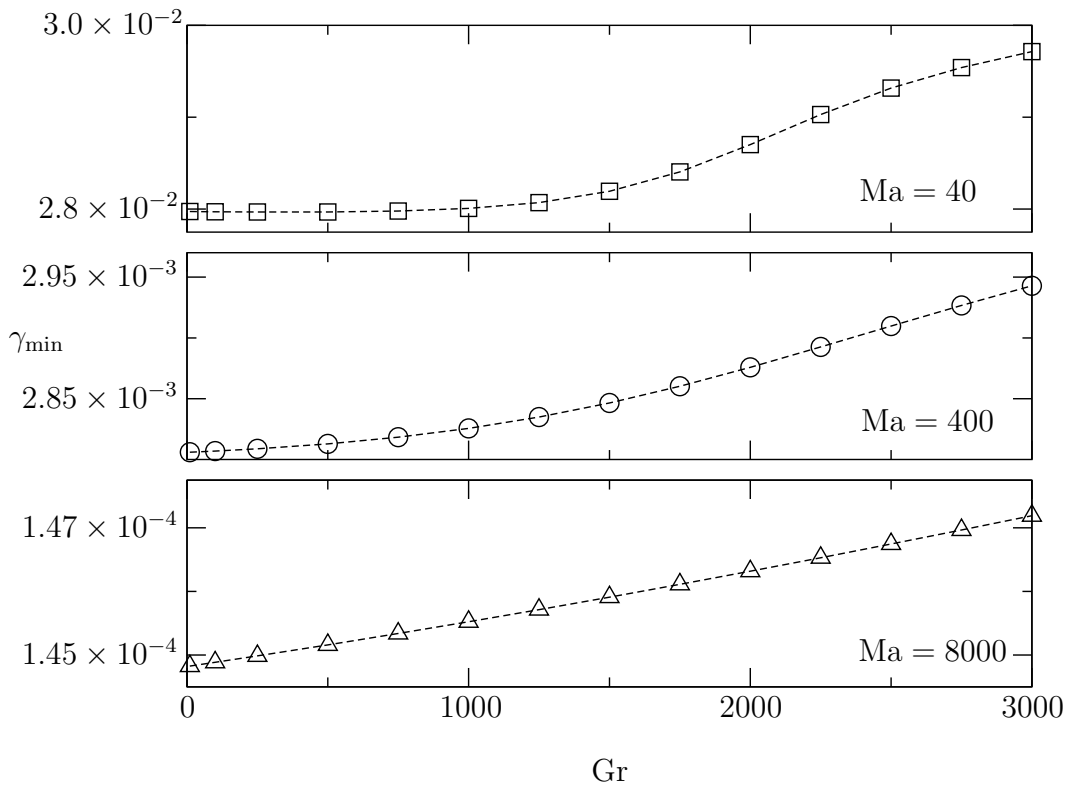


Figure 5.11: The most dangerous eigenvalue, γ_{\min} , as a function of the Grashof number, with the Marangoni number as a parameter, for the combined thermocapillary-buoyant flow in a hanging droplet attached to a cooled plate. The parameters are the same as in figure 5.12. The dashed lines are guides to the eye.

in a combined thermocapillary-buoyant flow, the most dangerous eigenvalues are obtained by solving the generalized eigenvalue problem for a wide range of Marangoni and Grashof numbers. The results are classified and plotted in figure 5.10. The positive slope of all the curves (except for a very weak local minimum which appears at $Gr = 1000$ in the upper curve) shows that the smallest eigenvalue grows by increasing the Grashof number, despite different trends for different Marangoni numbers. It means that the flow becomes more stable when the level of gravity increases. As a result, it can be concluded that the buoyancy has a stabilizing effect on the combined thermocapillary-buoyant flow independent of the Marangoni number. Moreover, the results confirm that the combined thermocapillary-buoyant flow is axisymmetrically stable similar to the case of pure thermocapillary-driven flow.

Similar investigation is done for the case of a hanging droplet attached to a cooled plate and the results are shown in figures 5.11 and 5.12. The obtained trends for the curves of the most dangerous eigenvalues versus Grashof number (figure 5.11) are nearly identical

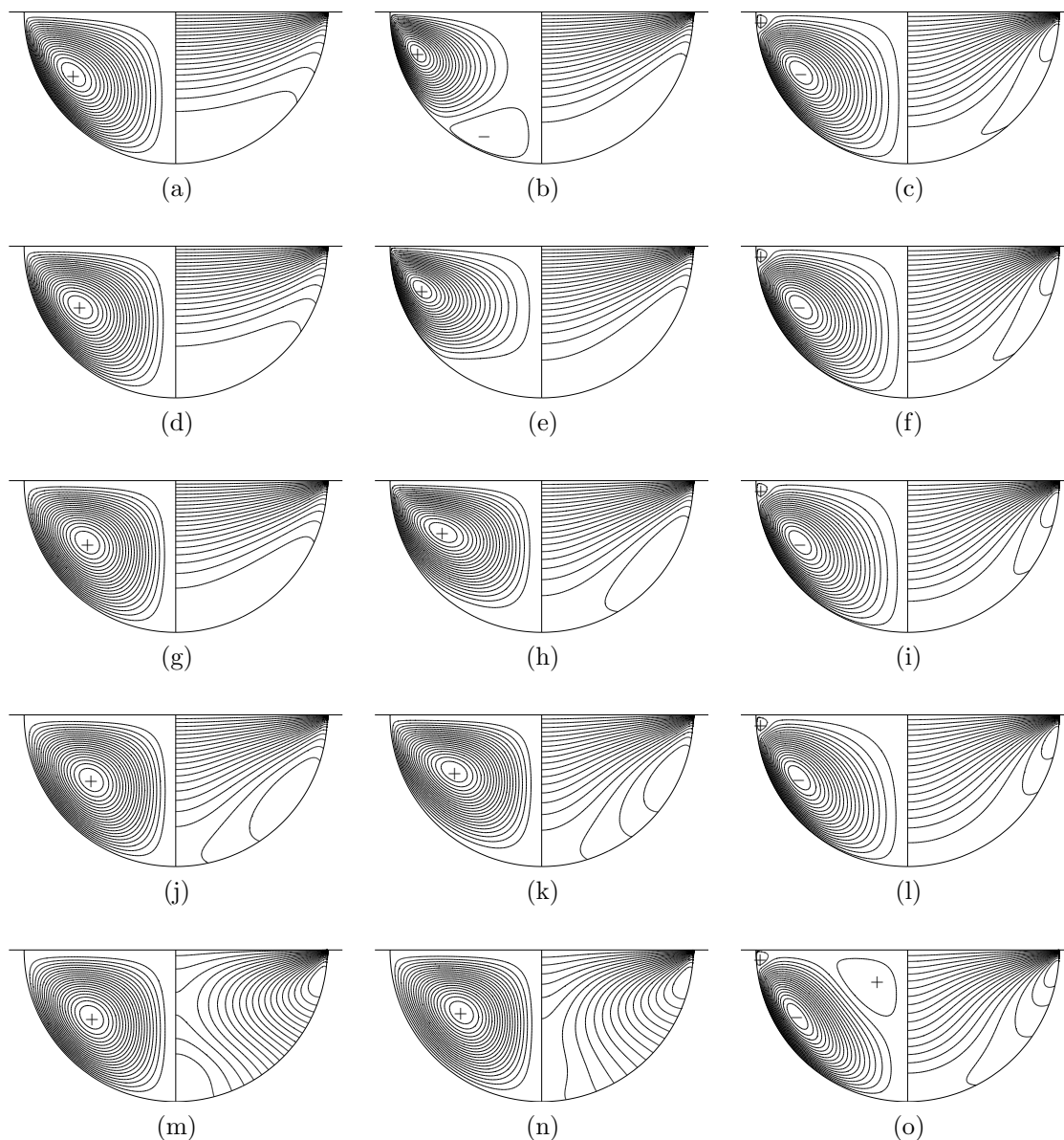


Figure 5.12: Isolines corresponding to the neutral modes of stream function and temperature for the combined thermocapillary-buoyant flow in a hanging droplet attached to a cooled plate; $Ma = 40$ (left column), $Ma = 400$ (middle column), and $Ma = 8000$ (right column). The parameters are $Pr = 4$, $Bi = 0.1$, $\alpha = 90^\circ$, and (a,b,c) $Gr = 10$, (d,e,f) $Gr = 100$, (g,h,i) $Gr = 500$, (j,k,l) $Gr = 1000$, (m,n,o) $Gr = 3000$.

5.3 Combined thermocapillary-buoyant flow

to the ones of the heated plate case as shown in figure 5.10 with some small deviations in the vertical axis. However, the evolution of the perturbations is different, comparing figures 5.9 and 5.12. In this case, patterns of perturbation isotherms exhibit a more uniform thermal gradients along the centerline which is different from the heated plate case. Therefore, the flow perturbations evolve differently by increasing the gravity level. Even for a very high Marangoni number (right column of figure 5.12), the effect of buoyancy on the stream function perturbations can be distinguished (see figure 5.12o) although the thermocapillarity remains dominant.

Chapter 6

Summary and Conclusions

The steady, incompressible, two-dimensional, axisymmetric flow in a non-volatile liquid droplet attached to a solid flat substrate has been numerically computed for three general cases of pure buoyancy-driven, pure thermocapillary-driven, and combined buoyant-thermocapillary flows. Assuming the droplet to have a non-deformable spherical-cap shape as a result of a large mean surface tension, the body-fitted toroidal coordinate is employed. The flow in both sessile and pendant droplets attached to an isothermal flat plate is investigated. The temperature in the ambient is assumed to vary linearly with the vertical distance from the substrate. Consequently, the heat transfer through the liquid-gas interface results in a temperature gradient within the droplet. This nonuniform temperature distribution initiates two different driving mechanisms: thermocapillarity which drives the flow along the liquid-gas interface and buoyancy which is a body force and acts in the bulk of the liquid. The governing equations in vorticity-stream function formulation are discretized by a second-order central difference scheme on a nonuniform computational grid and solved by means of an iterative solver implemented in Matlab. Results are presented in terms of streamlines and isotherms for different contact angles covering a wide range of thermocapillary Reynolds, Biot, Prandtl, and Grashof numbers. The data provided are claimed to have benchmark quality on account of the high accuracy which is attained employing a body-fitted coordinate system.

Based on the results obtained for the pure thermocapillary case, the flow can be categorized into two regimes, low and high Prandtl numbers. For each regime the flow behavior is different. For low Prandtl numbers, the stream function extremum, which represents the strength of the flow, was found to scale like $Ma^{-1/2}$ in the asymptotic limit of large Marangoni numbers. This scaling is valid for both sessile and pendant droplets. In contrast, different scalings are detected for the high Prandtl number

regime. For heated- and cooled-plate cases, the intensity of the flow scales like $\text{Ma}^{-1/3}$ and $\text{Ma}^{-2/3}$, respectively. Different thermal boundary layers, observed for a heated and a cooled plate, are found to be the reason for the different scalings. Furthermore, a scaling analysis of the boundary conditions on the free surface has been provided in the limit of shallow droplets ($\alpha \rightarrow 0$). The analysis yields the scalings $|\Psi|_{\max} \sim \alpha^3$ and $1 - \theta_{\text{apex}} \sim \alpha$. Both scalings are confirmed with the numerical results obtained for droplets with a range of small contact angles.

The onset of thermal convection in the pure buoyant flow is obtained when the temperature distribution is uniform in vertical direction. To retrieve this temperature distribution, a limit of maximum heat transfer rate through the liquid-gas interface ($\text{Bi} \rightarrow \infty$) is considered. A nearly perfect bifurcation diagram is obtained by plotting the stream function extremum as a function of Rayleigh number. The onset of thermal convection is examined for different droplet shapes. The values obtained for shallow droplets are in good agreement with the onset of thermal convection in thin liquid layers heated from below. Different origins have found for the observed toroidal convection cells: the cells close to the center of the droplet are driven by buoyant forces, whereas the ones in the vicinity of the contact line are formed by viscous forces. These two convection cell types can be visually distinguished. The streamlines of the buoyancy-driven cells have a symmetrical shape, while the center of the viscous eddies are displaced towards the separating streamlines. An empirical relation between the aspect ratio of the droplet and the number of convection cells is proposed, $N_{\text{cell}} \approx 1/l$.

In the presence of buoyancy and thermocapillarity, the flow is driven predominantly by thermocapillary stresses, except in the limit of low thermocapillary Reynolds number. Under such conditions, buoyant forces either compete with the thermocapillary forces and generate a counter-rotating vortex, or enhance the existing thermocapillary-driven vortex, depending on the temperature distribution within the domain. In case of competing forces, the separation of the buoyancy-driven vortex from the substrate strongly depends on the balance between body and surface forces. A more interesting competition of these forces is observed in shallow droplets. The surface tension stresses drive a global flow which envelops the cells driven by buoyancy. As a result, a series of co-rotating cells appears. The number of cells in these structures are found to be always less than the number of cells in the same droplet shape subject to pure buoyant forces.

By means of axisymmetric linear stability analysis, the neutral Rayleigh number is obtained for the pure buoyant flow in droplets of different contact angles subject to a uniform temperature distribution in vertical direction. The onset of thermal convection

obtained from the nonlinear calculations has been confirmed by the results of the linear stability analysis. For liquid droplets of different contact angles, the independence of the neutral Rayleigh number from the Prandtl number is confirmed numerically as well as analytically. For the thermocapillary-driven flow, it is found that no linear instability exists with the wave number $m = 0$ independent of the Marangoni number and the contact angle. It is shown that the most dangerous eigenvalue scales with Marangoni number like Ma^{-1} for $\text{Pr} > 1$, and $\text{Ma}^{-0.8}$ for a very low Prandtl number ($\text{Pr} = 0.02$). In case of the combined thermocapillary-buoyant flow, buoyancy is found to have a stabilizing effect on the flow in sessile and hanging droplets.

To extend the scope of the current study, many directions can be suggested. Firstly, considering the latent heat due to evaporation in the boundary conditions of the liquid-gas interface is probably the most appropriate extension to this work. A reason for neglecting the evaporation in this study was to decouple the problem and focus particularly on other influential phenomena such as thermocapillarity and buoyancy. Therefore, including the evaporation would help to provide more realistic results. Secondly, an analytical scaling analysis is suggested in order to clarify various scalings which have been found between stream function and Marangoni number. Finally, a full three-dimensional linear stability analysis would be of interest to analyze the instability mechanisms in buoyancy-driven as well as thermocapillary-driven flows.

Bibliography

- A. Al-Sharafi, H. Ali, B. S. Yilbas, A. Z. Sahin, M. Khaled, N. Al-Aqeeli, and F. Al-Sulaiman. Influence of thermalcapillary and buoyant forces on flow characteristics in a droplet on hydrophobic surface. *Int. J. of Therm. Sci.*, 102:239–253, 2016.
- K. Arafune, K. Kodera, A. Kinoshita, and A. Hirata. Control of crystal–melt interface shape during horizontal Bridgman growth of InSb crystal using solutal Marangoni convection. *J. Crystal Growth*, 249:429–436, 2003.
- G. Arfken. *Mathematical Methods for Physicists*. Academic Press, Amsterdam, 3rd edition, 1985.
- W. E. Arnoldi. The principle of minimized iterations in the solution of the matrix eigenvalue problem. *Quart. Appl. Math.*, 9:17–29, 1951.
- L. Y. Barash, T. P. Bigioni, V. M. Vinokur, and L. N. Shchur. Evaporation and fluid dynamics of a sessile drop of capillary size. *Phys. Rev. E*, 79:046301, 2009.
- W. Barten, M. Lücke, W. Hort, and M. Kamps. Fully developed traveling-wave convection in binary fluid mixtures. *Phys. Rev. Lett.*, 63:376–379, 1989.
- G. K. Batchelor. *An Introduction to Fluid Dynamics*. Cambridge University Press, 1967.
- H. Ben Hadid and B. Roux. Buoyancy- and thermocapillary-driven flows in differentially heated cavities for low-Prandtl-number fluids. *J. Fluid Mech.*, 235:1–36, 1992.
- H. Bénard. Les tourbillons cellulaires dans une nappe liquide. *Revue Gén. Sci. Pur. Appl.*, 11:1261–1271, 1900.
- R. D. Benguria and M. C. Depassier. Oscillatory instabilities in the Rayleigh–Bénard problem with a free surface. *Phys. Fluids*, 30:1678–1682, 1987.
- P. Bergé, M. Dubois, P. Manneville, and Y. Pomeau. Intermittency in Rayleigh–Bénard convection. *J. Physique Lett.*, 41:341–345, 1980.

BIBLIOGRAPHY

- T. L. Bergman and S. Ramadhyani. Combined buoyancy- and thermocapillary driven convection in open square cavities. *Numer. Heat Transfer*, 9:441–451, 1986.
- J. Birks and R. S. Bradley. The rate of evaporation of droplets. II. the influence of changes of temperature and of the surrounding gas on the rate of evaporation of drops of di-n-butyl phthalate. *Proc. R. Soc. A*, 198(1053):226–239, 1949.
- J. A. Black. *Compound Droplets for Lab-on-a-Chip*. PhD thesis, Georgia Institute of Technology, 2016.
- M. J. Block. Surface tension as the cause of Bénard cells and surface deformation in a liquid film. *Nature*, 178:650–651, 1956.
- W. N. Bond and D. A. Newton. Bubbles, drops, and Stokes’ law. (paper 2). *Philos. Mag.*, 5(30):794–800, 1928.
- R. S. Bradley and A. D. Shellard. The rate of evaporation of droplets. iii. vapour pressures and rates of evaporation of straight-chain paraffin hydrocarbons. *Proc. R. Soc. A*, 198(1053):239–251, 1949.
- G. J. Buck. Force-free magnetic-field solution in toroidal coordinates. *J. Appl. Phys.*, 36(7):2231–2235, 1965.
- F. H. Busse. Non-linear properties of thermal convection. *Rep. Prog. Phys.*, 41:1929–1967, 1978.
- F. H. Busse. Asymptotic theory of convection in a rotating, cylindrical annulus. *J. Fluid Mech.*, 173:545–556, 1986.
- F. Carle, B. Sobac, and D. Brutin. Hydrothermal waves on ethanol droplets evaporating under terrestrial and reduced gravity levels. *J. Fluid Mech.*, pages 1–10, 2012.
- B. M. Carpenter and G. M. Homsy. High Marangoni number convection in a square cavity: Part II. *Phys. Fluids A*, 2:137–149, 1990.
- S. Chandrasekhar. *Hydrodynamic and Hydromagnetic Stability*. Oxford University Press, Oxford, 1961.
- J. Chen and K. J. Stebe. Surfactant-induced retardation of the thermocapillary migration of a droplet. *J. Fluid Mech.*, 340:35–59, 1997.
- J. Z. Chen, S. M. Troian, A. A. Darhuber, and S. Wagner. Effect of contact angle hysteresis on thermocapillary droplet actuation. *J. Appl. Phys.*, 97(1):014906, 2005.

- E. Citakoglu and J. W. Rose. Dropwise condensation—the effect of surface inclination. *Int. J. Heat Mass Transfer*, 12(5):645–650, 1969.
- R. M. Clever and F. H. Busse. Transition to time-dependent convection. *J. Fluid Mech.*, 65:625–645, 1974.
- P. Colinet and J. C. Legros. On the Hopf bifurcation occurring in the two-layer Rayleigh–Bénard convective instability. *Phys. Fluids*, 6:2631–2639, 1994.
- J. H. Curry, J. R. Herring, J. Loncaric, and S. A. Orszag. Order and disorder in two- and three-dimensional Bénard convection. *J. Fluid Mech.*, 147:1–38, 1984.
- A. A. Darhuber and S. M. Troian. Principles of microfluidic actuation by modulation of surface stresses. *Annu. Rev. Fluid Mech.*, 37:425–455, 2005.
- S. H. Davis. Thermocapillary instabilities. *Annu. Rev. Fluid Mech.*, 19:403–435, 1987.
- S. H. Davis and G. M. Homsy. Energy stability theory for free-surface problems: buoyancy–thermocapillary layers. *J. Fluid Mech.*, 98:527–553, 1980.
- R. D. Deegan, O. Bakajin, T. F. Dupont, G. Huber, S. R. Nagel, and T. A. Witten. Capillary flow as the cause of ring stains from dried liquid drops. *Nature*, 389:827–829, 1997.
- P. G. Drazin and W. H. Reid. *Hydrodynamic Stability*. Cambridge University Press, Cambridge, 1981.
- G. J. Dunn, S. K. Wilson, B. R. Duffy, S. David, and K. Sefiane. A mathematical model for the evaporation of a thin sessile liquid droplet: Comparison between experiment and theory. *Colloids Surf., A*, 323(1-3):50–55, 2008.
- G. J. Dunn, S. K. Wilson, B. R. Duffy, S. David, and K. Sefiane. The strong influence of substrate conductivity on droplet evaporation. *J. Fluid Mech.*, 623:329–351, 2009.
- W. E and J. Liu. Vorticity boundary condition and related issues for finite difference schemes. *J. Comput. Phys.*, 124(2):368–382, 1996.
- E. R. G. Eckert and W. O. Carlson. Natural convection in an air layer enclosed between two vertical plates with different temperatures. *Int. J. Heat Mass Transfer*, 2(1):106–120, 1961.
- C. A. J. Fletcher. *Computational Techniques for Fluid Dynamics*, volume I of *Springer Series in Computational Physics*. Springer, 1991.

BIBLIOGRAPHY

- N. A. Fuchs. *Evaporation and droplet growth in gaseous media*. Pergamon, 1959.
- T. Fuhrich, P. Berger, and H. Hügel. Marangoni effect in laser deep penetration welding of steel. *J. Laser Appl.*, 13(5):178–186, 2001.
- R. Fürstner, W. Barthlott, C. Neinhuis, and P. Walzel. Wetting and self-cleaning properties of artificial superhydrophobic surfaces. *Langmuir*, 21(3):956–961, 2005.
- R. J. Good and M. N. Koo. The effect of drop size on contact angle. *J. Colloid Interface Sci.*, 71(2):283–292, 1979.
- Z. Guo, F. Zhou, and J. Hao and W. Liu. Stable biomimetic super-hydrophobic engineering materials. *J. Amer. Chem. Soc.*, 127(45):15670–15671, 2005.
- Z. Y. Guo, D. Y. Li, and B. X. Wang. A novel concept for convective heat transfer enhancement. *Int. J. Heat Mass Transfer*, 41(14):2221–2225, 1998.
- H. Haj-Hariri, Q. Shi, and A. Borhan. Thermocapillary motion of deformable drops at finite reynolds and Marangoni numbers. *Phys. Fluids*, 9(4):845–855, 1997.
- J. J. Hegseth, N. Rashidnia, and A. Chai. Natural convection in droplet evaporation. *Phys. Rev. E*, 54:1640–1644, 1996.
- H. Hu and R. G. Larson. Marangoni effect reverses coffee-ring depositions. *J. Phys. Chem. B*, 110(14):7090–7094, 2006.
- G. J. Hwang and K. C. Cheng. Convective instability in the thermal entrance region of a horizontal parallel-plate channel heated from below. *J. Heat Transfer*, 95(1):72–77, 1973.
- H. Jamgotchian, N. Bergeon, D. Benielli, Ph. Voge, B. Billia, and R. Guérin. Localized microstructures induced by fluid flow in directional solidification. *Phys. Rev. Lett.*, 87:166105, 2001.
- G. Karapetsas, O. K. Matar, P. Valluri, and K. Sefiane. Convective rolls and hydrothermal waves in evaporating sessile drops. *Langmuir*, 28(31):11433–11439, 2012.
- C. T. Kelley. *Iterative Methods for Linear and Nonlinear Equations*. Frontiers in Applied Mathematics. SIAM, Philadelphia, 1995.
- H. Kim, F. Boulogne, E. Um, I. Jacobi, E. Button, and H. A. Stone. Controlled uniform coating from the interplay of Marangoni flows and surface-adsorbed macromolecules. *Phys. Rev. Lett.*, 116:124501, 2016.

- J. R. Kliegel and J. N. Levine. Transonic flow in small throat radius of curvature nozzles. *AIAA J.*, 7(7):1375–1378, 1969.
- M. N. Kooper, H. A. van der Vorst, S. Poedts, and J. P. Goedbloed. Application of the implicitly updated arnoldi method with a complex shift-and-invert strategy in mhd. *J. Comput. Phys.*, 118(2):320–328, 1995.
- S. A. Korpela, D. Gözöm, and C. B. Baxi. On the stability of the conduction regime of natural convection in a vertical slot. *Int. J. Heat Mass Transfer*, 16(9):1683–1690, 1973.
- L. I. G. Kovasznay. Laminar flow behind a two-dimensional grid. *Math. Proc. Cambridge Philos. Soc.*, 44:58–62, 1948.
- H. C. Kuhlmann. *Thermocapillary Convection in Models of Crystal Growth*, volume 152 of *Springer Tracts in Modern Physics*. Springer, Berlin, Heidelberg, 1999.
- H. C. Kuhlmann, C. Nienhüser, and H. J. Rath. The local flow in a wedge between a rigid wall and a surface of constant shear stress. *J. Eng. Math.*, 36:207–218, 1999.
- H. C. Kuhlmann, R. V. Mukin, T. Sano, and I. Ueno. Structure and dynamics of particle-accumulation in thermocapillary liquid bridges. *Fluid Dyn. Res.*, 46(4):041421–1–041421–22, 2014.
- I. Langmuir. Vapor pressures, evaporation, condensation and adsorption. *J. Amer. Chem. Soc.*, 54(7):2798–2832, 1932.
- D. Lanzerstorfer and H. C. Kuhlmann. Global stability of the two-dimensional flow over a backward-facing step. *J. Fluid Mech.*, 693:1–27, 2012.
- M. Lappa. On the existence and multiplicity of one-dimensional solid particle attractors in time-dependent Rayleigh-Bénard convection. *Chaos*, 23(1):013105–013105–9, 2013.
- R. B. Lehoucq and D. C. Sorensen. Deflation techniques for an implicitly restarted arnoldi iteration. *SIAM J. Matrix Anal. Appl.*, 17(4):789–821, 1996.
- N. Liron and J. R. Blake. Existence of viscous eddies near boundaries. *J. Fluid Mech.*, 107:109–129, 1981.
- Lord Rayleigh. On convection currents in a horizontal layer of fluid, when the higher temperature is on the under side. *Phil. Mag.*, 32:529–546, 1916.

BIBLIOGRAPHY

- T. Lundgren and P. Koumoutsakos. On the generation of vorticity at a free surface. *J. Fluid Mech.*, 382:351–366, 1999.
- A. J. Mahajan, E. H. Dowell, and D. B. Bliss. Eigenvalue calculation procedure for an Euler/Navier-Stokes solver with application to flows over airfoils. *J. Comput. Phys.*, 97:398–413, 1991.
- V. S. Malyuga. Viscous eddies in a circular cone. *J. Fluid Mech.*, 522:101–116, 2005.
- C. Marangoni. Ueber die Ausbreitung der Tropfen einer Flüssigkeit auf der Oberfläche einer anderen. *Ann. Phys. Chem.*, 143:337–354, 1871.
- A. Marin, R. Liepelt, M. Rossi, and C. J. Kahler. Surfactant-driven flow transitions in evaporating droplets. *Soft Matter*, 12:1593–1600, 2016.
- G. McHale, S. Aqil, N. J. Shirtcliffe, M. I. Newton, and H. Y. Erbil. Analysis of droplet evaporation on a superhydrophobic surface. *Langmuir*, 21(24):11053–11060, 2005.
- H. K. Moffatt. Viscous and resistive eddies near a sharp corner. *J. Fluid Mech.*, 18:1–18, 1964.
- R. Mollaret, K. Sefiane, J. R. E. Christy, and D. Veyret. Experimental and numerical investigation of the evaporation into air of a drop on a heated surface. *Chem. Eng. Res. Des.*, 82(4):471–480, 2004.
- S. W. Morris, E. Bodenschatz, D. S. Cannell, and G. Ahlers. Spiral defect chaos in large aspect ratio Rayleigh-Bénard convection. *Phys. Rev. Lett.*, 71:2026–2029, 1993.
- T. Mullin. *The nature of chaos*. Oxford University Press, USA, 1993.
- H. Nguyen and J. Chen. Numerical study of a droplet migration induced by combined thermocapillary-buoyancy convection. *Phys. Fluids*, 22(12):062102, 2010.
- V. X. Nguyen and K. J. Stebe. Patterning of small particles by a surfactant-enhanced Marangoni-Bénard instability. *Phys. Rev. Lett.*, 88:164501, 2002.
- C. Nienhüser and H. C. Kuhlmann. Stability of thermocapillary flows in non-cylindrical liquid bridges. *J. Fluid Mech.*, 458:35–73, 2002.
- A. Odukoya and G. F. Naterer. Transient response of thermocapillary pumping of a droplet in a micro heat engine. *Int. J. Heat Mass Transfer*, 58(12):6–17, 2013.
- T. Onda, S. Shibuichi, N. Satoh, , and K. Tsujii. Super-water-repellent fractal surfaces. *Langmuir*, 12(9):2125–2127, 1996.

- S. Ostrach. Motion induced by capillarity (V. G. Levich Festschrift). In D. B. Spalding, editor, *Physico-chemical Hydrodynamics*, volume 2. Advance Publications, 1977.
- J. Park and J. Moon. Control of colloidal particle deposit patterns within picoliter droplets ejected by ink-jet printing. *Langmuir*, 22(8):3506–3513, 2006.
- D. Pesach and A. Marmur. Marangoni effects in the spreading of liquid mixtures on a solid. *Langmuir*, 3(4):519–524, 1987.
- R. G. Picknett and R. Bexon. The evaporation of sessile or pendant drops in still air. *J. Colloid Interface Sci.*, 61(2):336–350, 1977.
- J. Priede and G. Gerbeth. Convective, absolute, and global instabilities of thermocapillary-buoyancy convection in extended layers. *Phys. Rev. E*, 56:4187–4199, 1997.
- G. W. Recktenwald. *Numerical methods with MATLAB: implementations and applications*. Prentice Hall Upper Saddle River, 2000.
- S. W. Rienstra. The shape of a sessile drop for small and large surface tension. *J. Eng. Math.*, 24(3):193–202, 1990.
- W. D. Ristenpart, P. G. Kim, C. Domingues, J. Wan, and H. A. Stone. Influence of substrate conductivity on circulation reversal in evaporating drops. *Phys. Rev. Lett.*, 99:234502, 2007.
- P. J. Sáenz, K. Sefiane, J. Kim, O. K. Matar, and P. Valluri. Evaporation of sessile drops: a three-dimensional approach. *J. Fluid Mech.*, 772:705–739, 2015.
- T. S. Sammarco and M. A. Burns. Heat-transfer analysis of microfabricated thermocapillary pumping and reaction devices. *J. Micromech. Microeng.*, 10(1):42–55, 2000.
- R. Savino, D. Paterna, and N. Favaloro. Buoyancy and Marangoni effects in an evaporating drop. *Philos. Mag.*, 16(4):562–574, 2002.
- M. Schmitt and H. Stark. Marangoni flow at droplet interfaces: Three-dimensional solution and applications. *Phys. Fluids*, 28(1):012106, 2016.
- D. Schwabe, U. Möller, J. Schneider, and A. Scharmann. Instabilities of shallow dynamic thermocapillary liquid layers. *Phys. Fluids A*, 4:2368–2381, 1992.

BIBLIOGRAPHY

- D. Schwabe, P. Hintz, and S. Frank. New features of thermocapillary convection in floating zones revealed by tracer particle accumulation structures (PAS). *Microgravity Sci. Technol.*, 9:163–168, 1996.
- L. E. Scriven and C. V. Sternling. The Marangoni effects. *Nature*, 187:186–188, 1960.
- K. Sefiane, J. R. Moffat, O. K. Matar, and R. V. Craster. Self-excited hydrothermal waves in evaporating sessile drops. *Appl. Phys. Lett.*, 93(7):074103, 2008.
- A. T. Shih and C. M. Megaridis. Thermocapillary flow effects on convective droplet evaporation. *Int. J. Heat Mass Transfer*, 39(2):247–257, 1996.
- L. Shmuylovich, A. Q. Shen, and H. A. Stone. Surface morphology of drying latex films: Multiple ring formation. *Langmuir*, 18(9):3441–3445, 2002.
- R. S. Subramanian and R. Balasubramaniam. *The Motion of Bubbles and Drops in Reduced Gravity*. Cambridge University Press, 2005.
- L. M. M. Thomson. *Theoretical Hydrodynamics, Fourth Edition*. London; St. Martin's Press: New York, 1960.
- I. Ueno. Flow patterns and particle behaviors induced by thermocapillary effect in hanging droplets. (private communication), 2011.
- I. Ueno, Y. Abe, K. Noguchi, and H. Kawamura. Dynamic particle accumulation structure (PAS) in half-zone liquid bridge – reconstruction of particle motion by 3-D PTV. *Adv. Space Res.*, 41:2145–2149, 2008.
- J. S. Vrentas, R. Narayanan, and S. S. Agrawal. Free surface convection in a bounded cylindrical geometry. *Int. J. Heat Mass Transfer*, 24:1513–1529, 1981.
- Q. Wang, J. Qian, Y. Li, Y. Zhang, D. He, S. Jiang, Y. Wang, X. Wang, L. Pan, and J. Wang. 2d molecular semiconductors: 2d single-crystalline molecular semiconductors with precise layer definition achieved by floating-coffee-ring-driven assembly. *Adv. Funct. Mater.*, 26(19):3181–3181, 2016.
- T. G. Wright and L. N. Trefethen. Large-scale computation of pseudospectra using ARPACK and Eigs. *SIAM J. Sci. Comput.*, 23(2):591–605, 2001.
- Z. Wu and W. Hu. Thermocapillary migration of a planar droplet at moderate and large Marangoni numbers. *Acta Mech.*, 223(3):609–626, 2011.

BIBLIOGRAPHY

- M. Yekta-Fard and A. B. Ponter. The influences of vapor environment and temperature on the contact angle-drop size relationship. *J. Colloid Interface Sci.*, 126(1):134–140, 1988.
- R. K. Zeytounian. Joseph Boussinesq and his approximation: a contemporary view. *C.R. Acad. Sci. Mec.*, 331(8):575–586, 2003.
- N. Zhang and W. Yang. Natural convection in evaporating minute drops. *J. Heat Transfer*, 104(4):656–662, 1982.